Modeling Nanomaterials with Efficient and Accurate Electronic Structure Methods

Hongbin Liu

A dissertation
submitted in partial fulfillment of the
requirements for the degree of

Doctor of Philosophy

University of Washington

2019

Reading Committee:

Xiaosong Li, Chair

Daniel R. Gamelin

David S. Ginger

Program Authorized to Offer Degree:
Chemistry

University of Washington

Abstract

Modeling Nanomaterials with Efficient and Accurate Electronic Structure Methods

Hongbin Liu

Chair of the Supervisory Committee:
Professor Xiaosong Li
Department of Chemistry

Electronic structure methods are one of the most powerful tools in the computational toolbox to provide an atomistic understanding of molecules and materials. Among all electronic structure methods, Density functional theory (DFT) has become the standard choice for electronic structure calculations on molecules, clusters, surfaces, and solids, with thousands of papers published and new, improved, and more accurate functionals proposed almost every year. DFT methods have also gained great success in understanding the structural, thermodynamic, and electronic properties of nanomaterials like quantum dots and perovskite solar cells. However, with a growing demands for a deeper understanding of those nanomaterials, DFT has reached a bottleneck. Either the material system we are looking into is too complicated to be handled by DFT under current computational resources, or the physics we are targeting is beyond the capability of DFT. Therefore, more accurate and efficient methods need to be developed to better study nanomaterials. This dissertation covers both success stories of nanomaterials modeling by DFT, and efforts of developing new electronic structure methods for nanomaterials. After a brief introduction to the preliminary theory concepts in Chapter 1, Chapter 2 focuses on using DFT to rationalize experimental findings and predict the chemical and physical properties of the lead halide perovskites. Chapter 3 demonstrates the effort of pursuing the tractability of electronic structure methods to handle even larger chemical systems with no periodicity. Chapter 4 focuses on including relativis-

tic effects in electronic structure methods with the goal of accurate modeling of the wave functions of nanomaterials. Chapter 5 focuses on modeling external field and environmental effects. Though the benchmark and examples to the methods detailed in Chapter 4 and 5 are not real nanomaterial systems, the implementations are general and fully compatible to study the nanomaterial systems like metal or semiconductor clusters.

TABLE OF CONTENTS

LIST OF FIGURES

LIST OF TABLES

GLOSSARY

AO: Atomic Orbital

CAS: Complete Active Space no sympathy.

CASCI: Complete Active Space Configuration Interaction

CASSCF: Complete Active Space Self-Consistent Field

CASPT2: Complete Active Space Perturbation Theory of Second Order

CB: Conduction Band

CBM: Conduction Band Minimum

CI: Configuration Interaction

DFT: Density Functional Theory

DKH: Douglas-Kroll-Hess

DVR: Discrete Variable Representation

ERI: Electron Repulsion Integral

FCI: Full Configuration Interaction

FF: Fill Factor

GHF: Generalized Hartree-Fock

HF: Hartree-Fock

HOMO: Highest Occupied Molecular Orbital

KS: Kohn-Sham

MCSCF: Multi-Configurational Self-Consistent Field

MM: Molecular Mechanics

MO: Molecular Orbital

LUMO: Lowest Unoccupied Molecular Orbital

PBE: Perdew?Burke-Ernzerhof

PCE: Power Conversion Efficiency

PL: Photoluminescence

PV: Photovoltaic

PVSC: Perovskite Solar Cell

QD: Quantum Dot

QM: Quantum Mechanics

RT: Real-time

SA: State-Average

SOC: Spin-Orbit Coupling

SCF: Self-Consistent Field

TDCI: Time-dependent Configuration Interaction

TDDFT: Time-dependent Density Functional Theory

VB: Valence Band

VBM: Valence Band Maximum

XC: Exchange-Correlation

X2C: Exact Two Component

ACKNOWLEDGMENTS

Five years ago, I came to the University of Washington to pursue the Ph.D. degree. Since then, it has been a pleasant journey. There have been many people who have helped and supported me all the way through. Here I want to express my gratefulness to them.

First of all, words are hard to express my sincere gratitude to my advisor, Prof. Xiaosong Li. Thank you for offering me a chance to study with you five years ago, which changed my life entirely. You are a knowledgable, tolerant, patient, supportive, and charming advisor and have influenced me in so many ways. You guided me through the science and taught me to enjoy life. You have your door open and always welcome my confusions, questions, and emotions. Your self-discipline and enthusiasm for work, and philosophy of work-life-balance has set the best example for me to follow. It is my privilege to work with you. Thank you!

I would also like to thank my committee members, Prof. Daniel Gamelin, Prof. David Ginger, Prof. Stefan Stoll and Prof. Vincent Holmberg, for supervising my research and giving great comments and critics to drive me forward.

I spent most of my Ph.D. time in the theory suite, Bagley Hall. I would like to thank all Li group members, who used to reside or are currently residing in this room.You shine lights in my graduate student life. I am grateful to have Dr. Feizhi Ding, Dr. Bo Peng, Dr. Alessio Petrone, Dr. Patrick Lestrange, Dr. David Lingerfelt, Dr. Joshua Goings, and Dr. David Williams-Young who guided and mentored me in my earlier years as graduate student. I also want to express my appreciation to Dr. Andrew Jenkins, Joe Kasper and Hang Hu for tolerant my stupid questions and keep working with me in the past two years. I have also learned a lot from the visitors, senior postdocs and younger students in the group, Dr. Luna Huang, Dr. Yutaka Oya, Dr. Chad Hoyer, Dr. Andrew Valentine, Shichao Sun,

Ryan Beck, Andrew Wildman, Torin Stetina, Lauren Koulias and all others, thank you for the discussions and all funny stories.

I feel fortunate and being grateful to work with many great scientists inside and outside the department during my Ph.D. I would like to thank Prof. Alex Jen, Prof. Daniel Gamelin, Prof. David Ginger, Prof. Xin Zhang, Dr. Mike Frisch, Prof. Filippo Lipparini, Prof. Benedetta Mennucci for the opportunities and their trust. I also want to thank the people I closely worked with in their groups: Dr. Carl Brozek, Dr. Zonglong Zhu, Dr. Chu-Chen Chueh, Dr. Daniel Kroupa, Dr. Sidney Creutz, Dr. Sae-Byeok Jo, Dr. Ting Zhao, Dr. Susanne Birkhold, Dr. Ke Gao, Dr. Weifei Fu, Dr. Yu Liu, etc. You taught me a lot of chemistry, and set a high standard of academia research for me.

I would like to thank Dr. Mike Frisch from Gaussian Inc. for offering me opportunity to learn programming and electronic structures with him and visit New England eight times.

I also want to thank my undergraduate advisor Prof. Xin Xu and department chair Prof. Xiang Gao at Fudan University for cultivating my enthusiasm of science. I don't know what potential they saw from a low GPA, unconfident sophomore, but eventually, their trust and support were not in vain. Thank you.

I would also like to thank my friends, Zaiyuan, Haijie, Chenyuan, Chao, Jiale, Jiayu, Yandong, Jiaye, and Wenjie for all-the-time immediate response to my complains and emotions. Your encouragements are invaluable.

I would like to thank my parents for teaching me all characteristics of being a nice and kind person. Especially to my father, who also taught me being strong and optimistic. He has been diagnosed hcc and gallbladder cancer two years ago, and he is still fighting with them. He is a warrior, he is my hero.

Finally, I would like to thank my wife, Jingyi. We have seen happiness and frustration through each other in the past five years. We survived those tough times. This would not have happen without your firm support and lasting companionship. Thank you!

DEDICATION

to my parents, Jian Liu and Fengying Xue

and wife, Jingyi Ren

Chapter 1

THEORETICAL PRELIMINARIES

1.1 Quantum Mechanics and Wave Function

The postulates of quantum mechanics establish that a pure state of a given system is described by a state or ket vector, $|\Psi_i\rangle$, belonging to a mathematically well-defined vector space, i.e., the Hilbert space denoted by $\mathcal{H}$. Such vector is defined as a wave function and the inner product on $\mathcal{H}$ is defined as an expectation value. Here we simply mention that $\mathcal{H}$ is a vector space defined on the complex numbers set: it has the inner or scalar product defined; it has an infinite dimension; and it is complete. This last property is especially important and means that, for any vector $|\Psi_i\rangle \in \mathcal{H}$, there exists a family of infinite and complex numbers, $\{c_{ki}\}$, and an infinite family of vectors, $|\Phi_k\rangle$ to satisfy

$$|\Psi_i\rangle = \sum c_{ki} |\Phi_k\rangle \tag{1.1}$$

Now, recall that the goal of all quantum chemical methods is to obtain approximate solutions to the eigenvalue problem defined by the time-dependent Schrödinger equation

$$i\hbar \frac{d}{dt} |\Psi_i\rangle = \hat{H} |\Psi_i\rangle \tag{1.2}$$

And in most cases, Eq. (1.2) can be further simplified to a general time-independent equation if we only care about the ground state properties of a static system:

$$\hat{H} |\Psi_i\rangle = E_i |\Psi_i\rangle \tag{1.3}$$

where $\hat{H} = \hat{T} + \hat{V}_{Ne} + \hat{V}_{ee}$ is the usual electronic Hamiltonian hermitic operator in the Born−Oppenheimer approximation and includes the kinetic energy of the electrons ($\hat{T}$), the nucleus−electron potential ($\hat{V}_{Ne}$), and the electron−electron repulsion ($\hat{V}_{ee}$).

1.2 Hartree-Fock Theory

Hartree-Fock theory is one of the most important approximations in the electronic structure method. The simplest N-electron wave function that can be imagined consists of a single Slater determinant.

$$|\Psi_0\rangle = \frac{1}{\sqrt{N!}}\det|\psi_i\psi_j...\psi_N\rangle \tag{1.4}$$

The HF ground-state energy is determined by minimizing the energy functional $E_0 = \langle\Psi_0|\,\hat{H}\,|\Psi_0\rangle$ with the constraint that the orbitals remain orthogonal to each other. This is done by setting the linear variation in the following Lagrangian to be zero

$$\mathcal{L} = \langle\Psi_0|\,\hat{H}\,|\Psi_0\rangle - \sum_{ij}\epsilon_{ij}(\langle\psi_i\,|\,\psi_j\rangle - \delta_{ij}) \tag{1.5}$$

where i, j are Lagrange multipliers and $\langle\psi_i\,|\,\psi_j\rangle$ is the overlap between two orbitals. Evaluating the conditions that make the variation zero leads to a set of one-electron eigenvalue problems

$$\hat{f}\psi_i = \epsilon_i\psi_i \tag{1.6}$$

where $\hat{f}$ is the well-known one-electron Fock operator, the sum of the kinetic energy, nuclear attraction energy, and Coulomb and exchange effective potential operators. These effective potentials average the interaction with the rest of the electrons and is given by the orbitals themselves. Therefore, Eq. (1.6) must be solved in a self-consistent way. It is usually transformed to a matrix form by expanding the orbitals in a given atomic orbtial (AO) basis. These molecular orbitals are often described as linear combinations of atomic-orbitals (LCAO). The spatial part of the spin orbitals are expanded in a finite set of atomic orbital (AO) basis functions

$$\psi(r) = \phi(r)\sigma(\omega) \tag{1.7}$$

$$\phi(r) = \sum_{\mu=1}^{M} C_{\mu k}\chi_{mu}(r) \tag{1.8}$$

where $C_{\mu k}$ are molecular orbital (MO) coefficients and $\chi_\mu(r)$ are the basis functions. The basis functions are usually nuclei centered Gaussian or Slater-type functions[14], but in some software packages they are plane waves [24] or numerical basis[328].

The stationary condition of Eq. (1.5) can be satisfied by solving the generalized eigenvalue problem

$$\mathbf{FC} = \mathbf{SCE} \tag{1.9}$$

where $\mathbf{C}$ is the matrix representation of the aforementioned $C_{\mu k}$, *i.e.*, MO coefficients. and $\mathbf{S}$ is the overlap matrix now appearing because the basis set orbitals are centered in different nuclei, hence, are not orthogonal. The matrix in Eq. (1.9) is also solved iteratively, and the whole procedure is termed the self-consistent field (SCF) method. An important remark here is that since a variational approach is used, the HF scheme is aimed at approximating the ground-state wave function only.

1.3 Density Functional Theory

The Hartree-Fock theory described in the previous section provides reasonable approaches to obtain the wave functions from the time-independent Schrödinger equation, Eq. (1.3). From the approximate wave function the total energy can be obtained as an expectation value, and the different density matrices, in particular the one-particle density matrix, can be obtained in a straightforward way as

$$\rho_0(\vec{X}) = N \int \Psi_0^*(\vec{X}_1\vec{X}_2, ..., \vec{X}_N)\Psi_0(\vec{X}_1\vec{X}_2, ..., \vec{X}_N)d_{\vec{X}_2}...d_{\vec{X}_N} \tag{1.10}$$

where the subindex zero indicates that this is the ground-state density arising from the ground-state wave function Ψ_0. The integration in Eq. (1.10) is carried out for the spin and space coordinates of all the rest of electrons. In 1964 Hohenberg and Kohn proved a theorem that states that in certain conditions the inverse of this proposal also holds. [113] They proved that for a non-degenerate ground state the one-electron density determines the electronic Hamiltonian and wave function. They have also proven that for any N-electron system, there exist a universal functional to satisfy that the total energy is a functional of the

density. The resulting theoretical framework is nowadays referred to as density functional theory or simply DFT. [230] The foundation of DFT is further consolidated by the second theorem of Hohenberg and Kohn, which is a variational theorem stating that the ground-state energy is a minimum for the exact density.

Later, Kohn and Sham proposed a general framework which permits the practical use of DFT.[146] The Kohn-Sham formalism assumes that for any real system of electrons, there is a fictitious system on N non-interacting electrons experiencing the real external potential and showing exactly the same electron density as the real system. This allows one to define a convenient reference of N one-electron systems as a Slater determinant. In this way DFT permits handling of discrete and periodic systems (vida infra). The reference system allows a trial density to be obtained, but one still needs to compute the energy of the real system,

$$E[\rho] = T_s[\rho] + V_{\mathrm{Ne}}[\rho] + V_{\mathrm{Coulomb}}[\rho] + V_{\mathrm{XC}}[\rho] \tag{1.11}$$

The first term is the kinetic energy of the noninteracting electrons, the orbitals are re-introduced through the Slater determinant to better describe the kinetic energy.

$$T_s[\rho] = -\frac{1}{2}\sum_{i}^{N} \langle \psi_i | \nabla^2 | \psi_i \rangle \tag{1.12}$$

the second term accounts for the contribution of the nuclei attraction,

$$V_{\mathrm{Ne}}[\rho] = \sum_{A} \int d\mathbf{r} \frac{Z_A \rho(\mathbf{r})}{|\mathbf{R}_A - \mathbf{r}|} \tag{1.13}$$

and the third one corresponds to the Coulomb repulsion

$$V_{\mathrm{Coulomb}}[\rho] = \frac{1}{2}\iint d\mathbf{r} d\mathbf{r}' \frac{\rho(\mathbf{r})\rho(\mathbf{r}')}{|\mathbf{r} - \mathbf{r}'|} \tag{1.14}$$

Finally, the fourth term accounts for all the remaining effects, *i.e.*, the contribution to the kinetic energy due to the fact that electrons are interacting, the exchange part due to the Fermi character of the electrons, and the correlation contribution of the electron densities. The Kohn-Sham form of DFT is solved in the almost same way as HF. A Lagrangian is

formed with the constraint that the orbitals remain orthogonal to each other.

$$\mathcal{L} = E_{\mathrm{DFT}}[\rho] - \sum_{ij} \epsilon_{ij}(\langle \psi_i \mid \psi_j \rangle - \delta_{ij}) \tag{1.15}$$

The stationary condition that makes the variation in this Lagrangian zero leads to

$$\hat{f}^{KS}\psi_i = \epsilon_i \psi_i \tag{1.16}$$

where a unitary transformation has made the Lagrange multipliers diagonal. The Kohn-Sham operator can now be defined as

$$\hat{f}^{KS}(r) = \hat{h}(r) + \int dr' \frac{\rho(r')}{|r - r'|} + v_{xc}(r) \tag{1.17}$$

where

$$v_{xc}(\mathbf{r}) = \frac{\partial E_{xc}[\rho]}{\partial \rho(\mathbf{r})} \tag{1.18}$$

Even though the universal functional form is unknown, there have been tremendous efforts of developing approximated exchange-correlation functionals within KS theory to address different problems over the past twenty years. DFT has already become almost the standard choice for electronic structure calculations on molecules, clusters, surfaces, and solids, with thousands of papers published and new, improved, and more accurate functionals proposed almost every year.

1.4 Atomic Orbital Basis

Both HF and DFT require solving the generalized eigenvalue problem under concept of orbitals, which are a set of mathematical functions commonly named basis set. Although, as previously mentioned, any basis set that sufficiently spans the space of electron distribution could be used, the concept of Molecular Orbitals as Linear Combinations of Atomic Orbitals (LCAO) suggests a very natural set of basis functions: Atomic-Orbital (AO)-type functions centered on each nuclei. One obvious choice are the exact hydrogen AO's, known as Slater-type orbitals (STO), describing the radial component of the functions. However, the

computation of the integrals is greatly simplified by using Gaussian-type orbitals (GTO) for basis functions. GTOs are widely used in the computation from atom to molecules to even large metal clusters. The most popular ones are split valence basis set, *e.g.*, 6-31G, proposed by Pople [61] and correlation consistent basis set, *e.g.*, cc-pVDZ, proposed by Dunning. [72]

1.5 Pseudopotential, Plane-wave, and Periodic Boundary Condition

The re-introduction of the orbitals in the KS framework makes DFT again depends on the number of electrons and orbitals in the systems. The computational cost scales cubically with the number of basis functions in the system and causes numerical troubles when the system size is very large, for instance, metal solids. Therefore, a lot of techniques have been introduced and invented to reduce the dimension of the generalized eigenvalue problems.

The pseudopotential is an attempt to replace the complicated effects of the motion of the non-valence electrons of an atom and its nucleus with an effective potential, so that the Schrödinger equation contains a modified effective potential term instead of the Coulombic potential term for non-valence electrons normally found in the Schrödinger equation. The projector augmented wave methods (PAW) is a generalized method of the pseudopotential that assists the DFT to performed with greater computational efficiency.[24] Compared to other pseudopotential methods, PAW improves accuracy for magnetic materials, alkali and alkali earth elements, 3d elements, lanthanides and actinides.

Besides pseudopotentials, periodicity must be adopted to model the infinite expanded bulk metals and semiconductors. The extended system may be represented by a single unit cell. The interactions within the unit cell can be computed as per normal quantum chemistry method, while the interaction between the unit cells can be solved through Born-von Kármán equation:

$$\Psi(r + N\bar{a}) = \Psi(r) \tag{1.19}$$

where N is an integer, $\bar{a}$ is the lattice vector. Equation (1.19) can be easily satisfied if the plane-wave basis set is utilized to represent the one-electron wave-function.

$$\psi_{n\mathbf{k}}(r) = e^{i\mathbf{k}r} u_{nk}(r) \tag{1.20}$$

in which n is the band (orbital) index and $\mathbf{k}$ is the planewave vector. In software packages like VASP, it adopts all aforementioned techniques to fix the core electrons, using pseudopotentials, and and expand the valence-and-above Kohn-Sham orbitals using plane-waves under periodic boundary conditions. Those settings assure accurate, but rather fast calculations of infinite expanded metal and semiconductor systems.

1.6 Summary

With the advances of modern computers, the HF and DFT (mostly DFT) methods have been widely used in chemistry, both to serve as the rationalization of experiments and the prediction of novel chemical and physical properties. Nowadays, a modern high-performance computer cluster can roughly handle DFT calculations within one thousand atoms. Numerous efforts has been devoted to use DFT to study the electronic, optic, and magnetic properties in nanomaterials.

For some system like quantum dots or metal clusters with no obvious periodicity, DFT calculations are usually performed using atomic orbital basis using software like Gaussian. On the other hand, for systems with obvious periodicity, like several hundred nanometer semiconductor crystal grains, even though they are still in the nanometer scale, quantum confinement effect merely appear on such sizes. It is generally reasonable to treat those systems using a plane-wave basis with periodic boundary conditions. VASP is the most commonly used software to perform these DFT calcualtions.

However, one need always keep in mind that in the whole realm of electronic structure theory, DFT serves more like a compromise between the accuracy and computational affordability. One can easily find a nanomaterial system whose physical nature is far beyond the capability of conventional DFT (heavy metal clusters who has significant zero-field splitting) or a nanomaterial system which is too large and complicated to be handled by DFT with the current computation resources (usually quantum dots whose radii are larger than 2 nm).

This dissertation stands for the effort of modelling nanomaterials using DFT and beyond. The following of this dissertation will be divided into four part. In Chapter 2, I will discuss several examples of using conventional DFT to predict the chemical and physical properties in the bulk and interface of semiconductors. Chapter 3 focuses on improving the tractability of electronic structure methods like HF and DFT, I will discuss the demand and solution of calculating even larger non-periodic nanomaterial systems, e.g., quantum dots containing over 10,000 atoms.Chapter 4 and 5 focuse on pursuing the description of highly accurate wave functions beyond the DFT method, I will focus on the recent development of some post-HF electronic structure methods. The new methods has been implemented in an efficient and computationally economical fashion which makes it possible to be applied to the nanomaterial systems.

Chapter 2

MODELING NANOMATERIAL WITH DENSITY FUNCTIONAL THEORIES

The past twenty years have witnessed a rapidly growing demands of a in-depth understanding of materials from the atomistic level. More and more experimentalists rely on computation insights to optimize material design processes and rationalize novel phenomena to the fundamental physics. As the most frequently used tool in the computational toolbox, DFT has been extensively used to reveal the energetics and band structures of materials. In this chapter, I am showing two examples of using conventional DFT to model nanomaterials. In the first example, an AO and plane-wave combined DFT approach is used to 1) optimize the geometries of the $FA_xPEA_{1-x}PbI_3$ on the grain boundary. 2) help rationalize the structural and composition influence on the stability of $FA_xPEA_{1-x}PbI_3$ perovskite. In the second example, a plane-wave based DFT investigation has been carried out to profile the defect properties in the trivalent metal ion doped $CsPbCl_3$ perovskites. The first part of this chapter is adapted with the permission from Nan Li, Zonglong Zhu, Chu-Chen Chueh, Hongbin Liu, Bo Peng, Alessio Petrone, Xiaosong Li, Liduo Wang, Alex K-Y Jen, *Adv. Energy Mater.* **2017**, *7*, 1601307. Copyright ©2016 WILEY-VCH Verlag GmbH & Co. KGaA, Weinheim. [169]

2.1 Modeling Phase Stability in Mixed Cation Lead Iodide Perovskites

2.1.1 Introduction

Recently, organic-inorganic metal halide perovskites have drawn tremendous research attention among the photovoltaic (PV) community due to their superior semiconducting properties and facile solution processability.[50, 322, 283, 104] To date, the dynamic research

efforts have resulted in very high power conversion efficiency (PCE) in derived perovskite solar cells (PVSCs) with the highest certified PCE reaching 22.1%, which is on par with other high-performance inorganic solar cells.[309] Three-dimensional (3D) hybrid organic-inorganic perovskites are materials with a ABX_3 crystal structure, where A^+ is an organic cation or cesium cation (Cs^+), B^+ is a metal cation, and X^- is a halide anion, respectively. [95, 128, 133, 229, 280, 285] In principle, the electronic band structures of a hybrid perovskite are governed by the electronic orbitals of B^+ and X^- ions, while A^+ ions are mainly responsible for keeping the electro-neutrality and cohesion of the lattices.[320, 321] Therefore, the A^+ plays a critical role in affecting the symmetry of perovskite lattice and the associated phase transformation, which will also influence the resulting band structures and relevant optoelectronic properties.[182, 202, 325, 326, 308] In general, if the size of A^+ is too large, the 3D framework of ABX_3 will be transformed into a lower dimensional crystal structure, such as a 2D layered structure.[279, 48, 26] Currently, methylammonium lead iodide ($MAPbI_3$) is the most commonly studied perovskite composition for high-performance PVSCs.[271, 34, 162, 247, 223] However, there are several issues that need to be addressed, such as the photo- and thermal-stability of $MAPbI_3$.[309, 324] This is attributed to its low crystallization energy and low temperature phase transformation between the tetragonal and cubic phase at 320K.[182, 282, 312] Hence, a significant part of research focus has been shifted to engineer the perovskite compositions for achieving optimal material systems.[77, 232, 160, 6, 296] In this regard, formamidinium lead iodide ($FAPbI_3$) has been vigorously investigated due to its broader light absorption that extends to near infrared (NIR) region, higher decomposition temperature (over 150 $°C$), and decent charge diffusion length compared to $MAPbI_3$.[77, 232, 160, 6, 296] However, the phase-purity and -stability of pristine $FAPbI_3$ have also been found as a significant hurdle for developing efficient and stable PVSC. The relatively easy conversion of black α-phase $FAPbI_3$ into yellow non-perovskite δ-phase limits the resultant photovoltaic performance and long-term stability of devices.[3, 106, 68] These deficiencies need careful investigation to improve their applicability for practical solar cells.[263, 173, 159, 318] Several research groups have recently unveiled

that phase instability of $FAPbI_3$ can be effectively modulated by employing the mixed-cation strategy to form perovskites. For example, by mixing FA^+ with a smaller cation like MA^+ or Cs^+ into $FAPbI_3$, the lattice contraction introduced by the added small cations not only can facilitate the formation of α-phase but also retard its relaxation back to δ-phase.[317, 19] As a result, the current state-of-the-art mix-cation MA^+/FA^+ based PVSC showed a very high PCE of 21%.[20] Despite the vigorous progress, the FA-based perovskites still suffer from unsatisfied moisture stability as a result of their easy hydration with H_2O.[164] Therefore, it is imperative to simultaneously improve both their phase and ambient stability.[210, 212] As mentioned earlier, a 2D layered perovskite will form if the size of the employed A^+ exceeds the tolerance space of a 3D perovskite framework. For example, the phenylethylammonium iodide (PEAI) has been used to form 2D PEA_2PbI_4 perovskite, wherein a bilayered PEA^+ self-assembles along the inorganic sheet consisting of metal halide octahedron.[264, 211] This 2D structure yields a better ambient stability than that of the 3D counterpart due to the stronger interlock between the organic and inorganic species.[245, 35] Based on this principle, several reports have recently described the intercalation of PEA^+ into $MAPbI_3$ to form 2D/3D (or quasi-3D) hybrid perovskites with improved ambient stability.[176, 144] The inserted PEA^+ can break the 3D perovskite framework to result in quasi-3D perovskite structures with hydrophobic PEA formed on the surface to improve the ambient stability of resultant perovskites. In this work, different from the explored strategy of incorporating a smaller cation, MA^+ or Cs^+, into $FAPbI_3$ lattice, the larger PEA^+ was incorporated into $FAPbI_3$ perovskite to form $FA_xPEA_{1-x}PbI_3$ to demonstrate enhanced phase and ambient stability in addition to obtaining higher photovoltaic performance in derived PVSC. From both experimental results and theoretical calculations, the $FA_xPEA_{1-x}PbI_3$ phase stability was shown to greatly improve in quasi-3D perovskite at room temperature. We hypothesize that PEA^+ might migrate into the $FAPbI_3$ grain boundaries to form a self-assembled organic shell with induced $\pi - \pi$ interactions, raising the phase transition energy and enhance its phase stability. In addition, the hydrophobicity of self-assembled PEA^+ layer helps prevent moisture from interacting with $FA_xPEA_{1-x}PbI_3$. The PEA^+ and its I^- counterion can also

passivate the surface defects of perovskites to enhance device performance. As a result, a high-performance (PCE: 17.7%) solar cell with superior phase and ambient stability was successfully demonstrated.

2.1.2 Results and Discussion

A sequential two-step deposition procedure is employed to process the $FA_xPEA_{1-x}PbI_3$ films in this study (Fig. 2.1a), where a PbI_2 layer is formed initially then the FAI or FAI/PEAI mixed solution is deposited on top of layered PbI_2 to convert it into perovskites. The detailed process information is described in the experiment section. By adopting this 2-step procedure, the inter-diffusion of FAI/PEAI into the pre-deposited PbI_2 matrix can modulate the PEA^+ distribution and self-assembly on both the top surface and grain boundaries of $FAPbI_3$ through distinct diffusivity and van de Waals interactions between FA^+ and PEA^+.[144, 201]

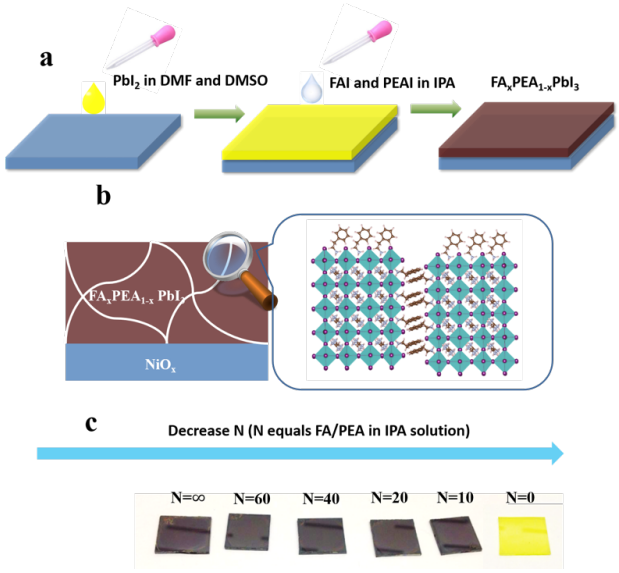

Figure 2.1: Schematic drawing of (a) the deposition of $FA_xPEA_{1-x}PbI_3$ films in this study. (b) The formation of quasi-3D $FA_xPEA_{1-x}PbI_3$ crystal. (c) Photographs of the prepared $FA_xPEA_{1-x}PbI_3$ films, where N is the molar ratio of FA^+ to PEA^+.

Previous reports have shown that the incorporation of larger organic cations can result in mixed 2D/3D perovskites with their crystal growth direction perpendicularly oriented to the substrate.[144, 201] Fig. 2.1b illustrates the schematic drawing of self-assembled PEA^+ in perovskite films. The PEA layer can form both on the lattice surface and within the grain boundaries via self-assembly to form quasi-3D perovskite structures. Different molar ratios (N) of FAI to PEAI could be adjusted by adding PEAI into the FAI solution. A yellow 2D PEA_2PbI_4 film will form if only a pure PEAI precursor solution is added (Fig. 2.1c). Fig. 2.2 shows the top-sectional scanning electron microscopy (SEM) images of the prepared $FA_xPEA_{1-x}PbI_3$ films. All of them exhibit a smooth and homogenous morphology without any pinholes or severe aggregations but only with slightly different grain sizes. Such high quality films are critical for their performance in derived PVSC.

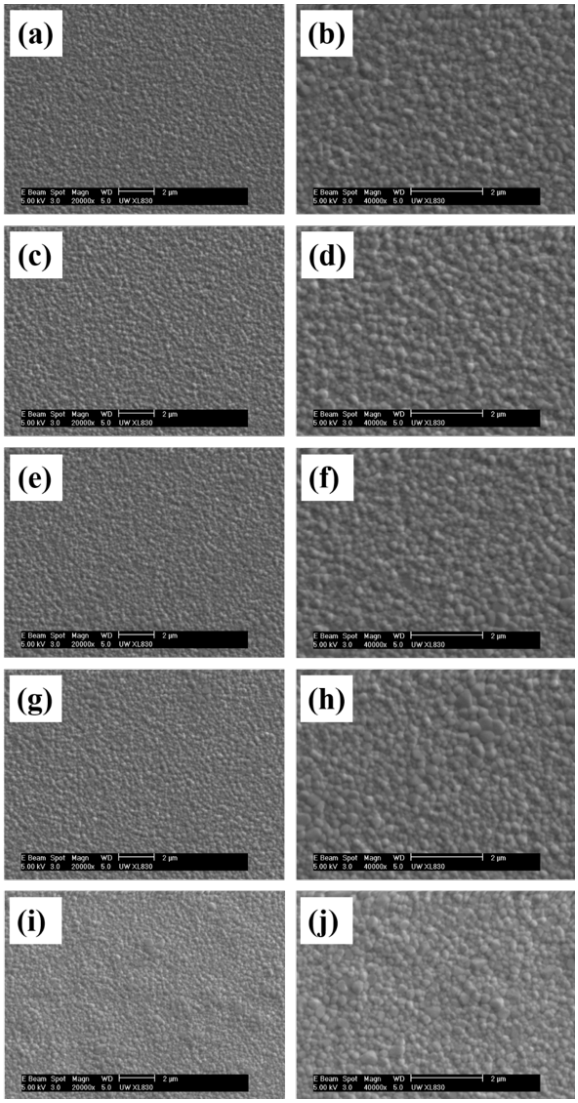

Figure 2.2: Top SEM images of FAPbI3 and $FA_xPEA_{1-x}PbI_3$ films with different magnifications. (a,b) $FAPbI_3$, (c,d) N = 60, (e,f) N = 40, (g, h) N = 20, and (i, j) N=10. N is the molar ratio of FA^+ ion to PEA^+ ion.

The absorption spectra of prepared $FA_xPEA_{1-x}PbI_3$ films are presented in Fig. 2.3a. As shown in the spectra, the $FA_xPEA_{1-x}PbI_3$ films possess similar profile with an absorption band-edge around 820 nm, indicating the formation of quasi-3D crystalline $FAPbI_3$ domains instead of 2D PEA_2PbI_4 (N = 0) domains. In addition, the total absorbance of

$FA_xPEA_{1-x}PbI_3$ films with N between 20 and 60 increases compared to that of the pristine $FAPbI_3$ (N = ∞), suggesting the addition of a small amount of PEA^+ improves the crystallinity of $FAPbI_3$. However, as more PEA^+ is added, the absorption of the prepared films decreases, which may be attributed to the excess larger-sized PEA^+ hindering FA^+ from diffusing into the PbI_2 layer.

The corresponding X-ray diffraction (XRD) patterns are displayed in Fig. 2.3b. For all the quasi-3D $FAPbI_3$ films, the characteristic peaks of 13.8°, 24.2°, 28°, and 31.5° can be assigned to the scattering from (111), (021), (222) and (123) crystal planes, which are apparently distinct to the characteristics of 2D PEA_2PbI_4. The full width at half maximum (FWHM) of the peak at 13.8° (Fig. 2.3c) was further estimated. The gradually decreased FWHM indicates the enhanced crystallization of $FAPbI_3$ as a result of PEAI addition. The enhanced crystallization may be due to the facilitated vertical growth of perovskite as reported in the literature,[7a, 22b] or the self-assembled PEA^+ at the grain boundaries behaving like molecular locks to strengthen the intermolecular interactions of $FAPbI_3$ domains.[144, 117]

To confirm the presence of PEA^+ in the prepared $FA_xPEA_{1-x}PbI_3$ films, we have further applied the Fourier transform infrared spectroscopy (FTIR). In the FTIR spectra (Fig. 2.3d), the feature peak of the alkenyl C=C stretching vibrations from the benzene ring of PEA^+ can be clearly seen at 1600 cm^{-1} and its intensity rises as the amount of incorporated PEA^+ increases. Figure 2.3e and f show the X-ray photoelectron Spectroscopy (XPS) results of the $FA_xPEA_{1-x}PbI_3$ films processed with N = 10, 40, ∞, respectively. There is no shift of the feature peaks in the XPS spectra of $FA_xPEA_{1-x}PbI_3$ films, suggesting the $FAPbI_3$ lattice parameter does not change after incorporating PEA^+, which is in agreement with the UV-vis absorption and XRD results, validating the formation of quasi-3D $FAPbI_3$ as illustrated.

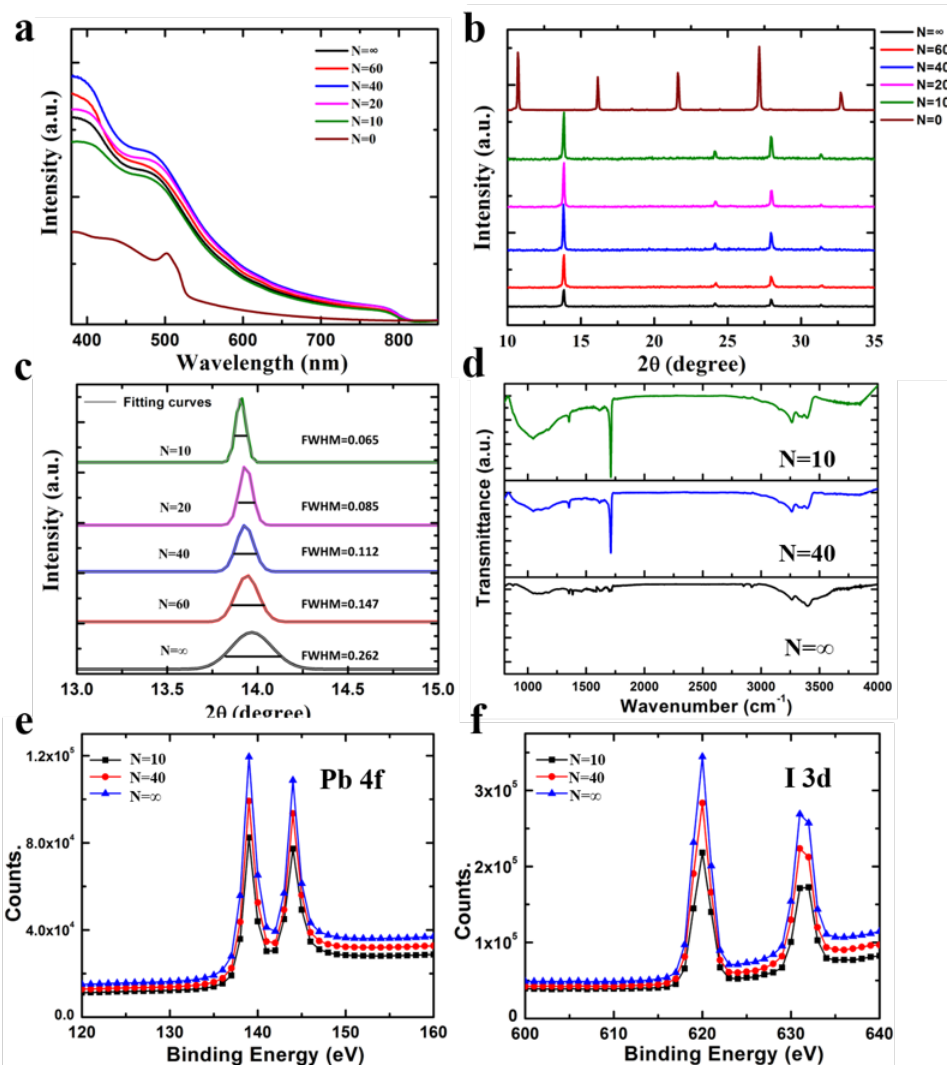

Figure 2.3: (a) Optical absorption spectra, (b) XRD patterns, (c) magnified (111) peak of XRD patterns, (d) FTIR spectra, and (e) Pb $4f$ and (f) I $3d$ XPS spectra of the studied $FA_xPEA_{1-x}PbI_3$ films.

The phase and ambient stability of prepared $FA_xPEA_{1-x}PbI_3$ films are investigated to understand the effect of PEA^+ incorporation on the films stability. All the prepared films were kept in ambient with a relative humidity of around 40±5%. Figure 2.4a shows the corresponding UV-vis spectra recorded at different storage times in ambient. The pristine $FAPbI_3$

decomposes totally into yellow phase after being stored for 30 days while the $FA_xPEA_{1-x}PbI_3$ film (N = 40) shows much better ambient stability. The pictures of degraded films are presented in Fig. 2.4b. The color of pristine $FAPbI_3$ changes from black into yellow after being stored in ambient for 30 days, while the color of the $FA_xPEA_{1-x}PbI_3$ film (N = 40) remains intact in black. Figure 2.4c and d illustrate the XRD patterns of those degraded films as a function of stored time in ambient, which unravels the possible degradation pathways of these films. The pristine $FAPbI_3$ first converted into δ-phase $FAPbI_3$ (characteristic peak at 11.7°) after 5 days storage in ambient, and then completely degraded into PbI_2 (characteristic peaks at 12.5°) after 30 days. On the contrary, the $FA_xPEA_{1-x}PbI_3$ film (N = 40) shows the retarded yellow phase transformation with only a relatively small amount of perovskite degraded into PbI_2 after 30 days in ambient.

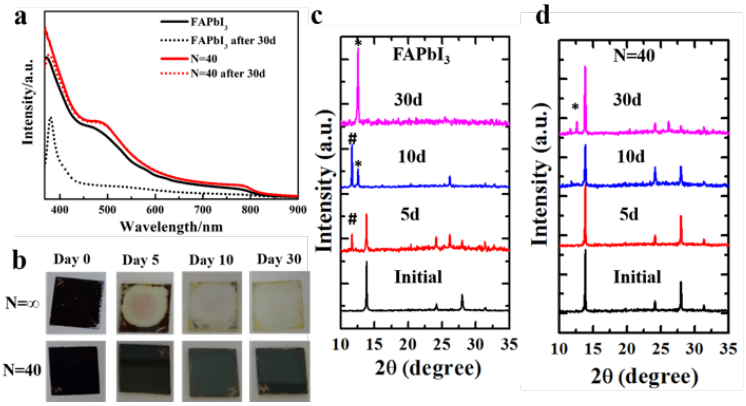

Figure 2.4: (a) Optical absorption spectra, (b) XRD patterns, (c) magnified (111) peak of XRD patterns, (d) FTIR spectra, and (e) Pb $4f$ and (f) I $3d$ XPS spectra of the studied $FA_xPEA_{1-x}PbI_3$ films.

To better understand the reason for the improved phase and ambient stability of $FA_xPEA_{1-x}PbI_3$ film, we resort to the density functional theory (DFT) simulation. On account of the sufficient characterizations, we propose that PEA^+ mainly penetrate into grain boundaries and substitute the FA^+ at the crystal surface. Based on this model, we first studied the stabil-

ity of α-phase $FAPbI_3$ by calculating the formation energy with different molar fractions of FA^+, and the detailed information is shown in the SI. By gradually substituting FA^+ with PEA^+ at the crystal surface, the formation energy of α-phase $FAPbI_3$ changes with different molar fractions of FA^+. The system reaches the most stable state of phase with the highest formation energy when the FA^+ molar fraction is around 95% to 96% (Fig. 2.5).

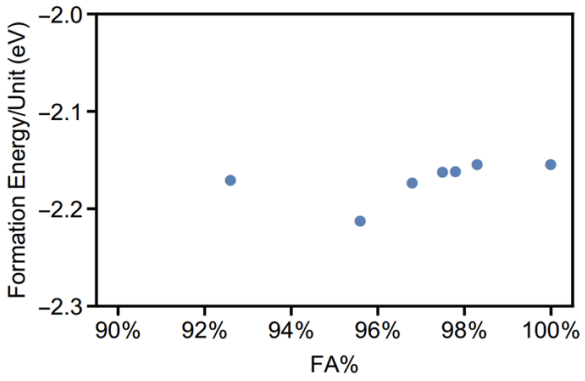

Figure 2.5: The formation energy change in accordance with the increase of the FA^+ mole fraction in the black phase.

Based on these calculations, we hypothesize the reason for improved phase stability of $FA_xPEA_{1-x}PbI_3$ film. The α- and δ-phase of $FAPbI_3$ lattices have very similar building layers parallel to the ab plane, which are highlighted with yellow circles in Fig. 2.6a and b. The significant difference is that the α-phase $FAPbI_3$ has one more FAI layer inserted in its supercell structure, which is highlighted with the red circle. The black phase can turn into the yellow phase through some translations of different layers. The existence of PEA^+ on the (-111) surface increases the inter-layer distance and blocks some mismatch pathways, which could potentially raise the transition energy barrier from the black phase to the yellow phase as illustrated in Fig. 2.6c and d, thereby enabling the black phase to be more kinetically stable.

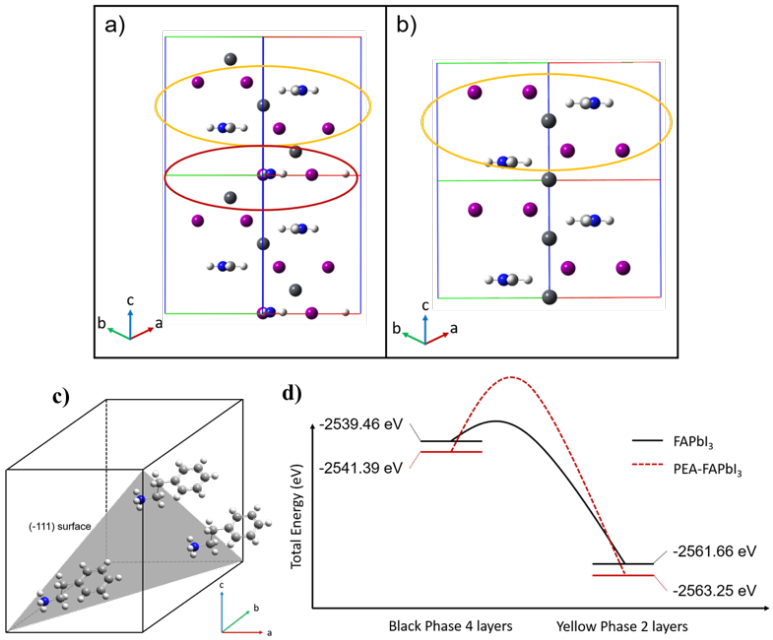

Figure 2.6: Material calculation: (a) The 1×1×2 supercell of black phase $FAPbI_3$. (b) The 1×1×2 supercell of the yellow phase $FAPbI_3$. (c) The PEA docking on the (-111) surface of black phase $FAPbI_3$ will prevent the layer translations or mismatch along the a, b, c directions. (d) The thermodynamic analysis and kinetic hypothesis using a 4-layer black phase $FAPbI_3$ to a 2-layer yellow phase $FAPbI_3$ transition (number of Pb atoms conserved) as an example.

The inverted p-i-n planar $FA_xPEA_{1-x}PbI_3$-based PVSCs were fabricated in the configuration of ITO/NiO_x/$FA_xPEA_{1-x}PbI_3$/PCBM/bis-C_{60}/Ag.[168, 136] Figure 2.7a shows a representative cross-sectional SEM image of the fabricated devices, wherein a thick perovskite layer (400 nm) was deposited on top of the NiO_x hole-transporting layer (HTL) (40 nm), followed by the deposition of a PCBM electron-transporting layer (ETL) (50 nm) and a thin bis-C_{60} surfactant layer (10 nm). The energy levels of the fabricated device illustrated in Fig. 2.7b show the well aligned conduction band minimum (CBM) and valence band maximum (VBM) of perovskite with the energy levels of employed ETL and HTL, respectively, which ensures the efficient charge transport and collection in the device.

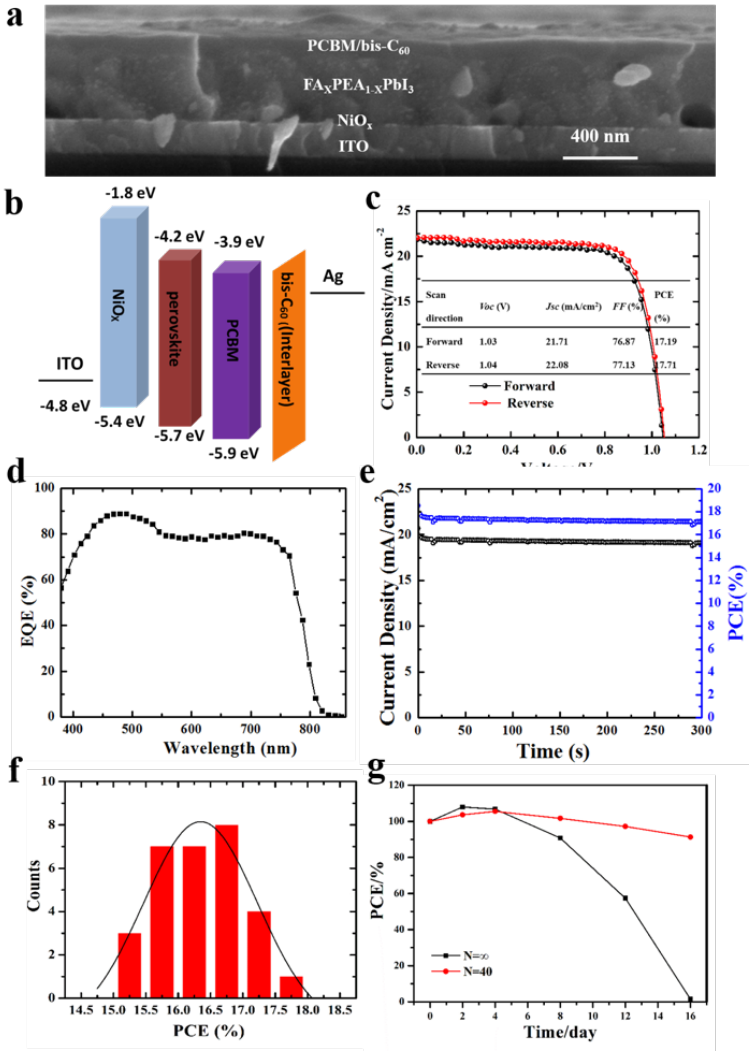

Figure 2.7: (a) The cross-sectional SEM image of the fabricated device. (b) The energy level diagram of the studied device with a structure of ITO/NiO_x/ $FA_xPEA_{1-x}PbI_3$/ PCBM/bis-C_{60}/ Ag. (c) The J-V curve, (d) EQE spectra, and (e) the stable out-put performance curve of $FA_xPEA_{1-x}PbI_3$ devices with the best performance. (f) The performance distribution of $FA_xPEA_{1-x}PbI_3$ (N = 40) devices. (g) The stability evolution of the derived PVSCs. Note the stabilized photocurrent density (black) and PCE (blue) shown in (e) is measured under a constant bias of 0.89 V near the maximum power point.

The best PCE of 17.71%, with a VOC of 1.04 V, a JSC of 22.08 mA/cm^2, and a FF of 77.14% is realized in the device based on a $FA_xPEA_{1-x}PbI_3$ with N=40 and shows negligible

hysteresis under the forward and reverse scans (Fig. 2.7c). The EQE spectrum is plotted in Fig. 2.7d, for which the integrated JSC agrees well with the value obtained in the J-V curve. A plateau of EQE around 80% across 400-750 nm is clearly observed, revealing the high photon-to-electron conversion of the fabricated device. To further confirm the reliability of the fabricated PVSC, the stabilized photocurrent measured at a constant bias of 0.89 V near the maximum power point is examined and presented in Fig. 2.7e. A steady-state PCE of 17.3% is clearly shown. Moreover, the solar cell efficiency histogram of this top-performing PVSC is evaluated along with the Gaussian fitting as illustrated in Fig. 2.7f, which unravels an average PCE of 16.4% over 35 devices with good reproducibility. Figure 2.7g shows that the ambient stability of the $FA_xPEA_{1-x}PbI_3$ (N=40) based device is greatly improved, which retains over 90% of its initial PCE after being stored in air for 16 days under a relative humidity of 40±5% without encapsulation. On the contrary, the PCE of pure $FAPbI_3$ based device decays to near zero after 16 days.

It is interesting to note that all the fabricated devices show similar series resistance (R_s) but distinctly different shunt resistance (R_{shunt}), which is relevant to the previously discussed favorable vertical crystal growth induced by the small amount of PEA^+ at the grain boundaries (Fig. 2.1b). The self-assembled PEA^+ layer can reduce the lateral charge leaking, thereby leading to increased R_{shunt} and FF.

Electrochemical impedance spectroscopy (EIS) has been widely used to measure the charge transport dynamics in solar cells, such as chemical capacitance, recombination lifetime, and transport properties.[22, 21, 102] As metioned, the PEA^+ should be located mainly at the perovskite surface and grain boundaries, which will also passivate the grain boundary defects.[176, 144, 117] To further elucidate the charge carieer dynamics in $FA_xPEA_{1-x}PbI_3$, we have measured the EIS for devices derived from $FA_xPEA_{1-x}PbI_3$ (N = 40, 60, and ∞). The Nyquist plots of these devices recorded at different applied voltages are shown in Fig. 2.8a-c. The frequency used for all EIS measurements is ranging from 0.5 Hz to 1 MHz. All devices were applied with a bias ranging from 0 V to 1 V. The arc at low frequencies has been assigned as the recombination process[27] and the obtained data was fitted based

on the commonly used equivaltent circuit model as shown in Fig. 2.8d, where a parallel bulk resistance (R_1)-chemical capacitance (C_1) sub-circuit was applied. R_2 represents the surface recombination resistance along with its related capacitance (C_2) forming another sub-circuit, and R_s, C_3 and R_3 represent the series resistance, geometric capacitance and internal resistance, respectively. The recombination process in device was investigated by evaluating its bulk charge recombination lifetime (τ_{rec}) from R_1 and C_1, and surface charge recombination lifetime ($\tau_{rec(surface)}$) from R_2 and C_2, respectively.[11, 105, 134, 273, 79, 71] Both τ_{rec} and $\tau_{\mathrm{rec(surface)}}$ can be derived from the equation $\tau_{rec} = R_{rec}C_{rec}$. The estimated τ_{rec} value for devices based on $FA_xPEA_{1-x}PbI_3$ (N = 10, 40, and ∞) is similar while the value of $\tau_{rec(surface)}$ varies significantly following the order of $FAPbI_3$ < $FA_xPEA_{1-x}PbI_3$ (N=40) < $FA_xPEA_{1-x}PbI_3$ (N=10). This result demonstrates that the recombination at the perovskite surface can be effectively suppressed by the intercalated PEA^+, proving its possible role in passivating the defects located among the grain boundaries.

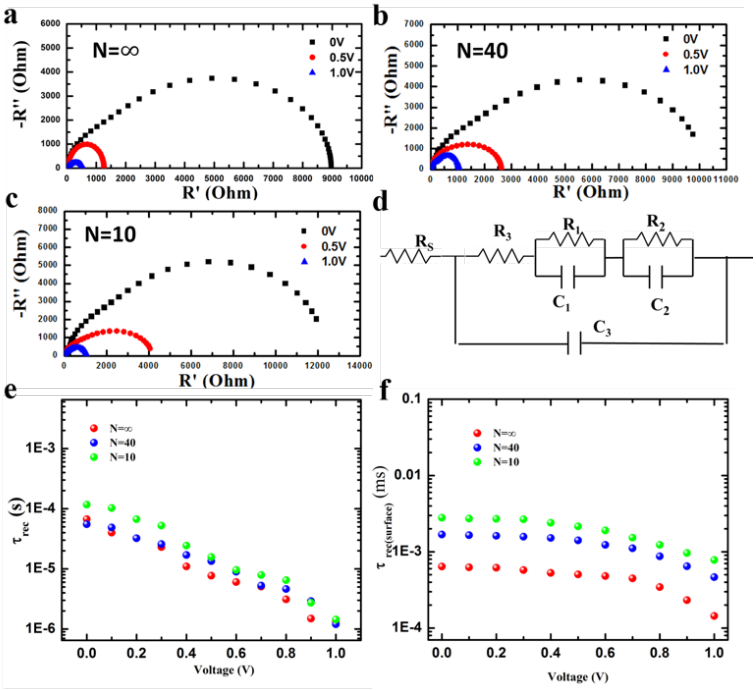

Figure 2.8: Impedance spectrum study. The representative Nyquist plots of whole regions of impedance spectra at different biases (0 V, 0.5V and 1.0 V) of (a) $FAPbI_3$, $FA_xPEA_{1-x}PbI_3$ ((b) N = 40 and (c) N = 10) based PVSCs. The equivalent circuit (d) is used for fitting the Nyquist plots. Plots a series of (e) bulk electron lifetime and (f) surface recombination time of $FAPbI_3$ and $FA_xPEA_{1-x}PbI_3$ (N = 40 and N = 10) based PVSCs.

2.1.3 Conclusion

In summary, we demonstrate that both phase and ambient stability of $FAPbI_3$ can be effectively enhanced by intercalating a larger cation PEA^+ into $FAPbI_3$ perovskite to form mix-cation $FA_xPEA_{1-x}PbI_3$ perovskites. PEA^+ can self-assemble at the grain boundaries of 3D perovskite grains to form quasi-3D perovskite structures, behaving as molecular locks to strengthen the intermolecular interactions of $FAPbI_3$. Consequently, the transition energy from the black phase to the yellow phase is raised, resulting in enhanced phase stability. In addition, the PEA^+ and its I^- counterion can also passivate the defects at grain boundaries with the hydrophobic PEA^+ on perovskite surface to enhance the ambient stability of the

perovskites. As a result, a high-performance $FA_xPEA_{1-x}PbI_3$ solar cell with a PCE as high as 17.7% could be demonstrated with superior phase and ambient stability.

2.2 Modeling Defects in Trivalently doped Lead Halide Perovskites

2.2.1 Introduction

Doped metal-halide perovskites are an emerging class of phosphors that combine the desirable broadband absorptive properties of perovskite semiconductors with the richly tunable color emission profiles of sensitized metal ion dopants. A variety of dopants have been incorporated into perovskites including transition metals (Mn^{2+}, Ni^{2+}, Cd^{2+}, Cu^{2+}),[180, 323, 213, 18] metalloids (Sn^{2+}, Bi^{3+}),[319] and lanthanides (Y^{3+}, La^{3+}, Ce^{3+}, Sm^{3+}, Eu^{3+}, Tb^{3+}, Dy^{3+}, Er^{3+}, Yb^{3+}).[4, 209, 155, 54, 228, 330] Among the trivalent lanthanides, ytterbium (Yb^{3+}) has proven to be an extraordinarily attractive luminescence activator in $CsPb(Cl_{1-x}Br_x)_3$. Yb^{3+} shows a single emission band centered around 1.3 eV, corresponding to $^2F_{5/2} \rightarrow {}^2F_{7/2}$ $f-f$ electronic transitions, which is well-aligned with the 1.1 eV band gap of silicon. Moreover, Yb^{3+}-doped $CsPb(Cl_{1-x}Br_x)_3$ nanocrystals and thin films exhibit photoluminescence quantum yields (PLQYs) that exceed 100%, stemming from a unique picosecond quantum-cutting process. For these reasons, quantum-cutting perovskites are extremely promising down-conversion materials for efficient solid-state lighting and solar photovoltaics.[330]

Previously, we hypothesized that aliovalent Yb^{3+} substitution at the B-site of $CsPbX_3$ stabilizes a proximal charge-compensating defect, and that these dopants and defects are electrostatically associated as a charge-neutral defect complex.[209] Based on literature precedent, we hypothesized a Yb^{3+}-V_{Pb}-Yb^{3+} motif in which two Yb^{3+} dopants are compensated by one intervening Pb^{2+} vacancy.[110, 208] This defect cluster was anticipated to play an integral role in the quantum-cutting mechanism in these materials: following $CsPbX_3$ photoexcitation, the defect complex was hypothesized to rapidly trap the excitation energy, thereby depopulating the exciton, and this trapped energy is then divided to excite two Yb^{3+} ions into their luminescent excited state. The existence of such a dopant-induced de-

fect has been confirmed by direct observation of shallow trap luminescence in lanthanum (La^{3+}) doped $CsPbCl_3$. While the spectroscopic signatures are evident, less is known about the structural properties of Yb^{3+} dopants in $CsPbX_3$. Here we apply a combination of computational analysis and chemical synthesis to more closely examine the microscopic defect structure of $CsPbX_3$ perovskites doped with trivalent metal ions.

2.2.2 Experiments

We prepared a series of M^{3+}-doped $CsPbCl_3$ bulk powders by solid-state mechanochemical grinding of stoichiometric metal-halide salts using an agate mortar and pestle. The resulting powders are composed primarily of the desired $CsPbCl_3$ phase as determined by powder X-ray diffraction, Fig. 2.9. Similar to previous reports on manual grinding of metal-halide perovskite semiconductors, excess precursor and other phases are also present in the product powder. Specifically, we detect excess $PbCl_2$ and a CsCl-rich Cs_4PbCl_6 phase in all samples studied here.

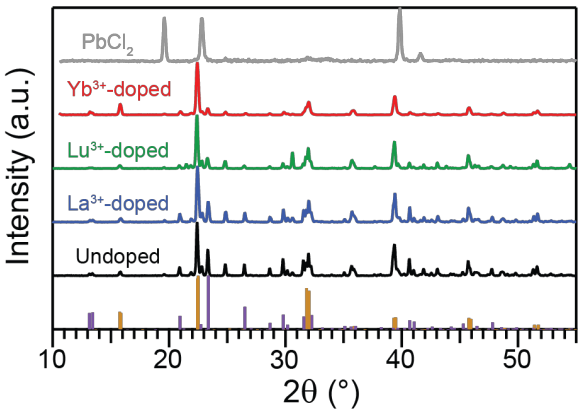

Figure 2.9: X-ray diffraction patterns for undoped (black), 3% La^{3+}-doped (blue), 3% Lu^{3+}-doped (green), and 3% Yb^{3+}-doped (red) $CsPbCl_3$ powders. Reference indices are for shown for *Pnma* $CsPbCl_3$ (orange) and $I4/mcm$ $CsPb_2Cl_5$ (purple).

Figure 2.10 presents photoluminescence (PL) spectra of undoped (black), 3% La^{3+}-doped

(blue) and 3% Lu^{3+}-doped (red) $CsPbCl_3$ powders at 45 K under 375 nm photoexcitation. The undoped sample shows characteristic band-edge emission centered at 2.97 eV and a broad emission band centered near 1.64 eV. This broad feature has previously been assigned to defect emission from lattice chloride vacancies. [143, 301] Similar to what has been observed for nanocrystals [209] and polycrystalline thin films. [155]

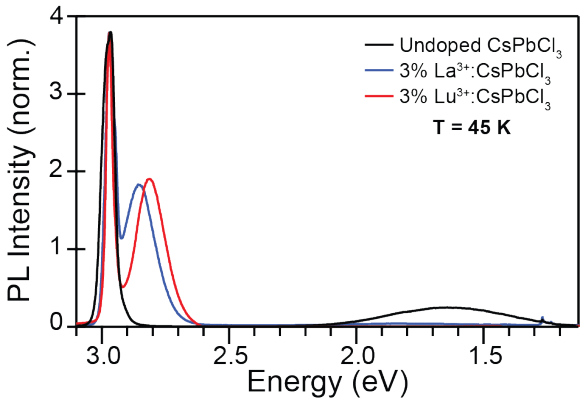

Figure 2.10: Photoluminescence spectra of undoped (black), 3% La^{3+}-doped (blue), 3% Lu^{3+}-doped (red) CsPbCl3 powders at 45 K under 375 nm photoexcitation.

La^{3+} and Lu^{3+} were selected as dopant candidates because they are optically inert with completely empty or full f orbitals, respectively. They also have the same charge-compensation requirements as Yb^{3+} with comparable ionic radii. Thus, introduction of La^{3+} and Lu^{3+} should introduce a similar microscopic dopant structure as Yb^{3+}, but should not introduce ion-specific emission. Instead, emergent emission features can be ascribed to dopant-induced defects. As shown in Fig. 2.10, incorporation of La^{3+} and Lu^{3+} also quenches the defect emission band at 1.64 eV. Beginning at 60 K, we observe the growth of a new band lower in energy than the exciton. This band peaks in intensity between 45 and 50 K and is rapidly quenched at temperatures lower than 40 K. Full temperature-dependent PL data for Lu^{3+}-doped $CsPbCl_3$ is included in the Fig. 2.11.

	Defect Binding Energy (eV)	m_e^*/m_e	Defect Bohr Radius (nm)
La^{3+}	0.114	0.138	1.56
Lu^{3+}	0.161	0.196	1.10

Table 2.1: The calculated defect Bohr radius of Lu^{3+} and La^{3+}-doped $CsPbCl_3$.

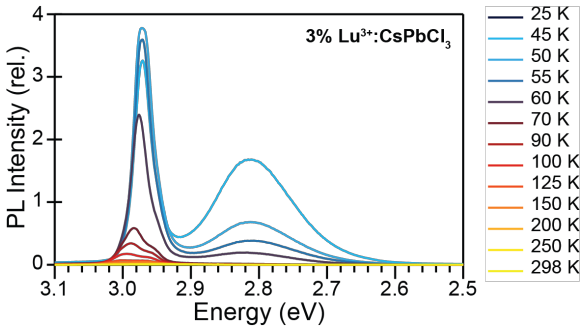

Figure 2.11: Temperature-dependent photoluminescence spectra of 3% Lu^{3+}-doped $CsPbCl_3$ powder under 375 nm photoexcitation.

We extracted the M^{3+}-induced defect binding energies by taking the peak difference between band-edge and induced-defect emission bands. The corresponding defect Bohr radii, assuming a dielectric constant, ϵ_r, of 4.07 for $CsPbCl_3$,[241] are calculated using Eq. (2.1) and Eq. (2.2) and reported in Tab. 2.1, where ΔE is the experimental measured Stokes shift.

$$\frac{m_e^*}{m_e} = \frac{8\epsilon_0^2 h^2}{m_e e^4} \times \Delta E \epsilon_r^2 = \frac{\Delta E \epsilon_r^2}{13.6} \tag{2.1}$$

$$\text{Defect Bohr Radius [nm]} = \frac{4\pi\epsilon_0\hbar^2}{e^2 m_e} \frac{\epsilon_r}{(\frac{m_e^*}{m_e})} = 0.053 \frac{\epsilon_r}{(\frac{m_e^*}{m_e})} \tag{2.2}$$

2.2.3 DFT Simulations

Density functional theory (DFT) calculations have been carried out to further investigate the effect of different M^{3+} dopant on the electronic structures of $CsPbCl_3$. Five dopants, Al^{3+},

Lu^{3+}, Yb^{3+}, Y^{3+}, La^{3+}, have been chosen in the computational modelling. The calculations start from a cubic $CsPbCl_3$ perovskite with a lattice constant of 5.727 Å. All electronic structure calculations are performed using the VASP software package with projector-augmented wavefunctions.[151, 150, 24] The calculations used the Perdew-Burke-Ernzerhof functional with an energy cut-off of 300 eV.[238] For Cs, Pb, and Cl atoms, $5s5p6s$, $6s6p$, and $3s3p$ valence electrons were explicitly treated, respectively. For the Al^{3+}, Y^{3+} dopants, the $3s3p$, $4s4p5s4d$ valence electrons were explicitly treated, respectively. For La^{3+}, Yb^{3+}, and Lu^{3+} dopants, the $6s5p5d$ were explicitly treated. We first optimized the $CsPbCl_3$ unit cell at a Γ-centered 6×6×6 k-point grid of the Brillouin zone. The total energy convergence is set to 10^{-6} eV and we assume the geometry relaxation converges when the max Hellman?Feynman force on each atom was below 0.001 eV/Å. A 5×5×5 supercell was then expanded based on the optimized unit cell structure. The density of states of the supercell was then calculated at a Γ-centered 3×3×3 k-point grid of the Brillouin zone. The band structure is calculated along all special k-points of the cubic lattice: Γ(0,0,0), X(0,1/2,0), R(1/2,1/2,1/2), M(1/2,1/2,0) [272]

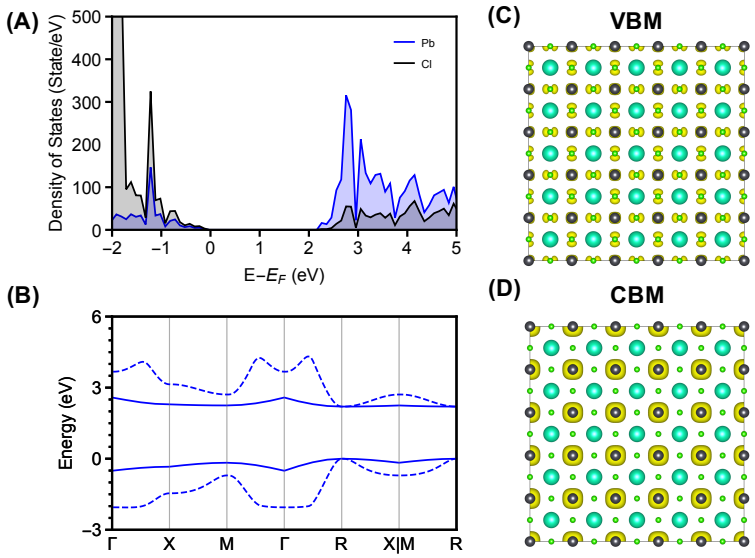

Figure 2.12: The electronic structures of undoped $CsPbCl_3$. (A) The density of states (B) The band structure (C) The wave function at VBM (D) The wave function at CBM of cubic $CsPbCl_3$. All calculations are done on a 5×5×5 supercell, containing 625 atoms (except the dash lines in B, which correspond to the band structures of the unit cell, containing only 5 atoms). The band gap is on the R(1/2,1/2,1/2) point instead of Γ(0,0,0) point.

The supercell expansion flattened the band-structure (as shown in Fig. 2.12B, compared to ref.[241]), but all the other electronic structures remain the same. The band-gap still located on the R point of the Brillouin zone. The VBM is mostly consist of the chloride p-orbitals and the CBM is mostly consist of the lead *p*-orbitals (as shown in Fig. 2.12A, C, and D). As expected, standard DFT underestimates the bandgap in the $CsPbCl_3$ material substantially. [16] The calculation gives a band gap of 2.2 eV (3.1 eV as measured and shown in Fig. 2.10), which is consistent with previous calculations. [241, 172] The spin-orbit coupling is not considered in the paper due to tremendous computational cost. According to the literatures, the higher level of calculations, *e.g.*, including spin-orbit coupling, using GW method or hybrid functionals can give accurate band-gaps, but would not virtually alter the band-structures. [16]

By modifying the supercell structure, we can get the various types of the M^{3+}-doped $CsPbCl_3$ defects. All types of defects (linear, diagonal, A1 and A2 type) studied in this paper has been summarized in Fig. 2.13, with defect densities of 0.4×10^{20} cm^{-3}. The geometries of the defects are further relaxed with a total energy convergence of 10^{-4} eV.

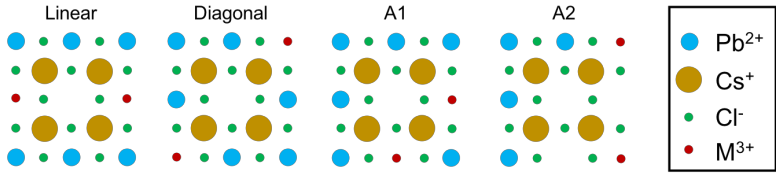

Figure 2.13: Four types of M^{3+}-V_{Pb}-M^{3+} defects.

The formation energy of a defect with charge q can be calculated as [2]

$$\Delta H_f(\alpha, q) = E^d(\alpha, q) - E^h + \sum_i n_i(\mu_i + E_i) + q(\epsilon^h_{VBM} + \epsilon_F) \tag{2.3}$$

Where, $E^d(\alpha, q)$ is the total energy of the defect supercell, E^h is the total energy of the non-defect supercell. μ_i is the chemical potential of the constituent i referenced to the total energy E_i of its pure elemental solid or molecule (Cs metal, Pb metal, and Cl_2 molecule for $CsPbCl_3$). n_i is the number of atom i, and q is the number of electrons, transferred from the supercell to the reservoirs in forming the defect cell. In the case of a M^{3+}-V_{Pb}-M^{3+} defect, n_M = -2 and n_{Pb} = 3. q is the overall charge of the defect. ϵ^h_{VBM} is the energy of the VBM. ϵ_F is the Fermi level. Usually, the defect transition energy level can be calculated assuming the charged defect has the same formation energy as the non-charged defect.

$$\Delta H_f(\alpha, q) = \Delta H_f(\alpha, q') \tag{2.4}$$

Substituting Eq. (2.3) into Eq. (2.4) will give the transition energy level $\epsilon(q/q')$ as:

$$\epsilon(q/q') = \frac{E(\alpha, q) - E(\alpha, q')}{q' - q} - \epsilon^h_{\mathrm{VBM}} \tag{2.5}$$

The value of formation energy showed in Eq. (2.3) largely depends on the constituent chemical potential μ_i, which is bounded by:

$$\Delta H_{f\,\mathrm{PbCl_2}}^{\mathrm{bulk}} \leq \mu_{\mathrm{Pb}} \leq \mu_{\mathrm{Pb}}^{\mathrm{bulk}} \tag{2.6}$$

$$\Delta H_{f\,\mathrm{MCl_3}}^{\mathrm{bulk}} \leq \mu_{\mathrm{M}} \leq \mu_{\mathrm{M}}^{\mathrm{bulk}} \tag{2.7}$$

The lower bound of Eq. (2.6) and Eq. (2.7) represents for the metal-poor growth condition, on the other hand, the upper bound stands for the metal-rich growth condition. In the paper, we assumed a Pb-rich synthetic condition as suggested by the experiments. We calculate the formation energy range of M^{3+}-V_{Pb}-M^{3+} by altering the dopant M^{3+} growth condition.

As shown in Fig. 2.14, Al^{3+}-defects have much higher formation energy even in the Al^{3+} rich growth condition. This is because the Al^{3+} ions are too small (70pm) to be commensurate to the V_{Pb} (133pm) in the lattice, which leads to a severe lattice distortion. Therefore, the Al^{3+}-defects are much less stable comparing to the other M^{3+}-defects, which are all over 100 pm in ionic radii. The formation energy explains the synthetic difficulty of making the Al^{3+}-doped $CsPbCl_3$. For the Y^{3+}/La^{3+}/Yb^{3+}/Lu^{3+}-defects, the linear and A1 type defects always have lower formation energies in the M^{3+} rich growth condition; while the A2 type defects always have the highest formation energies in the M^{3+} rich growth condition. This means the stability roughly follows the trend of: linear $\approx$ A1 $>$ diagonal $>$ A2 in all four M^{3+} dopants. The energy differences between the linear type and A1 type defects are subtle, indicating the high possibility of their co-existence in the lattice.

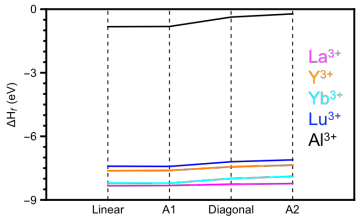

Figure 2.14: The formation energies of linear, diagonal, A1, and A2 types of M^{3+}-defect. The formation energy ranges are calculated by setting a Pb and M rich condition, *i.e.*, $\mu_{Pb} = \mu_{\mathrm{Pb}}^{\mathrm{bulk}} = 0$, and $\mu_M = \mu_{\mathrm{M}}^{\mathrm{bulk}} = 0$.

A main reason to account for the defect stability is the electrostatics. The total energy change after introducing the defect can be attributed to two coulomb interactions, the V_{Pb}(-2q)-M^{3+}(+q) attraction and M^{3+}(+q)-M^{3+}(+q) repulsion. The linear and A1 defects maximize the V_{Pb}-M^{3+} attraction, while the M^{3+}-M^{3+} distance is well separated in the linear defect to minimize the repulsion. The detailed electrostatic analysis can be found in Fig. 2.15. The analysis suggests the linear defect should be slightly more stable than the A1 defect, however, due to the strain effects in the actual lattice, there are some cases the formation energy of A1 defects can be slightly lower than the linear defects, e.g. Lu^{3+} and Yb^{3+}-doped ones.

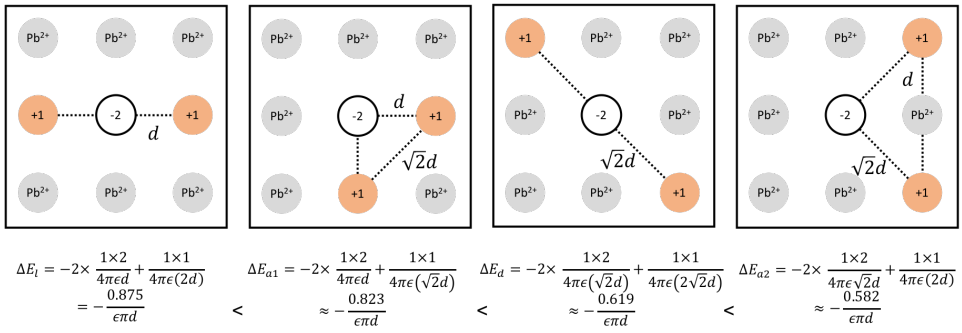

Figure 2.15: The electrostatic explanation of the defect stability. From a pure electrostatic point of view, the stability trend is: linear > A1 > diagonal > A2, which is consistent with the first principle calculations.

Figure 2.16 shows the defect energy levels of four types of M^{3+}-defects and Figure 2.17 shows the defect Bohr radius in the linear type defects. Similar size-dependencies can be observed in both figures, *i.e.*, the smaller M^{3+} ions will lead to a deeper trap (with respect to the CBM) with smaller defect Bohr radius.

We hypothesize that the lattice commensuration is the key factor governing this size-dependency. The worse lattice commensuration of the small M^{3+} ions will cause severer structural distortion: the Cl atoms will be contracted to the M^{3+} to form the M-Cl bond, in consequence, the adjacent Cl-Pb distance will be elongated, which impairs the bonding

between the defect center and the rest of the lattice, leading to a more locally trapped defect. On the other hand, in the defect of large M^{3+} dopants, since their ionic radii are much similar to the Pb^{2+}, the M-Cl and Cl-Pb bond distances are much more balanced, leading to a delocalized defect (relative large Bohr radius). On the analogy of the "particle in a box" model, the more localized wave function corresponds to the lower energy state. Therefore, within the same type of defect, smaller M^{3+} dopant will lead to a deeper defect energy level.

In terms of the different types of defects, the linear and A1 type defects have similar defect energy levels (except Al^{3+} doped) and are deepest among the four, while the A2 type M^{3+}-defects have the shallowest defect energy levels. The observation is consistent with the results of formation energies. A stable defect (with more negative formation energy) will have a lower defect energy level, in other word, will create a deeper energy trap.

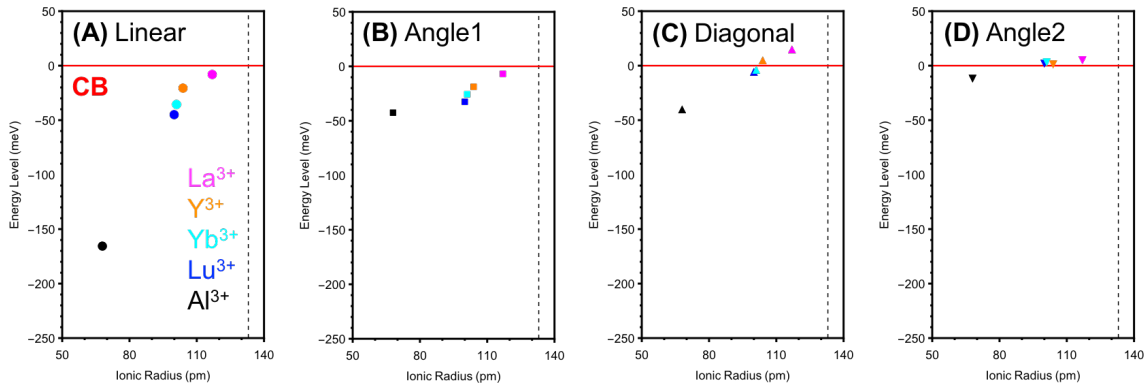

Figure 2.16: The defect transition energy levels of Al^{3+}, Lu^{3+}, Yb^{3+}, Y^{3+} and La^{3+}-doped $CsPbCl_3$. The black line indicates the ionic radius of Pb^{2+}, the red solid horizontal line indicates the CBM. The linear defects introduce the deepest defects while the A2 defects introduce the shallowest defects. However, all defects follow a size-dependency of the dopant ionic radii.

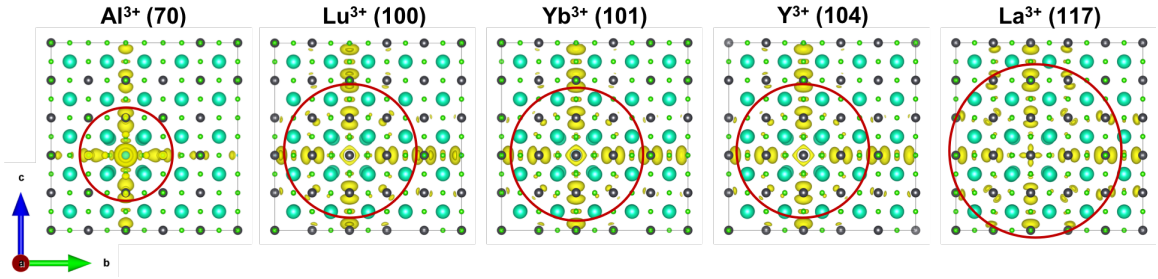

Figure 2.17: The wave functions of charged defects in linear type M^{3+}+-doped $CsPbCl_3$, the wave functions are plotted at the same isovalue of 0.0002. The two M^{3+} are aligned along a-axis in linear type and are diagonally across the a-c plane in A1 type. In both defect types, the wave functions expand as the size of M^{3+} dopants increase. The red circles indicate the rough estimation of defect Bohr radii, which are 0.57 nm, 0.86 nm, 0.86 nm, 0.86nm, 1.28nm, respectively.

Though both the calculations and experiments reveal a same size-dependent trend on the defect energy levels. The calculations under estimate the defect Bohr radii and overestimate of the defect energy levels (equivalent to underestimate the binding energy).

The calculated defect Bohr radii using experimental measured binding energies ranged from 1.1 nm for Lu^{3+} to 1.56 nm for La^{3+} as shown by Tab. 2.1. We can roughly estimate the defect Bohr radius of linear type M^{3+}-defects from 0.6 nm for Al^{3+} to 1.2 nm for La^{3+} based on Fig. 2.17. The underestimation is because the 5×5×5 supercell is not large enough to show a clear termination of the defect wave function within the lattice boundary.

The overestimation of the defect energy levels is mainly contributed by the overestimation of the total energy of one-electron charged defect $E(\alpha, -1)$ used in Eq. (2.5). Due to the computational cost, we used a 5×5×5 supercell, such size may be sufficient enough to prevent the simple replacement or vacancy or interstitial defect from interacting with its adjacent charged defect cell, but not for the large defects like M^{3+}-V_{Pb}-M^{3+}. Therefore, the $E(\alpha, -1)$ used in Eq. (2.5) also accounts for the repulsion from the adjacent charged defect cell. Therefore, the defect binding energy is systematically overestimated for all defect types and M^{3+} dopant. Overall, a larger supercell size might remedy both issues, but far more

computation resources will be required. Nevertheless, the current supercell modeling is adequate to provide qualitative agreement with experiments and insights for designing the M^{3+}-doped $CsPbCl_3$.

2.2.4 Conclusion

In summary, we have combined both experimental and computational approaches to study the electronic structures of various M^{3+}-$CsPbCl_3$ defects. Through the calculations, we found that among different types of defects we proposed, the linear defect is the most stable one for all examined M^{3+}. However, under the same Pb^{2+}-rich and M^{3+}-rich growth condition, its energy difference with the A1 type M^{3+}-VPb-M^{3+} defect is subtle, those two types of defects are likely to co-existence in the realistic experiment conditions. In the same type of defect, both experiments and calculations confirm that the energy level and Bohr radius of the defect show a size-dependency with respect to the size of doped M^{3+} ions. We propose the lattice commensuration plays important role in the size-dependent trend of defect energy levels, i.e., too small M^{3+} dopant cannot balance the M-Cl and Pb-Cl bond distances, leading to strong M-Cl and weak Pb-Cl bonds, which make the wave function localize to the close proximity of the M^{3+} center, giving rise to a deep trap and small defect Bohr radius. The calculations and experiments again support the quantum-cutting mechanism in the Yb^{3+}-doped $CsPbCl_3$ and give insights into the further modification of the $CsPbCl_3$ as more promising down-conversion materials.

Chapter 3

MODELING NANOMATERIALS WITH HYBRID QUANTUM-CLASSICAL METHOD.

In Chapter 2, we focused on the ab initio simulations of bulk materials with the help of periodic boundary conditions. However, when condense matter solid shrink its size to several nanometer scale, which ususally means that the size of the material is already smaller than its exciton Bohr radius, quantum confinement effect is going to introduce many peculiar properties to the materials. At this time, the periodic boundary condition is no longer a good approximation to simplify the wave function expansion. Nanocrystal with the size of 5 nm in radius usually contains more than tens or hundreds thousand of atoms, leading to tremendous amount of atomic basis functions. Modeling those nanomaterials in the atomic basis is neither a feasible approach. To keep nanocrystal in a tractable size, we need to introduce more elegant approximation to simplify the degree of freedom in the Schrödinger equation. Quantum dot is a kind of nanomaterials which has been shown success in modeling in a mathematical model. The hybrid quantum-classical model shows excellent agreement with experimental and DFT calculated results in Fermi-levels. The simple mathematical formalism also allows the further extension of the model. The model can be applied not only to even aliovalently doped quantum dots to reveal novel physical phenomena. This chapter is adapter with permission from Hongbin Liu, Carl K Brozek, Shichao Sun, David B Lingerfelt, Daniel R Gamelin, Xiaosong Li, *J. Chem. Phys. C* **2017**, *121*, 26086-26095. [187]

3.1 Introduction

Addition of excess charge carriers has emerged as a powerful tool for manipulating the physical and chemical properties of colloidal quantum dots (QDs). Multiple conduction-band (CB) electrons can be introduced synthetically through aliovalent doping, or through electrochemical, thermochemical (remote chemical doping), or photochemical reduction (photodoping).[267] Charge mobilities, carrier dynamics, optical absorption, plasmon resonances, and various physical properties are altered upon charge accumulation. In certain materials, infrared plasmonics emerge that are tunable by charge, size, and composition,[152, 51, 269] giving rise to fascinating electrochromic[96], and magneto-optical behavior.[107] Electrostatic interactions between additional carriers and surface charges leads to dramatic shifts in band-edge potentials [41] and Stark-shifted luminescence. [315] At a fundamental level, many properties of excess electrons in charged QDs are not well understood, however. Despite progress in tuning carrier densities in various colloidal QD materials, such as ZnO, CdSe, PbS, InN, and In_2O_3, [266, 257, 145, 194, 268] the factors governing CB electron (e^-_{CB}) potentials and maximum achievable carrier densities remain largely unknown.

Mounting experimental evidence points to surface electrostatics as key determinants of QD band-edge potentials. Systematic modulation of PbS, HgS, and CdSe surface dipoles has been shown to tune their band-edge potentials by hundreds of mV.[41, 29, 47] Similar energetic shifts are observed by altering the ion-pairing strength of charged ZnO[40, 30] QDs with charge-balancing cations of differing coordinating ability. Confinement and inter-electronic interactions alone cannot account for these experimental observations. A convenient model is needed to describe excess electrons in charged QDs that accounts for electron-cation stabilization, dielectric effects, and inter-electronic interactions. To the best of our knowledge, no such model exists.

The "Particle in a Sphere" model [32, 33] is widely used to describe singly occupied QDs. Expressed in spherical coordinates, it solves the Schrödinger equation, $\hat{H}\Psi(r,\theta,\phi) = E\Psi(r,\theta,\phi)$. After the separation of variables, the Hamiltonian in the radial equation is

composed of kinetic, angular, and potential terms, written in atomic units as:

$$\hat{H} = -\frac{1}{2}\frac{d^2}{dr^2} + \frac{l(l+1)}{2r^2} + V(r) \tag{3.1}$$

The potential $V(r)$ in the Hamiltonian is usually defined as a step function:

$$V(r) = \begin{cases} -E_A, & r < R \\ 0, & r \geq R \end{cases} \tag{3.2}$$

where E_A is the electron affinity and R is the radius of the QD. With the definition of $V(r)$ in Eq. (3.2), solution of the single-electron Schrödinger equation is analytically tractable, with wavefunctions and energy levels taking the form:

$$\Psi(r, \theta, \phi) = A \cdot \mathcal{R}_{nl}(r) \cdot Y_l^m(\theta, \phi) \tag{3.3}$$

$$E_{nl} = \frac{\beta_{nl}^2}{2R^2} \tag{3.4}$$

where $\mathcal{R}_{nl}(r)$ is the spherical Neumann function, $Y_l^m(\theta, \phi)$ is the spherical harmonic function, and A is a normalization constant. β_{nl} is the solution to the boundary condition of the spherical Neumann function. This approach gives rise to hydrogenic orbitals, which have been reproduced using density functional theory (DFT) calculations of QD e_{CB}^-.[101]

Whereas the square well potential assumed in Eq. (3.2) is sufficient for singly occupied QDs in the absence of surface chemistry, it does not describe inter-electronic interactions of many-electron systems, nor does it account for important experimental parameters such as charge compensation or the solvent dielectric strength. As electrons populate the CB, inter-electronic and electron-countercation interactions significantly perturb the effective potential acting upon a e_{CB}^-. In first-principles methods, inter-electronic interactions produce Coulomb and exchange contributions to the Fermi-level energy (E_F), but such calculations are only tractable for small clusters of atoms.[300, 101, 224, 97, 219, 49] Here, we present a model of inter-electronic and electron-cation interactions in multiply charged QDs that, through comparison with ab initio calculations and experimental results, accurately approximates

E_F of charged QDs. By treating key experimental parameters as explicit variables in the model, their impact on the energetics of excess electrons can be investigated systematically for any QD material. We then illustrate how this versatile model can help explain emerging phenomena in multiply charged QDs.

3.2 Hybrid Quantum-Classical Model

3.2.1 Theoretical Model

The model presented here approximates inter-electronic and electron-cation interactions by modifying the potential term of Eq. (5.5) to reflect a uniformly charged sphere. To distinguish our model from the "Particle in a Sphere" model with a square well potential, we term these the "Charged Sphere" and "Square Well" models, respectively. The "Charged Sphere" model consists of q^- number of electrons inside a spherical QD of radius R with q^+ compensating cations at the QD surface (Fig. 3.1). Employing Gauss's law, the effective potential outside the QD ($r \geq R$) arises from contributions from both q^+ and q^-,

$$V^+(r) = -\frac{q^+}{\epsilon_{\text{out}} r}, \quad r \geq R; \quad V^-(r) = +\frac{q^-}{\epsilon_{\text{out}} r}, \quad r \geq R \tag{3.5}$$

where ϵ_{out} is the dielectric constant of the medium (solvent or vacuum) surrounding the QD. In Eq. (3.5)–Eq. (3.10), $V_{r=\infty}$ determines the zero reference.

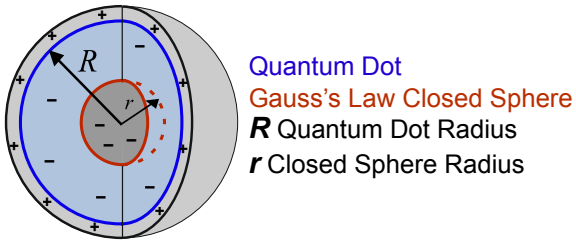

Figure 3.1: Pictorial representation of the "Charged Sphere" model.

q^+ and q^- make different contributions to the potential inside the QD ($r < R$). Because q^+ is distributed evenly across the QD surface, its contribution is equal everywhere inside

the dot, and can be written as

$$V^{+}(r) = -\frac{q^{+}}{\epsilon_{\text{out}} R}, \quad r < R \tag{3.6}$$

The contribution of the electric field generated by q^{-} to the potential inside the QD ($r < R$) can be evaluated at any distance r using Gauss's Law (Fig. 3.1) as,

$$E(r) = \frac{\iiint \rho(r) dV}{r^2 \epsilon_r}, \quad r < R \tag{3.7}$$

where ϵ_r and $\rho(r)$ are the dielectric constant and electron density inside the QD. As a starting point, the electron density and dielectric constant are uniform inside the QD, so that Eq. (3.7) can be rewritten as

$$E(r) = -\frac{q^{-} r}{\epsilon_R R^3} \tag{3.8}$$

where $\rho(r)$ is replaced by the homogenous e^{-}_{CB} density (ρ^{-}_{CB}) inside the QD, $\rho^{-}_{CB} = \frac{q^{-}}{(\frac{4}{3}\pi R^3)}$, and the dielectric constant ϵ_r becomes the dielectric constant of the QD, ϵ_R. Integrating Eq. (3.8) from r to ∞ leads to the following expression for the potential inside the QD:

$$V^{-}(r) = -\frac{q^{-} r^2}{2\epsilon_R R^3} + \frac{q^{-}}{2\epsilon_R R} + \frac{q^{-}}{\epsilon_{out} R}, \quad r < R \tag{3.9}$$

Combining Eq. (3.2), Eq. (3.5), Eq. (3.6), and Eq. (3.9), the potential at any distance r can be expressed as

$$V(r) = \begin{cases} -\frac{1}{2\epsilon_R}[q^{-} r^2/R^3 - q^{-}/R] - \frac{1}{\epsilon_{out}}[(q^{+} - q^{-})/R + E_A] & r < R \\ \\ -\frac{1}{\epsilon_{out}}[(q^{+} - q^{-})/r] & r \geq R \end{cases} \tag{3.10}$$

Figure 3.2 depicts the combined effect of the square well potential, a quantum mechanical property defined as E_A/ϵ_{out}, and the electrostatic contributions from q^{+} and q^{-} to the total effective potential, $V(r)$. Varying q^{-} and q^{+} in Eq. (3.10) leads to potentials with drastically different forms, as shown in Fig. 3.2. Two scenarios are presented, $q^{+} > 0$ and $q^{+} = 0$, to illustrate the competing effects of $q^{-}/\epsilon_{out} R$ and $q^{+}/\epsilon_{out} R$ on the potential. Unless specified

otherwise, discussion of the "Charged Sphere" model will refer to the scenario when $q^+ = q^-$. Below, this model is contrasted with the "Anionic Charged Sphere" ($q^+ = 0$) and the "Square Well" models to explore the impact of electron-cation and inter-electronic interactions.

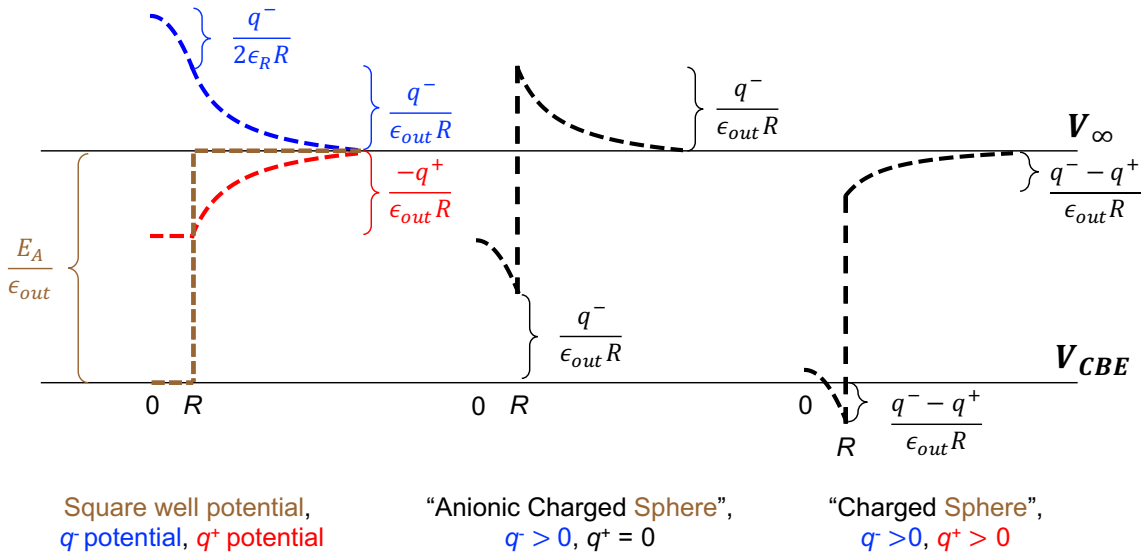

Figure 3.2: Illustration of the energetic contributions of the square well potential (brown), q^+ (red), and q^- (blue) to the total potential (black), with two specific scenarios highlighted: $q^- \neq 0, q^+ = 0$ (middle, "Anionic Charged Sphere" model) and $q^+ > 0, q^- > 0$ (right, "Charged Sphere" model). V_∞ and V_{CBE} denote the potential at $r = \infty$ and at the CB edge (CBE) of the undoped QD, respectively.

Equation (3.10) suggests that for a given charged semiconductor QD surrounded by a dielectric medium (e.g., solvent), the potential depends on three tunable parameters: the size of the quantum dot (R), the excess electron density inside the QD ($\rho^-_{CB} \propto q^-$), and the density of surface counter cations ($\rho^+_{SUR} \propto q^+$). In the limit of large crystal radius ($R \to \infty$), it is easy to see from Eq. (3.10) that the potential inside the crystal approaches zero. On the other hand, in the limit of low ρ^-_{CB} ($q^- = 0$) and no surface counter ions ($q^+ = 0$), the potential in Eq. (3.10) simply converges to the results from the "Square Well" model.

For QDs with multiple e^-_{CB}, the QD radius R strongly affects the shape of the potential

inside the QD. Figure 3.3A plots $V(r)$ as a function of R for a ZnO QD solvated by tetrahydrofuran (THF) with $q^- = q^+ = 10$. Because evaluating $V(r)$ of undoped ZnO ($q^- = q^+ = 0$) requires an additional uncompensated probe electron, the same procedure was used to plot Fig. 3.3. To compare against undoped ZnO, therefore, the zero reference was taken as the CB edge (CBE) of undoped ZnO. ZnO and THF are represented in the "Charged Sphere" model by choosing $E_A = 4.2$ eV and $\epsilon_{out} = 7.56$, respectively. When R is small, the prominent r^2 dependence of the potential inside the QD is consistent with classical Coulombic repulsion increasing for charges confined to a small volume. As the QD size increases, the potential inside the QD flattens because the Coulombic repulsion is spread across a larger volume. The bulk limit is illustrated with a $R = 5\mu m$ sphere, where the charged sphere model yields the same results as the"Square Well" model. The exterior potential in Fig. 3.3A follows a similar size dependence. Charges confined to smaller QDs destabilize the exterior potential more than when R is large, in which case the exterior potential approaches a bulk limit dominated by E_A and ϵ_{out}. At the boundary ($r = R$), the potential is zero because the contributions from both q^- and q^+ cancel exactly ($q^- = q^+$ for all examples shown in Fig. 3.3A).

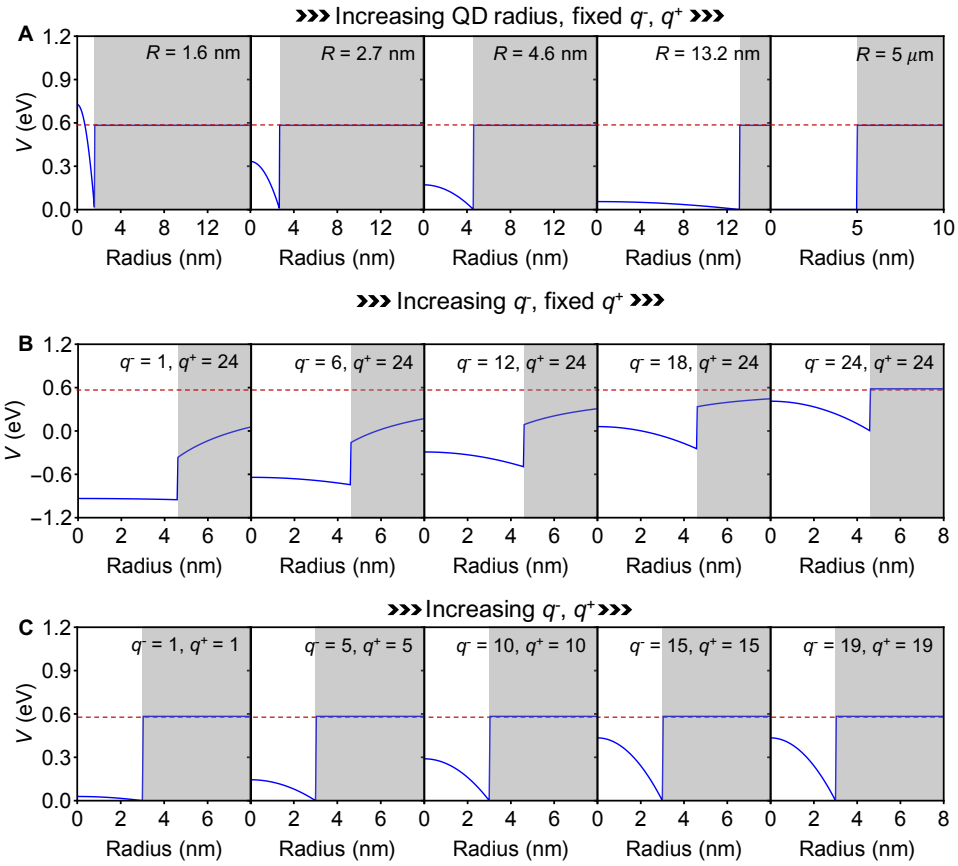

Figure 3.3: **A:** Size-dependence of the potential for a multiply charged ZnO QD with a fixed number of electrons solvated by THF ($q^- = q^+ = 10$). See Eq. (3.10) for the definition of $V(r)$. **B:** Electron density-dependence of the potential for a $R = 4.6$ nm ZnO QD solvated by THF with fixed $q^+ = 24$. **C:** Dependence of the potential on increasing numbers of q^+, q^- pairs in a $R = 3$ nm ZnO QD solvated by THF. ZnO and THF are simulated with $E_A = 4.2$ eV, $\epsilon_{out} = 7.56$. $r > R$ regions are shaded in grey. The horizontal red dashed line denotes the exterior potential bulk limit, E_A/ϵ_{out}. The zero reference is set at the V_{CBE} of pure undoped ZnO for all cases, i.e. $q^- = q^+ = 0$.

Figure 3.3B illustrates the effect of $\rho^-_{CB} \propto q^-$ on $V(r)$ when q^+ is fixed. Both E_A and ϵ_{out} are chosen again to simulate a ZnO QD solvated by THF. As the density increases, the interior potential rises, being highest at the origin and decreasing quadratically towards the surface. This behavior arises from inter-electronic repulsion within the classical mean-

field approximation. Figure 3.3B also illustrates that in accordance with Eq. (3.10) charge balancing cations ($q^+ : q^- > 1$) lower both the interior and exterior potentials. This scenario is also depicted in the "Charged Sphere" model of Figure 3.2 and represents an extreme limit of charged QDs with large electrical double layers due to low electrolyte concentrations.

Figure 3.3C depicts the scenario where overall charge neutrality is maintained at the surface of a $R = 3$ nm ZnO QD solvated by THF. For different values of $q^+ = q^-$, the exterior potential remains constant, whereas the interior potential rises sharply with electron accumulation. The maximum number of e^-_{CB} (q^-_{max}) that can be stabilized in a QD is given by the value where E_F equals the exterior potential energy. Because $q^- = q^+$, the potential again equals zero at the QD surface, where both contributions cancel exactly.

The results presented above illustrate the impact of QD size and charge density on the energetics of excess CB electrons in QDs. As seen from Fig. 3.3A–C, in the case of weak inter-electronic repulsion or bulk-like crystal sizes, the "Square Well" model is sufficient, but this model fails when multiple excess electrons are confined to small volumes, which is the scenario of most interest when studying charged QDs.

3.2.2 Implementation of the "Charged Sphere" Model

Whereas analytical solutions of the Schrödinger equation using the "Square Well" model (Eq. (3.2)) can be obtained (Eq. (3.3) and Eq. (3.4)), the Schrödinger equation using the "Charged Sphere" model (Eq. (3.10)) does not have analytical solutions. Instead, the discrete variable representation (DVR) approach[49, 179] is used to numerically solve the Schrödinger equation for e^-_{CB}, with the potential as defined in Eq. (3.10). To compare Eq. (3.5)–Eq. (3.10) and Fig. 3.3 against undoped ZnO ($q^- = q^+ = 0$), an additional uncompensated probe electron was used to evaluate $V(r)$. As a result, the potential at $r = R$ equals zero because the interactions of q^- and q^+ with the probe electron are equal and opposite. This potential is identical to the CB edge (V_{CBE}) of undoped ZnO ($q^- = q^+ = 0$) and is therefore the zero reference in Fig. 3.3. All other calculations with the "Charged Sphere" model treat the nth electron as a probe of the mean field created by the previous $n-1$ electrons so that the

minimum potential, always at $r = R$, lies $-1/\epsilon_{out}R$ lower than the V_{CBE} of the corresponding undoped ZnO QD due to stabilization by q^+, in accordance with Eq. (3.10) and as depicted by Fig. 3.2. Consequently, the zero reference for these calculations, and in Fig. 3.4, Fig. 3.7, Fig. 3.8, and Fig. 3.9, is taken as the minimum value for convenience. The zero reference of Fig. 3.5 is taken as the minimum of the "Charged Sphere" model, which lies $q^-/\epsilon_{out}R$ below the minimum of the "Anionic Charged Sphere" model. As stated previously, we solve the radial part of the Schrödinger equation for a given angular momentum. The size dependent dielectric constant formalism, [274]

$$\epsilon_R = 1 + \frac{\epsilon_0 - 1}{1 + \frac{1.8}{R^{1.7}}} \tag{3.11}$$

is used throughout the paper, where ϵ_0 is the static dielectric constant.

3.2.3 Comparison to the "Square Well" Model

Figure 3.4 compares the potential energies of the Fermi-level electron (V_F) and radial-distribution functions ($\psi(r)^2r^2$) calculated from both the "Charged Sphere" and "Square Well" models for different R and ρ_{CB}^-. Both models incorporate the centrifugal potential $\frac{l(l+1)}{2r^2}$ arising from orbital angular momentum. At low ρ_{CB}^-, the solutions of the two models are nearly identical for all sizes. As ρ_{CB}^- increases at a fixed QD size, however, the solutions of the "Square Well" and the "Charged Sphere" models begin to deviate. Both models predict a shift of the radial-distribution function toward the surface at higher angular momentum due to the centrifugal potential. This shift causes a large degree of e_{CB}^- tunneling ("spill out"). Compared with the "Square Well" solutions, the e_{CB}^- in the "Charged Sphere" model shift more toward the QD surface because of inter-electronic repulsion, resulting in a narrower distribution (Figure 3.4). For example, in the case of $q^- = q^+ = 32$ in a $R = 4.0$ nm QD, the difference between the positions of the distribution maxima is as large as 0.41 nm, with a full-width-at-half-maximum (FWHM) difference of 0.43 nm. The righthand side of Fig. 3.4 shows that for a fixed electron density, this deviation is accentuated with increasing R. For example, when $\rho_{CB}^- = 1.4 \times 10^{20}$ cm^{-3} in a $R = 4.0$ nm QD, the sum total $\psi(r)^2r^2$ of all e_{CB}^-

$(\Sigma\psi(r)^2r^2)$ from the "Square Well" model resides at $r = 3.17$ nm with a 1.35 nm FWHM, whereas the "Charged Sphere" model predicts a maximum at $r = 3.58$ nm with a 0.99 nm FWHM. At this ρ^-_{CB} and $R = 2.0$ nm, the "Square Well" and the "Charged Sphere" models produce nearly identical results.

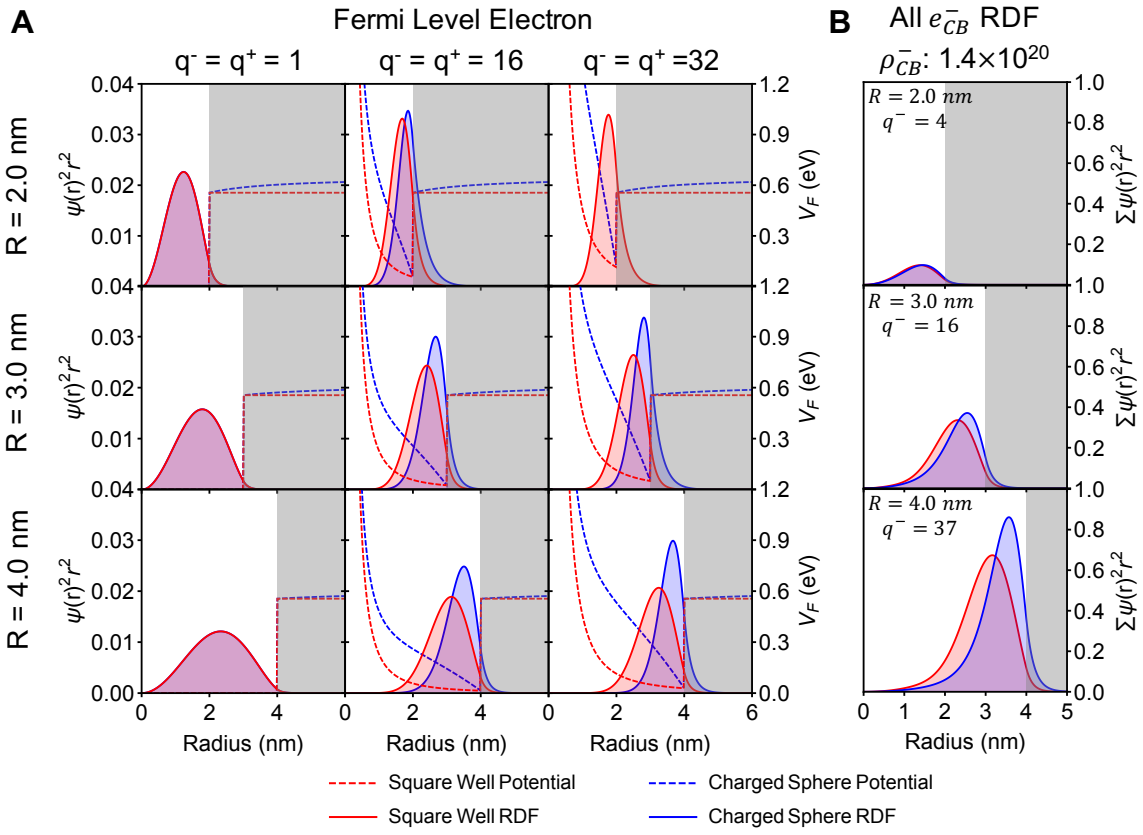

Figure 3.4: Comparison of the "Square Well" (red) and "Charged Sphere" (blue) models for a ZnO QD solvated by THF ($E_A = 4.2$ eV, $\epsilon_{out} = 7.56$). The zero reference is set to the potential energy minimum for each QD size. **A**: Dependence of the potential energy of the Fermi-level electron (V_F) and radial-distribution functions ($\psi(r)^2r^2$) of the QD Fermi-level electron on the QD radius (R) and number of q^-, q^+ pairs. Potentials are plotted as dashed lines and $\psi(r)^2r^2$ as shaded curves. **B**: Dependence of the sum total $\psi(r)^2r^2$ of all e^-_{CB} $(\Sigma\psi(r)^2r^2)$ on R at a fixed ρ^-_{CB}.

3.2.4 Comparison to the "Anionic Charged Sphere" Model

To evaluate the energetic stabilization provided by charge-balancing cations, we compare V_F in the "Anionic Charged Sphere" and "Charged Sphere" models. From Fig. 3.2, the interior potential in the "Anionic Charged Sphere" model raises by $q^-/\epsilon_{out}R$ above V_{CBE}, where q^- is the number of uncompensated e^-_{CB}, consequently also shifting the E_F by $q^-/\epsilon_{out}R$. This Coulombic term suggests charge-balancing cations provide greatest stabilization for highly charged QDs with small R and ϵ_{out}.

Figure 3.5 compares V_F and $\psi(r)^2r^2$ calculated from the "Charged Sphere" ($q^+ = q^-$, blue) and "Anionic Charged Sphere" ($q^+ = 0$, black) models for a $R = 4$ nm ZnO QD solvated by THF ($E_A = 4.2$ eV, $\epsilon_{out} = 7.56$) for several values of q^-. The lefthand figure shows that $\psi(r)^2r^2$ (shaded curves) calculated from both models are nearly identical when $q^- < 16$. The calculated potentials (dashed lines) on the other hand deviate even at $q^- = 1$, with the "Anionic Charged Sphere" model predicting higher E_F. At $q^- = 16$, the interior potential rises above the exterior potential, causing the maximum of $\psi(r)^2r^2$ to lie outside the QD. In other words, QDs with uncompensated e^-_{CB} support lower electron densities. The righthand panel of Fig. 3.5 summarizes this result across QD sizes, showing again that modeling charged QDs without surface cations ($q^+ = 0$) systematically underestimates q^-_{max}.

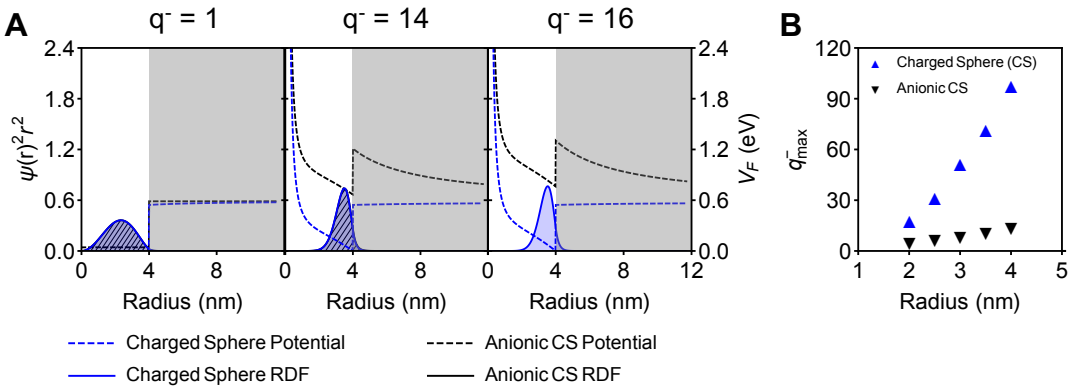

Figure 3.5: Comparison of the "Charged Sphere" (blue) and "Anionic Charged Sphere" (black) models for a $R = 4$ nm ZnO QD solvated by THF ($E_A = 4.2$ eV, $\epsilon_{out} = 7.56$). **A**: Dependence of V_F and $\psi(r)^2r^2$ of the QD Fermi-level electron on the QD radius, R, and number of q^-, q^+ pairs. Potentials are plotted as dashed lines and $\psi(r)^2r^2$ as shaded curves (hashed black for the "Anionic Charged Sphere" model). V_F of the "Anionic Charged Sphere" model are baseline-corrected so that the zero reference is taken as the minimum potential of the "Charged Sphere" model. **B**: Size-dependence of q^-_{max}.

3.2.5 Comparison to DFT and Experiment

To evaluate the accuracy of the "Charged Sphere" model, we compared its solutions to DFT calculations of small QDs. Details of the DFT calculations are provided in the Methods section. Figure 3.6 compares E_F from the "Charged Sphere", "Anionic Charged Sphere", and "Square Well" models with DFT calculations of $Zn_{33}O_{33}$ ($R = 0.6$ nm), $Zn_{84}O_{84}$ ($R = 0.7$ nm), and $Zn_{153}O_{153}$ ($R = 0.8$ nm) and experimental results[40, 266] of various ZnO QDs. Figure 3.6A plots the predicted energetic difference between the 1 e^-_{CB} and 2 e^-_{CB} Fermi levels (ΔE_F) of $R = 0.6$ nm, $R = 0.7$ nm, and $R = 0.8$ nm ZnO QDs in vacuum ($\epsilon_0 = 1$). The "Square Well" model predicts degeneracy of these levels ($\Delta E_F = 0$), whereas the "Charged Sphere" and "Anionic Charged Sphere" models and DFT calculate nonzero ΔE_F values that are numerically similar with average values of $\Delta E_F = 0.31$ eV, 0.25 eV, and 0.20 eV for the $R = 0.6$, 0.7, and 0.8 nm QDs, respectively.

For comparison against two key experimental signatures of multiply charged QDs, the

"Charged Spher" model was used to compute the size dependence of q^-_{max} and the impact of many additional charge carriers on E_F. Figure 3.6B compares q^-_{max} determined from the "Charged Sphere" model with experimental results of ZnO QDs photodoped in the presence of Li[$HBEt_3$] or K[$HBEt_3$].[266] Excellent numerical agreement between theory and experiment show increasing q^-_{max} for larger QD sizes. The strong size dependence of q^-_{max} observed experimentally for ZnO,[266] In_2O_3, Sn:In_2O_3,[268] and InN[194] QDs can therefore be interpreted in terms of the "Charged Sphere" model as large QDs requiring greater numbers of excess charges to reach the destabilizing interior effective potential that limits q^-_{max}. Figure 3.6C compares E_F values of THF-solvated $R = 3.7$ nm ZnO QDs from experiment and predicted by the "Square Well" and "Charged Sphere" models. For clarity, the zero reference in this figure is taken as E_F at $1e^-_{CB}$ ($E_F^{1e^-}$) rather than V_{CBE} because the "Charged Sphere" model predicts this value to lie nearly $\frac{1}{\epsilon_{out}R}$ below V_{CBE}, leading to an unphysical negative value. Note that we are unable to calculate the electronic structure of a $R = 3.7$ nm ZnO QD using DFT due to computational expense. The solutions to the "Square Well" model are a set of hydrogenic orbitals with degeneracy within each orbital shell ($S, P, D, \dots$). By excluding inter-electron repulsion, these orbitals fill in a staircase fashion with constant potential for each orbital shell. In contrast, the "Charged Sphere" model reproduces the more gradual increase in E_F observed in experiment [40] and expected for multi-electron systems when inter-electronic repulsion is included.

Figure 3.6D illustrates that the "Anionic Charged Sphere" model calculates E_F values that are systematically raised by $q^-/\epsilon_{out}R$ after applying the baseline correction described above. Even at low e^-_{CB} accumulation, a lack of charge compensation destabilizes E_F by hundreds of meV.

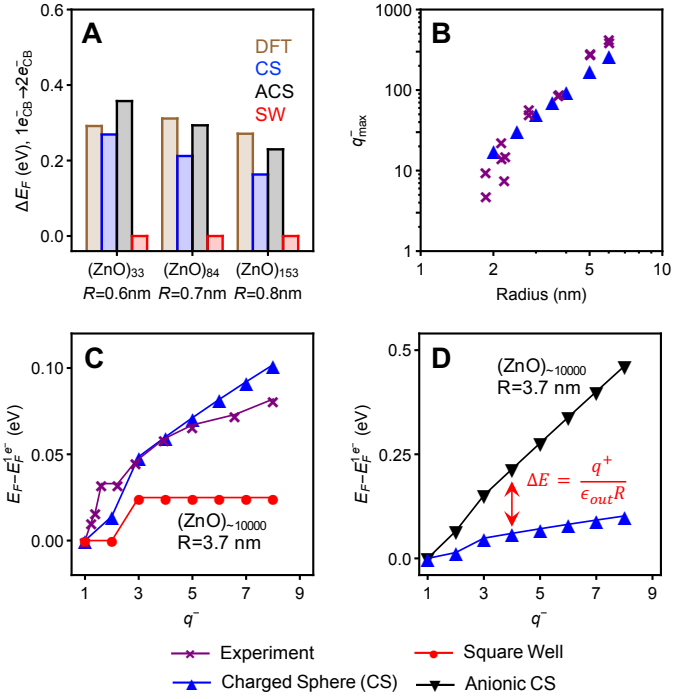

Figure 3.6: Comparison of ZnO QD Fermi-level energies (E_F) calculated using the "Square Well", "Charged Sphere", and "Anionic Charged Sphere" models ($E_A = 4.2$ eV, $\epsilon_{out} = 1$ (vacuum)) with DFT and experimental results.[40] **A:** Energetic difference (ΔE_F) between 1 e^-_{CB} and 2 e^-_{CB} Fermi levels of $R = 0.6$ nm, $R = 0.7$ nm, and $R = 0.8$ nm ZnO QDs calculated from the "Square Well", "Charged Sphere", and "Anionic Charged Sphere" models, and DFT. **B:** Comparison of the maximum number of e^-_{CB} (q^-_{max}) from experiments given in Ref. 8 and calculated by the "Charged Sphere" model. **C:** Comparison of calculated relative E_F values with experimental results for THF-solvated $R = 3.7$ nm ZnO QDs. Energies are plotted relative to the E_F at $1e^-_{CB}$ ($E_F^{1e^-}$). **D:** Comparison of E_F values calculated from the "Charged Sphere", and "Anionic Charged Sphere" models. The difference is equal to the term written in red. The baseline is corrected so that the zero reference is set at the minimum value calculated from the "Charged Sphere" model.

3.2.6 Comparison of Different QD Materials

Figure 3.7 compares $\Sigma\psi(r)^2 r^2$ and E_F for $R = 2$ nm In_2O_3 and ZnO QDs solvated by THF ($\epsilon_{\text{out}} = 7.56$), simulated using E_A values of 4.45 eV and 4.2 eV[215, 139] and ϵ_0 of 9 and 10, respectively. Two hypothetical materials were also included to illustrate the impact of

ϵ_0 by setting $\epsilon_0 = 20$ and $\epsilon_0 = 80$ but keeping the E_A of ZnO. For each material, ϵ_R was calculated from ϵ_0 using Eq. (3.11). Figure 3.7A compares the $\Sigma\psi(r)^2r^2$ of the QD materials at q^-_{max}, determined for all models as when the highest bound E_F is reached, i.e., when $E_F = E_A/\epsilon_{out}$. Figure 3.7B compares E_F computed from the "Square Well", "Charged Sphere", and "Anionic Charged Sphere" models versus number of e^-_{CB}. Horizontal lines indicate E_A/ϵ_{out} and vertical lines denote the q^-_{max} according to each color-coded model.

Figure 3.7 illustrates the impacts of ϵ_R and E_A in the "Charged Sphere" model on E_F, and hence q^-_{max}, of a QD material. As suggested by Eq. (3.9), a large ϵ_R screens the interior potential and inter-electronic repulsion. As a result, for similar values of E_A, higher dielectric materials accumulate more e^-_{CB} and exhibit diminished orbital energy splitting within a given orbital shell. A larger E_A, on the other hand, imposes a higher tunneling barrier, allowing more e^-_{CB} to accumulate. Therefore, despite In_2O_3 having ϵ_R smaller than ZnO, its larger E_A results in the two materials having similar q^-_{max}. As discussed above, the "Anionic Charged Sphere" model predicts Fermi-level energies that are greatly destabilized relative to the "Charged Sphere" results, and fewer e^-_{CB} accumulate in each material, resulting in the smallest q^-_{max} in Fig. 3.7A and $\Sigma\psi(r)^2r^2$ in Fig. 3.7B. The "Square Well" model, in contrast, predicts much higher q^-_{max} as a consequence of neglecting inter-electronic repulsion and fails to reproduce the constant increase in E_F with increasing values of q^-.

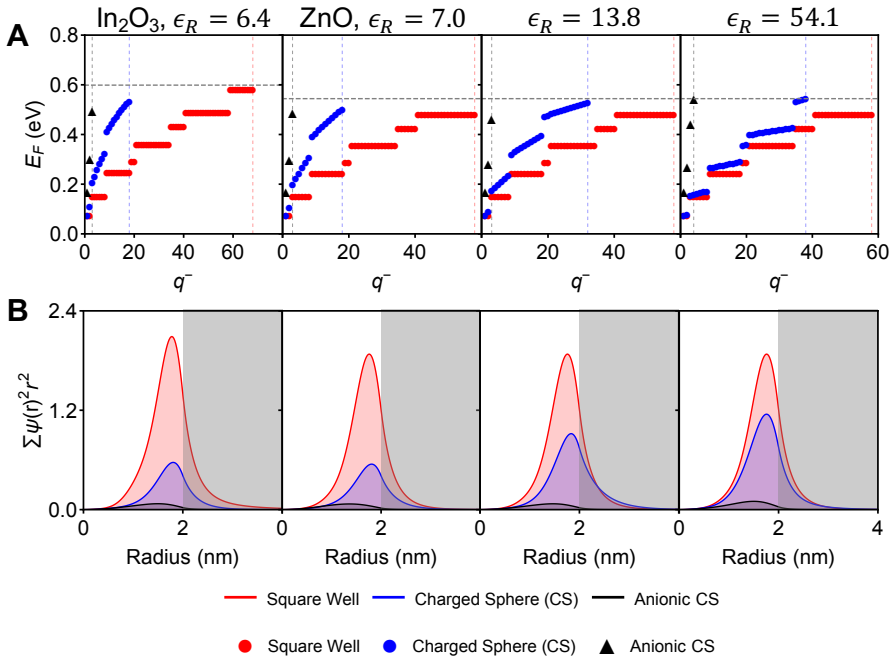

Figure 3.7: Comparison of E_F (**A**) and $\Sigma\psi(r)^2r^2$ (**B**) and of $R = 2$ nm ZnO, In_2O_3, and two hypothetical QDs using the "Square Well", "Charged Sphere", and "Anionic Charged Sphere" models. **A**: E_F of QDs with increasing e^-_{CB} accumulation. Horizontal lines indicate the E_A/ϵ_{out} of each material. Vertical lines denote q^-_{max} according to each color-coded model. **B**: Comparison of $\Sigma\psi(r)^2r^2$ of the same series of QDs at the predicted q^-_{max} of each. ϵ_R were calculated from Eq. (3.11), using ϵ_0 values of 9, 10, 20, 80 for In_2O_3, ZnO, and the two hypothetical materials, respectively.

3.2.7 Solvation Effects

Solvation effects can be simulated within the "Charged Sphere" model by adjusting ϵ_{out}. Figure 3.8 plots q^-_{max}, $\Sigma\psi(r)^2r^2$, and E_F for a $R = 2$ nm ZnO QD in various dielectric media chosen for their experimental relevance: toluene ($\epsilon_0 = 2.38$), polymethylmethacrylate (PMMA, $\epsilon_0 = 3$), THF ($\epsilon_0 = 7.56$), ethanol (EtOH, $\epsilon_0 = 24.5$), propylene carbonate (PC, $\epsilon_0 = 64$), water ($\epsilon_0 = 80.1$), and formamide ($\epsilon_0 = 111$). As suggested by Eq. (3.5), ϵ_{out} screens E_A, lowering the tunneling barrier and decreasing the q^-_{max}. The leftmost panel of Fig. 3.8 compares q^-_{max} as a function of ϵ_{out}. The smallest ϵ_{out} leads to greatest e^-_{CB} accumulation by

maximizing the barrier height E_A/ϵ_{out}. The middle panel of Fig. 3.8 illustrates the impact of ϵ_{out} on $\psi(r)^2r^2$ at a fixed q^-_{max}. In the 1-e^-_{CB} limit, the $\Sigma\psi(r)^2r^2$ expands toward the QD surface with increasing ϵ_{out}. The rightmost panel of Fig. 3.8 plots E_F for three selected solvents versus log of e^-_{CB}, illustrating that weaker dielectric solvents lower the interior QD potential, decrease E_F, and greatly confine $\psi(r)^2r^2$.

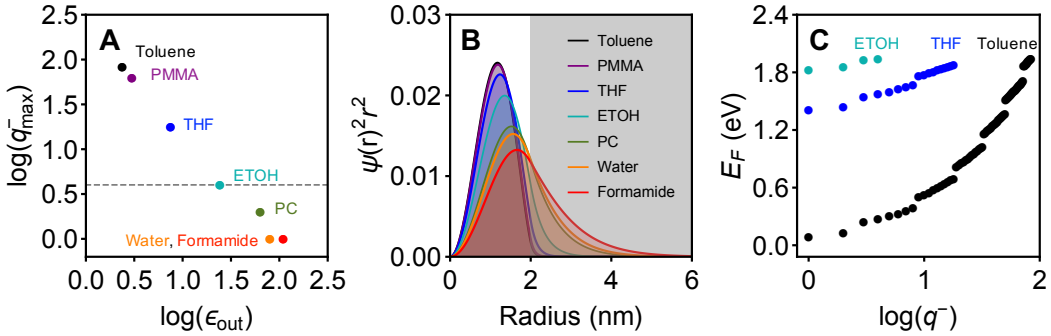

Figure 3.8: Solvent-dependence of the $e^-_{CB_{max}}$ (**A**), 1-e^-_{CB} $\Sigma\psi(r)^2r^2$ (**B**), and E_F (**C**) for $R = 2$ nm ZnO QDs using the "Charged Sphere" model, simulated by varying ϵ_{out}. The Fermi-level zero reference is set to the potential minimum for the QD solvated by toluene. The horizontal dashed line in the leftmost panel denotes the experimentally determined q^-_{max} for colloidal ZnO QDs. Solvent ϵ_{out} were adjusted as follows: toluene ($\epsilon_0 = 2.38$), polymethylmethacrylate (PMMA, $\epsilon_0 = 3$), THF ($\epsilon_0 = 7.56$), ethanol (EtOH, $\epsilon_0 = 24.5$), propylene carbonate (PC, $\epsilon_0 = 64$), water ($\epsilon_0 = 80.1$), and formamide ($\epsilon_0 = 111$)

3.2.8 Surface Proximity of Charge-Balancing Cations

The dependence of E_F on the distance (ΔR) of charge-balancing cations from QD surfaces was also examined within the "Charged Sphere" model. E_F increases as q^+ moves away from the QD surface, as illustrated in the left-hand-side of Fig. 3.9. To calculate the Coulombic destabilization of displacing charge-balancing cations from the QD surface, an energetic correction of $\frac{q^+}{\epsilon_{out}R} - \frac{q^+}{\epsilon_{out}(R+\Delta R)}$ is added to E_F.

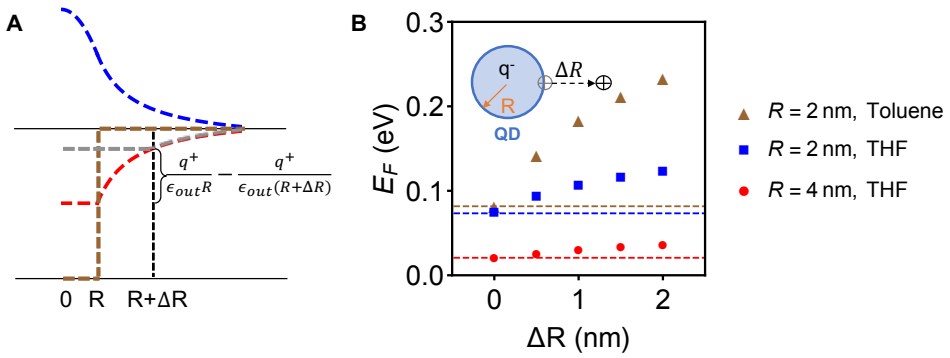

Figure 3.9: **A:** The potential difference resulting from q^+ displacement from the QD surface. Contributions from E_A/ϵ_{out}, q^-, q^+ at R, and q^+ at $R + \Delta R$ are shown in brown, blue, red, and grey, respectively. **B:** Dependence of E_F calculated from the "Charged Sphere" model on the surface proximity of charge-balancing cations (ΔR) for a ZnO QD ($E_A = 4.2$ eV) with $q^- = q^+ = 1$ and varying R and solvent media (ϵ_{out}). Horizontal lines denote the energy at $\Delta R = 0$ for comparison.

The right panel of Figure 3.9 plots E_F of a ZnO QD in the $q^- = q^+ = 1$ limit versus ΔR for a variety of R and ϵ_{out}. $\Delta R = 2$ nm is the largest distance considered. This distance coincides with the approximate length of a typical surface-capping ligand such as trioctylphosphonate. In all cases, displacement of the cations from the QD surfaces leads to destabilization of E_F. Comparing E_F for $R = 4$ nm versus $R = 2$ nm ZnO QDs solvated by THF shows that smaller QDs experience greater Coulombic destabilization. Comparing $R = 2$ nm ZnO QDs solvated by THF ($\epsilon_0 = 7.56$) versus toluene ($\epsilon_0 = 2.38$), on the other hand, illustrates that QDs in weaker dielectric media are more sensitive to cation displacement. Although these results were obtained for $q^- = q^+ = 1$, the correction term scales linearly with q^+ and so similar trends are predicted for other values of q^+ and q^-.

3.3 Computation Details

3.3.1 DFT calculations

All electronic structure calculations were performed using the development version of the Gaussian program.[87] Nearly spherical wurtzite phase ZnO QDs having C_{3v} symmetry were built according to the previously published scheme[8, 9] using lattice parameters from the American Crystal Structure Database. The coordinatively unsaturated surface atoms were passivated using pseudohydrogen atoms with modified nuclear charges of +0.5 and +1.5 to terminate surface O^{2-} and Zn^{2+} ions, respectively, for neutral QDs.[8, 9] In the case of QDs charged with e^-_{CB}, this pseudohydrogen capping scheme also allows us to create a homogenous distribution of surface compensating charges by increasing the nuclear charge of each pseudohydrogen by δ^+ so that $q^+ = \sum \delta^+$. A uniform distribution of fractional charges simulates the realistic scenario of dipoles induced by localized cations and delocalized electrons being counterbalanced by large numbers of other dipoles distributed over the entire QD surface. The PBE0 hybrid DFT functional was used [1, 238, 239] along with the Los Alamos double-ζ pseudopotential and the associated valence double zeta basis (LANL2DZ) for the lattice.[73, 295, 108] This methodology has already shown promising results for the theoretical characterization of diluted magnetic semiconductors, e.g., doped ZnO QDs, and for charged ZnO QDs in the limit of one excess electron.[9, 15, 207, 206, 101, 233, 28] All DFT calculations were performed in vacuum.

3.3.2 Model calculations

The discrete variable representation (DVR) approach[49, 179] is used to numerically solve the Schrödinger equations in the hybrid model. The DVR code is implemented in Python and is publicly available.[183]. A fine grid composed of 1000 Gauss-Hermite quadrature points was employed in the DVR calculations. The eigenfunction and corresponding radial-distribution function were collected with 0.02 nm resolution.

3.4 Theoretical Insights

The "Charged Sphere" model presented above offers four key predictions about excess electron accumulation in colloidal QDs: (i) $\psi(r)^2 r^2$ dramatically shifts toward the QD surfaces with larger ϵ_{out}, R, or ρ_{CB}^-. (ii) For a fixed dielectric medium, QDs with larger values of E_A and ϵ_r can sustain higher $\rho_{CB_{max}}^-(\propto q_{max}^-)$ values. (iii) Weaker dielectric media promote greater $\rho_{CB_{max}}^-$ by increasing the barrier height for electron escape. (iv) Charge-balancing cations closer to the QD surfaces stabilize e_{CB}^- more effectively.

Although the "Charged Sphere" model uses a uniform charge density to construct the interior potential, a key insight is that excess electrons in highly charged QDs shift toward the QD surfaces. The resulting electron density distributions are reminiscent of Schockley or Tamm delocalized surface states.[277] Our analysis suggests that these states become more relevant in larger QDs with greater ρ_{CB}^-.

The "Charged Sphere" model helps explain several experimental observations. For example, the model correctly predicts similar $\rho_{CB_{max}}^-$ in colloidal In_2O_3 and ZnO QDs, determined from experiment to be 2.3×10^{20} cm^{-3} and 1.4×10^{20} cm^{-3}, respectively.[268, 266] Numerically, the model predicts $\rho_{CB_{max}}^-$ of 5.4×10^{20} cm^{-3} for both materials when photodoped in the presence of EtOH. A likely explanation for this higher predicted $\rho_{CB_{max}}^-$ is that the model neglects competing redox transformations such as QD oxidation reactive surface species. As E_F rises with greater ρ_{CB}^-, these processes may dominate. In line with this reasoning, acetaldehyde hydrogenation was invoked previously as introducing a limit to $\rho_{CB_{max}}^-$ in colloidal ZnO QDs photodoped using EtOH as the hole quencher.[40] Interestingly, photodoping ZnO QDs with Li[HBEt$_3$], thereby eliminating formation of acetaldehyde, leads to higher $\rho_{CB_{max}}^-$ of 6×10^{20} cm^{-3}, much more similar to our predicted value. This model, therefore, estimates an upper limit of $\rho_{CB_{max}}^-$ for a QD material in the absence of competing redox processes.

The strong size dependence of q_{max}^- for a given QD material is accurately predicted by the "Charged Sphere" model. Agreement between experiment and calculations in Fig. 3.6B provides a basis for understanding why larger ZnO,[266] In_2O_3, Sn:In_2O_3,[268] and InN[194]

QDs accumulate greater q^-_{max} and display volume-independent $\rho^-_{CB_{max}}$ regardless of whether charges arrive through photodoping, remote chemical doping, or reductive synthetic conditions. Electrons accumulate in QDs until the interior effective potential rises above a threshold value that causes spontaneous charge ejection. Whereas the "Charged Sphere" model simulates this process as QD ionization into solvated electrons and cationic QDs, reports have postulated Zn(0) metal formation in the case of ZnO QD photodoping, for instance.[266] Despite mechanistic differences of charge ejection between experiment and theoretical predictions, the "Charged Sphere" model captures the essence of the strong size dependence of q^-_{max} with remarkable numerical accuracy.

Solvent dependencies of $\rho^-_{CB_{max}}$ are also explainable by the "Charged Sphere" model. A previous study of electrochemical electron injection into a thin-film assembly of $R = 2.15$ ZnO QDs reported a solvent dependence consistent with the one predicted by the "Charged Sphere" model (Fig. 3.8).[258] Electron injection in EtOH, PC, and water led to q^-_{max} values of 4, 2, and 11, respectively, compared to predicted values of 4, 2, and 1 for $R = 2$ ZnO QDs. Interestingly, ϵ_0 of water at the surface of an electrode is known to be at least ten times smaller than its bulk value,[52] which would bring the calculated q^-_{max} for this solvent in line with experiment. The q^-_{max} values predicted by the "Charged Sphere" model for ZnO QDs in toluene, PMMA, and THF are not observed experimentally, however. Lower values of q^-_{max} are observed likely because of competing redox processes, such as charge trapping at surfaces. For example, the high calculated values of q^-_{max} may not be achievable in weak dielectric media because these solvents poorly solubilize cations, leading to ineffective charge compensation at the QD surface and higher E_F. The general agreement with experiments performed in EtOH, PC, and water suggest that among sufficiently strong dielectric media, the key determinant of $\rho^-_{CB_{max}}$ is the ability of the dielectric to screen the QD E_A and stabilize e^-_{CB}. Again, the "Charged Sphere" model estimates an upper limit of $\rho^-_{CB_{max}}$ achievable in a given dielectric medium.

The higher E_F calculated for QDs with q^+ displaced from the surface supports experimental observations that surface electrostatics greatly impact e^-_{CB} stabilization.[29, 41, 40, 47, 30,

126] Altering ΔR simulates the effect of poor ion-pairing and low electrolyte concentrations at the QD surface, with the "Anionic Charged Sphere" model representing an extreme limit of cation displacement. Consistent with experimental evidence, Figure 3.9 predicts these electrostatic factors to impact E_F by hundreds of meV. For example, one report has shown that $R = 1.9$ nm ZnO colloidal QDs in toluene charged to the 1-e^-_{CB} limit are destabilized by 600 mV when compensated by $[CoCp^*_2]^+$ versus H^+.[40] For comparison, the maximum destabilization obtained by displacing cations from the surface of a $R = 1.9$ nm QD solvated by toluene is predicted to be 320 meV (by setting $\Delta R = \infty$). The precise value depends heavily on ϵ_{out}, which likely differs from ϵ_0 of the bulk solvent because the QD surface is surrounded by ligands and other chemical species, in addition to solvent. Reducing ϵ_{out} by half would reproduce the 600 mV destabilization, and is reasonable given solvent exclusion from the QD ligand shell and the weak dielectric ligands used.

Adjusting ΔR can also be used simulate experimental observations that q^-_{max} depends on the electrolyte concentration and composition of the electrical double layer. For example, E_F of Se^{2-}-rich $R = 2.7$ nm CdSe colloidal QDs has been demonstrated experimentally to stabilize by over 250 mV simply by increasing the concentration of $[Bu_4N][PF_6]$ electrolyte, thereby decreasing the length of the electrical double layer and improving charge-compensation at the QD surface. This value is similar to the 224 meV maximum destabilization energy predicted for $R = 2.7$ nm ZnO QDs in toluene (Fig. 3.9). A dependence of E_F on the proximity of charge-balancing cations has also been reported in potentiometric titrations of multiply charged ZnO QDs.[30] Displacing charge-balancing protons from the surfaces of charged ZnO QDs with increasing amounts of bulky non-coordinating diammonium ions leads to systematic destabilization of E_F without changing the number of e^-_{CB}.

Conceptually, the "Charged Sphere" model relates to the classical electrostatic expression $\Delta V = \mu N/\epsilon_0$ invoked previously to calculate the shift ΔV of QD band-edge potentials resulting from a surface density N of dipoles with magnitude μ.[41, 47, 126] Both predict a shift of E_F when the QD surface is surrounded by separated point charges screened by a dielectric medium. Whereas the expression above treats this charge separation specifically

as a dipole with quantifiable strength μ, the "Charged Sphere" model parameterizes this interaction more generally as q^- separated from q^+ by ΔR, allowing a greater variety of surface phenomena to be modeled, such as dependence on electrolyte concentration and coordinating strength of the countercation. Further development of the "Charged Sphere" model will allow more detailed description of specific aspects of the electrical double layer, but these results already provide valuable insight into the electrostatics of QD surfaces.

The accuracy of the "Charged Sphere" model can be improved through several modifications. First, the Schrödinger equation can be solved iteratively by proceeding from $V(r)$ determined through Gauss's Law using the previously calculated electron density. Also, introducing additional parameters to model the electrical double layer and modifying E_A as a function of electron doping level would improve both E_F and $\psi(r)^2 r^2$. The model presented here was chosen to balance convenience and accuracy.

3.5 Conclusions

In summary, we present a quantum model for describing E_F and $\psi(r)^2 r^2$ of excess electrons in multiply charged QDs. This "Charged Sphere" model successfully accounts for inter-electronic and electron-cation interactions using classical electrostatics and exhibits marked quantitative advantages over models that neglect charge-compensating cations at the QD surfaces or inter-electronic interactions. The model is generalizable to many materials and dielectric media by using the adjustable parameters ϵ_R, ϵ_{out}, and E_A. Its predictions agree well with both DFT and experiment. The model's predictions of an expansion of excess electron density toward the QD surfaces and a strong dependence of E_F on the proximity of charge-balancing cations provide a theoretical basis for understanding and quantifying the sensitivity of multiply charged QDs to surface chemistry. Future work will focus on extending this model to p-type semiconductor QDs with excess holes, to aliovalently doped QDs, and to modeling electrical double layers. Beyond providing insights into the characteristics of multiply charged QDs as discussed above, the quantitative description of key experimental factors determining V_{CBE} outlined here will help guide the understanding of

surface electrostatic effects on QD electron-transfer processes including those involved in QD-based photovoltaics, solar photocatalysis, and electrical devices.

Chapter 4

TOWARD ACCURATE MODELING OF NANOMATERIALS WITH RELATIVISTIC EFFECTS

As more and more researchers are pursuing the atomic level deeper understanding of nanomaterials other than energetics and bands/orbitals. Most of the electronic, optic, and magnetic properties relies on the accurate description of the wave functions. However, for such purpose, neither numerical methods nor DFT aforementioned can serve as an appropriate method. Chapter 3 has already shown that many approximations need to be considered to convert the model into a numerically solvable problem, which jeopardizes the completeness of physics. On the other hand, DFT is well-known for its deficiency of treating systems with multireference in nature, *e.g.*, open shell singlets. Nevertheless, a lot of nanomaterials and clusters has multireference ground states arise from unpaired electrons in metal d-/f-orbitals. Moreover, the relativistic effect arise from the heavy element centers in the nanomaterials, *e.g.*, lead and iodine in the perovskites, can significantly change the character of the wave functions. Therefore, a relativistic wave-function based method has been developed in this chapter to fully account both dense manifold and relativistic effect. The method has been benchmarked with abundant atomic spectroscopies. It has been implemented in an efficient and computationally economical way to has full compatibility to be applied to nanomaterial systems which are suitable for atomic basis treatment. This chapter is adapted with permission from: Andrew J Jenkins, Hongbin Liu, Joseph M Kasper, Michael J Frisch, Xiaosong Li, *J. Chem. Theory Comput.* **2019**, *15*, 2974-2982, Copyright ©2019 American Chemical Society.[122]

4.1 Introduction

The accurate description of electronic properties of late-row (≥4th) elements in the periodic table and their molecular complexes presents a challenge to modern electronic structure theory. Their dense manifold of nearly degenerate states often demands the treatment of a multi-configurational method, such as the complete-active-space self-consistent field (CASSCF) approach. The strong attraction from their "heavy" nuclei and the presence of unpaired valence electrons require the effects of relativity to be considered. These effects grow in importance further down the periodic table.[243, 244] For example, scalar relativities give rise to radial contraction and stabilization of s and p orbitals and the subsequent radial expansion of outer d and f orbitals due to changes in screening. Relativistic effects also introduce important spin-couplings that are responsible for the unique chemical reactivities, magnetic properties, and optical responses of metal complexes.[74, 244, 251, 81]

To introduce relativistic effects in a multi-configurational framework, Malmqvist *et. al.* developed a computational scheme[200] that includes scalar relativistic effects in a CASSCF optimization via a 2nd-order Douglas-Kroll-Hess Hamiltonian[154] and perturbative one-electron spin-orbit coupling by adapting the CASSCF state interaction (CASSI) approach.[198, 199] This method involves diagonalizing a spin-orbit Hamiltonian in the basis of the optimized CASSCF states, resulting in spin-orbit coupled states that are combinations of CASSCF states of different spin and space symmetry. Further, dynamic correlation was included by shifting the diagonal elements of the spin-orbit Hamiltonian by the CASPT2 energies, giving the final spin-orbit-coupled states referred to here as CASPT2-SOC.[259] In benchmark calculations of spin-orbit splittings of p-block elements, the CASPT2-SOC approach reproduced ground state experimental splittings to within 15%, with a higher error for excited state splittings. An extension to using a restricted active space (RASSI)[200] has allowed studies of larger systems. However, these methods add the spin-orbit coupling *a posteriori* as a perturbation, *i.e.*, the spin-orbit coupling is added after orbital optimization. While these methods have proven to be successful,[93, 92] it has been shown that the

inclusion of spin-orbit coupling in the orbital optimization is required for reasonable atomic ground state spin-orbit splittings, and additionally affects orbital hybridization and molecular properties.[84] Work by Ganyushin and Neese, using a self-consistent LS-coupling scheme, also found that inclusion of spin-orbit coupling has an important effect on the configuration expansion coefficients in CASSCF.[94]

A more rigorous way of including relativistic effects is to solve the Dirac equation, involving a four-component (4C) relativistic wavefunction. In recent years there has been much development in the area of multi-configurational four-component methods, including four-component Kramers-restricted multi-configurational SCF (KR-MCSCF)[125, 288, 5] and four-component CASSCF[12, 254], internally contracted CASPT2,[276, 294] internally contracted MRCI,[276] and four-component density matrix renormalization group (DMRG) approach.[141, 13] These methods have also been benchmarked for the spin-orbit splittings of *p*-block elements[327]. Solution of the Dirac equation with four-component framework is inherently more computationally demanding than solution of the Schrödinger equation. For the specific case where one is only concerned with studying scalar-relativistic effects, the cost can be reduced by using a spin-free Dirac-Coulomb Hamiltonian, where the spin-free and spin-dependent parts of the four-component equation have been decoupled, and the spin-dependent term discarded. This approach has been used in a spin-free CASSCF implementation,[186] and results in a real wavefunction with full spin and spatial symmetry, significantly reducing the number of integrals to be evaluated, therefore reducing the cost.

To tackle the general case, much effort has been made to decouple the four-component equations into two-component electronic and positronic equations, retaining the key physical relativistic effects of the full four-component equations, but at a reduced computational cost. The Douglas-Kroll-Hess (DKH) and exact two-component (X2C)[70, 111, 249, 250, 311] methods are popular approaches that decouple the four-component Hamiltonian into a reduced dimension electronic two-component Hamiltonian. [158, 192, 234, 118, 193, 189, 265, 175, 235, 75, 98, 147, 76] Relativistic two-component DMRG using the tenth-order Douglas-Kroll-Hess (DKH) one-electron Hamiltonian with scalar-relativistic effects[216] and relativis-

tic generalized Van Vleck second-order perturbation theory (GVVPT2) using the spin-free X2C Hamiltonian[286] have shown promise in resolving challenging multireference electronic structure problems. In this work, we present a two-component CASSCF method within the one-electron X2C framework that includes both scalar relativistic and one-electron spin-orbit coupling. This includes the spin-orbit coupling within the CASSCF orbital optimization, *i.e.*, it is non-perturbative in nature, allowing the orbital shape to adjust as a result of the coupling. The method is benchmarked against experimental values for the spin-orbit splitting of ground and low-lying excited states of *p*-block atoms and further applied to the splittings of transition metals. It should be noted that examples of two-component CASSCF methods that do not include a decoupling scheme have been presented previously[85, 135, 137], where relativistic effects may be included via a two-component effective core potential.

4.2 Theory

In this section the following notation will be used: *i,j,k,l* label inactive MOs; *t,u,v,w* label active MOs; *a,b,c,d* label virtual MOs; *p,q,r,s* label general MOs; *I,J,K* label Slater determinants. Note that the nature of relativistic Hamiltonian requires variational electronic structure methods to be formulated using complex arithmetic. The following discussions assume all quantities are complex-valued unless stated otherwise.

4.2.1 Relativistic X2C-HF Reference

The relativistic two-component CASSCF method developed in this work utilizes spinor molecular orbitals from a relativistic X2C-HF reference. In this section we provide a brief overview of relativistic electronic Hamiltonian and its two-component formalism in the context of Hartree-Fock theory. We refer readers to Refs. 74, 251, 191 for a more thorough review of the subject matter.

The Dirac equation utilizes a four-component wavefunction of the form

$$\Psi \mapsto \begin{pmatrix} \psi_L \\ \psi_S \end{pmatrix} \tag{4.1}$$

where ψ_L and ψ_S are two-component spinors known as the large and small components. Expressing one-electron wavefunctions in a finite kinetically-balanced basis set, the Dirac equation in matrix form is given by[74, 251, 191]

$$\begin{pmatrix} \mathbb{V} & \mathbb{T} \\ \mathbb{T} & (\frac{1}{4c^2}\mathbb{W} - \mathbb{T}) \end{pmatrix} \begin{pmatrix} \mathbb{C}_L^+ & \mathbb{C}_L^- \\ \mathbb{C}_S^+ & \mathbb{C}_S^- \end{pmatrix} = \begin{pmatrix} \mathbb{S} & \mathbf{0}_2 \\ \mathbf{0}_2 & \frac{1}{2c^2}\mathbb{T} \end{pmatrix} \begin{pmatrix} \mathbb{C}_L^+ & \mathbb{C}_L^- \\ \mathbb{C}_S^+ & \mathbb{C}_S^- \end{pmatrix} \begin{pmatrix} \boldsymbol{\epsilon}^+ & \mathbf{0}_2 \\ \mathbf{0}_2 & \boldsymbol{\epsilon}^- \end{pmatrix} \tag{4.2}$$

where c is the speed of light, $\mathbb{C}$ are the basis set expansion coefficients, and $\boldsymbol{\epsilon}$ are orbital energies. "+" and "−" refer to solutions that correspond to electrons and positrons, respectively. The matrices $\mathbb{V}$, $\mathbb{T}$ and $\mathbb{S}$ are the non-relativistic, two-component matrix representations of the the potential energy operator, kinetic energy operator, and the overlap, respectively. $\mathbb{W}$ is the relativistic potential energy operator, with matrix elements given by

$$W_{\mu,\nu} = \langle \phi_\mu | \, (\vec{\sigma} \cdot \vec{p}) \, V \, (\vec{\sigma} \cdot \vec{p}) \, | \phi_\nu \rangle \tag{4.3}$$

where $\vec{p}$ is the linear momentum operator, $\vec{\sigma}$ is the vector containing the Pauli spin matrices, and ϕ are kinetically-balanced basis functions. Note that in general Eq. (4.2) is solved in an uncontracted basis over primitives, although it can be recontracted to reduce the number of orbitals in the SCF and post-HF procedures.

In two-component methods such as the exact-two-component (X2C) method,[158, 192, 234, 118, 193, 189, 265, 175, 235] the large and small components of the four-component Dirac equation are decoupled by a unitary transformation $\mathcal{U}$ that block diagonalizes the Hamiltonian:

$$\mathcal{U}^\dagger \hat{\mathcal{H}} \mathcal{U} = \begin{pmatrix} \mathbb{H}^+ & \mathbf{0}_2 \\ \mathbf{0}_2 & \mathbb{H}^- \end{pmatrix} \tag{4.4}$$

Since only electronic solutions are of interest, only the two-component Hamiltonian corresponding to electronic solutions, $\mathbb{H}^+$, need be computed. The X2C transformation takes the

form

$$\mathcal{U} = \begin{pmatrix} (\mathbf{1}_2 + \mathbb{Y}^\dagger\mathbb{Y})^{-1/2} & 0 \\ 0 & (\mathbf{1}_2 + \mathbb{Y}^\dagger\mathbb{Y})^{-1/2} \end{pmatrix} \begin{pmatrix} \mathbf{1}_2 & \mathbb{Y}^\dagger \\ -\mathbb{Y} & \mathbf{1}_2 \end{pmatrix} \tag{4.5}$$

where the matrix $\mathbb{Y}$ is calculated from the orbital coefficients as

$$\mathbb{Y} = \mathbb{C}_S^+(\mathbb{C}_L^+)^{-1} \tag{4.6}$$

Effectively, the X2C transformation eliminates the need to evaluate the small component by "folding" it into the large,

$$\mathcal{U}\begin{pmatrix} \psi_L \\ \psi_S \end{pmatrix} = \begin{pmatrix} \tilde{\psi}_L \\ 0 \end{pmatrix} \tag{4.7}$$

While this transformation is exact for the single electron case, extension to many electron systems requires the decoupling transformation to be applied to the 4-component Dirac-Hartree-Fock equations,[265, 189, 190] which, while more expensive, affords a more accurate description of relativistic effects.

Our implementation does not transform the four-component matrix representation of the two-electron operator, but instead uses the bare Coulomb operator. The leading error in this one-electron X2C approaches arises from the neglect of the transformation of the two-electron Coulomb repulsion operator. To compensate for this error, an empirical correction, known as the Boettger factor, is used to scale the one-electron spin-orbit terms in order to approximately account for the two-electron spin-orbit terms[25]. This approach has been shown to be reasonably accurate in describing spin-orbit splittings of both valence and core electrons.[132, 76, 310, 98, 75]

In the one-electron X2C framework, the transformation (or "picture change") is independent of the two-electron operator. This gives rise to a major advantage of using an effective one-electron X2C approach in the context of CASSCF, which is that the two-component transformation $\mathcal{U}$ becomes invariant with respect to the CASSCF optimization (to be discussed later).

4.2.2 Complex X2C-CASSCF

The CAS wavefunction $|\Psi\rangle$ is described as a linear combination or a configuration interaction (CI) expansion of Slater determinants, $|K\rangle$, constructed from a subset of the orthonormal molecular orbitals (MOs) – the active space.

$$|\Psi\rangle = \sum_{K=1}^{N_{\text{det}}} C_K |K\rangle \tag{4.8}$$

where N_{det} is the total number of determinants in the expansion. For a CAS wavefunction, the active electrons are distributed into the active orbitals in *all* combinations that preserve the symmetry of the system. In the "conventional" one-component CASSCF method, where α and β spin are collinear, the number of determinants that can be constructed is given by a product of binomial coefficients, $N_{\text{det}} = \binom{N_{\text{spatial}}}{n_\alpha}\binom{N_{\text{spatial}}}{n_\beta}$, where n_α and n_β indicate the number of electrons of α and β spin, and N_{spatial} is the number of number of spatial orbitals.

A two-component CASSCF method uses transformed single-occupation molecular spinor orbitals, $\tilde{\psi}_L$ in Eq. (4.7). In the following discussion, we remove the "L" labeling by assuming a decoupling scheme is applied and the pseudo-large component is used. We will also remove the tilde notation but readers should keep in mind that the X2C-CAS method is formulated subject to the "picture change" from the two-component transformation.

X2C-transformed molecular orbitals can be defined as

$$\psi_p(\mathbf{q}) = \begin{pmatrix} \phi_p^\alpha(\mathbf{r}) \\ \phi_p^\beta(\mathbf{r}) \end{pmatrix} \tag{4.9}$$

where the variable $\mathbf{q}$ includes both the spatial coordinate $\mathbf{r}$ and the spin coordinate for one electron. The spatial functions $\{\phi_p^\alpha(\mathbf{r})\}$ and $\{\phi_p^\alpha(\mathbf{r})\}$ are expanded in a common set of real atomic orbital basis functions χ with *complex* coefficients.

$$\phi_p^\alpha(\mathbf{r}) = c_{\mu p}^\alpha \chi_\mu \tag{4.10}$$

$$\phi_p^\beta(\mathbf{r}) = c_{\mu p}^\beta \chi_\mu \tag{4.11}$$

When forming Slater determinants in the two-component CASSCF method, the number

of possible determinants for a two-component CAS is given by

$$N_{\text{det}} = \binom{N_{\text{spinor}}}{n_e} \tag{4.12}$$

where n_e is the total number of active electrons. Note that for a same number of active electrons and molecular orbitals, the two-component CAS space is much bigger than that in the conventional CAS calculation.

The two-component CASSCF wavefunction is optimized by making the energy stationary with respect to variations of *both* the configuration parameters and the MO coefficients. For the complex CI coefficients, this is achieved via solution of the CAS-configuration interaction (CASCI) eigenvalue equation. The complex spinor orbitals are optimized via a unitary transformation of the existing orbitals

$$\psi'_p(\mathbf{q}) = R_{pq}\psi_q(\mathbf{q}) \tag{4.13}$$

where the $\mathbf{R}$ matrix may be written in terms of an anti-Hermitian orbital-rotation matrix $\mathbf{X}$:

$$\mathbf{R} = \exp(\mathbf{X}) \tag{4.14}$$

$$X_{pq} = -X^*_{qp} \tag{4.15}$$

The CASSCF wavefunction is optimized when

$$\frac{\partial E}{\partial \mathbf{C}} = 0 \;\; ; \;\; \frac{\partial E}{\partial \mathbf{X}} = 0 \tag{4.16}$$

In the present work the wavefunction is optimized via a two-step procedure.

Complex-Valued Two-Component CI Optimization

The prerequisite of X2C-CASSCF wavefunction optimization is to define the two-component CASSCF energy and Hamiltonian. In contrast to non-relativistic one-component CASSCF where inactive orbitals are doubly occupied, X2C inactive orbitals are singly occupied. Note

that enforcing time-reversal symmetry can lead to the Kramers paired orbital structure, but we choose to formulate X2C-CASSCF in the general Kramers unrestricted case.

The X2C-CASSCF energy is written as,

$$E = \epsilon^c \; + \; \langle \Psi | \hat{H}^{CAS} | \Psi \rangle \tag{4.17}$$

where ϵ^c is the X2C-Hartree-Fock energy of the inactive orbitals (the "core energy") and is defined as

$$\epsilon^c = \sum_i h_{ii} + \frac{1}{2} \sum_{ij} \left[(ii|jj) - (ij|ji) \right] \tag{4.18}$$

and $\hat{H}^{CAS}$ is the active space Hamiltonian and is defined as

$$\hat{H}^{CAS} = \sum_{tu} h^c_{tu} \hat{E}_{tu} + \frac{1}{2} \sum_{tuvw} (tu|vw) \left(\hat{E}_{tu} \hat{E}_{vw} - \delta_{uv} \hat{E}_{tw} \right) \tag{4.19}$$

where h^c is the inactive orbital Fock matrix, and is given by

$$h^c_{tu} = h_{tu} + \sum \left[(tu|ii) - (ti|iu) \right] \tag{4.20}$$

and $\hat{E}_{pq}$ is an operator that excites from molecular orbital q to p and can be written using the usual creation and annihilation operators $\hat{E}_{pq} = a^\dagger_p a_q$. The excitation list is generated using Handy's string based approach [142] adapted to the two-component orbital space.

Note that since ERIs using X2C orbitals are complex valued, they only have a four-fold symmetry instead of eight, as in the case of real-valued ERIs,

$$(tu|vw) = (vw|tu) = (ut|wv)^* = (wv|ut)^*$$

The first step of the 2-step optimization is the solution of the CASCI eigenvalue problem

$$\mathbf{HC} = E\mathbf{C}. \tag{4.21}$$

For large CI expansions the CAS-Hamiltonian matrix will be too large to store. In such cases the matrix-vector product, **HC**, is formed using a *direct* contraction. In the *direct* X2C-CASSCF approach, the matrix-vector product

$$\sigma_L = \sum_L H_{KL} C_L \tag{4.22}$$

is computed *on-the-fly* using Olsen's minimum operation count algorithm.[226] A subsequent Davidson diagonalization procedure[56] for complex arithmetic is performed to solve Eq. (4.21).

X2C Orbital Optimization

The X2C molecular orbitals are optimized via a complex-valued quasi-Newton-Raphson scheme using an approximate diagonal orbital Hessian $\widetilde{\mathbf{H^{oo}}}$,

$$\mathbf{X} = \left(\widetilde{\mathbf{H^{oo}}}\right)^{-1} .\mathbf{g^o} \tag{4.23}$$

where the dimension of $\mathbf{X}$ is doubled compared to the non-relativistic case. The orbital gradient $\mathbf{g^o}$ is given by

$$g^o_{pq} = -(1 - \hat{P}_{pq}) \langle\Psi| [\hat{E}_{pq}, \hat{H}] |\Psi\rangle \tag{4.24}$$

$$= -2(F_{pq} - F^*_{qp}) \tag{4.25}$$

where $\hat{P}_{pq}$ is the permutation operator that satisfies the relation

$$\hat{P}_{pq} F_{pq} = F^*_{qp} \tag{4.26}$$

and p, q run over *all* two-component molecular orbitals. The elements of F are given by

$$F_{pq} = \sum_r \gamma_{pr} h_{qr} + \sum_{rso} \Gamma_{prso} (qr|so) \tag{4.27}$$

γ and Γ are the one- and two-particle density matrices. They are defined as:

$$\gamma_{tu} = \langle\Psi| \hat{E}_{tu} |\Psi\rangle = \sum_{KL} C^*_K C_L \langle K| \hat{E}_{tu} |L\rangle \tag{4.28}$$

$$\Gamma_{tuvw} = \langle\Psi| \hat{E}_{tuvw} |\Psi\rangle = \sum_{KL} C^*_K C_L \langle K| \hat{E}_{tu}\hat{E}_{vw} - \delta_{uv}\hat{E}_{tw} |L\rangle \tag{4.29}$$

The F matrix can be evaluated by blocks, due to the properties of the one- and two-particle density matrices:

$$\begin{aligned} F_{iq} &= F^1_{iq} \\ F_{tq} &= F^2_{tq} \\ F_{aq} &= 0 \end{aligned} \tag{4.30}$$

where F^1 and F^2 are defined as

$$\begin{aligned} F^1_{pq} &= 2\left(h^c_{pq} + \sum_{tu}\gamma_{tu}[(pq|ut) - (pt|uq)]\right) \\ F^2_{tq} &= \sum_{u}\gamma_{tu}h^c_{qu} + \sum_{tuvw}\Gamma_{tuvw}(qu|vw) \end{aligned} \tag{4.31}$$

Since the CASSCF energy is invariant with respect to rotations within each subspace, the only non-zero classes of the orbital gradient are the inactive-active, the inactive-virtual, and the active-virtual. The upper triangular part of the orbital gradient matrix is therefore:

$$\begin{aligned} g^o_{it} &= -2(F^1_{it} - F^{2*}_{ti}) \\ g^o_{ia} &= -2F^1_{ia} \\ g^o_{ta} &= -2F^2_{ta} \end{aligned} \tag{4.32}$$

In this quasi-Newton-Raphson procedure, the gradient is pre-conditioned by an approximate diagonal Hessian, where the non-zero elements are estimated by

$$\frac{1}{2}H^{oo}_{ia,jb} = \delta_{ij}F^1_{ab} \; - \; \delta_{ab}F^1_{ij} \tag{4.33}$$

$$\frac{1}{2}H^{oo}_{ta,ub} = \delta_{tu}h^c_{ab} \; - \; \delta_{ab}F^2_{ta} \tag{4.34}$$

$$\frac{1}{2}H^{oo}_{it,ju} = \gamma_{tu}h^c_{ij} \; + \; \delta_{ij}(F^1_{tu} - F^2_{tu}) \; - \; \delta_{tu}F^1_{ij} \tag{4.35}$$

The present work also makes use of state averaged orbitals[305], where the density matrices used in the orbital optimization process (Eqs. (4.27) and (4.31)) are replaced by an average of the density matrices for a set of states, resulting in orbitals that are optimized for the set of states rather than a single state.

4.2.3 "Picture Change" Effects in X2C-CASSCF

The evaluation of properties in addition to energies requires the corresponding operators to be constructed in the original four component basis and transformed with the same unitary matrix used for the Hamiltonian. However, the CASSCF procedure can also, in principle, modify the transformation matrix itself, affecting both the energy and other properties.

While the CI part of the CASSCF procedure is independent of how the two-component molecular orbitals are obtained, the orbital rotation in CASSCF is closely connected to the 4c-to-2c transformation. This point can be seen from Eq. (4.5) and Eq. (4.6), where the exact decoupling of the large and small component is constructed from orbital coefficients. Since orbital rotation will directly modify the orbital coefficients, this, in principle, requires the reconstruction and application of two-component transformation matrix at every CASSCF step. However, the use of the approximate one-electron X2C approach eliminates the need to recompute the two-component transformation matrix in the current implementation. The reason can be traced back to the fact that the two-electron operator is not transformed so the one-electron X2C transformation only depends on the four-component one-electron operator, which does not need to be solved self-consistently.

4.3 Results and Discussion

The relativistic two-component CASSCF method introduced in this work is implemented in the development version of the Gaussian quantum chemistry package.[88] At the current stage, double point group symmetries are not used. Benchmark tests include calculations of spin-orbit splittings of p- and d-block elements, using relativistic and non-relativistic versions of two-component CASSCF. Non-relativistic calculations use molecular orbitals from generalized Hartree-Fock (GHF) without relativistic corrections as reference orbitals in a CASCI or in a CASSCF calculation, referred to here as GHF-CASCI and GHF-CASSCF respectively. Relativistic calculations use X2C-HF molecular orbitals, including both scalar relativities and effective one-electron spin-orbit couplings. These calculations are referred to as X2C-CASCI and X2C-CASSCF. Use of state averaging in the CASSCF orbital optimization is also indicated.

4.3.1 Recovering the Energetic Ordering and Degeneracy of Fine Structure Splitting

Perturbative treatment of spin-orbit coupling may predict the energetic splitting with a reasonable accuracy, but the broken degeneracy of orbitals arising from spin-orbit coupling

State	GHF-SA-CASSCF	X2C-CASCI	X2C-SA-CASSCF
1	−161.8413411	−162.0340508	−162.0339674
2	−161.8413411	−162.0189330	−162.0339674
3	−161.7682878	−161.9571497	−161.9607845
4	−161.7682878	−161.9571312	−161.9607845
5	−161.7682878	−161.9571125	−161.9607195
6	−161.7682878	−161.9493940	−161.9607195
7	−161.7682878	−161.9493814	−161.9607195
8	−161.7682878	−161.9493690	−161.9607195

Table 4.1: The energy (in Hartree) of the first 8 states of Na calculated from the X2C or GHF reference.

can only be obtained from a variational calculations. In this section, we investigate the fine structure of the sodium atom to understand characteristics of the two-component CAS methods. For simplicity we use a 6-31G basis, as the purpose of the calculations in this section is to understand the qualitative nature of the solutions obtained using different CAS methods rather to obtain quantitative agreement with experiment. As mentioned above, we perform the four-component part of the X2C calculation over uncontracted primitives, but recontract the basis for the subsequent SCF and post-SCF calculations. A valence active space, *i.e.*, $3s$ and $3p$, is used, resulting in 1 electron in 8 spin-orbitals – CAS(1,8). In order to treat all states on an equal footing, CASSCF calculations reported make use of equal state averaging over 8 states.

Table 4.1 compares the energetics of the lowest 8 states obtained from various CAS calculations and the energetic alignment are schematically shown in Fig. 4.1. In the non-relativistic regime where the spin-orbit coupling is absent, all states exhibit separate orbital and spin degeneracies, $(2S+1)(2L+1)$, where S and L are spin and orbital angular momenta.

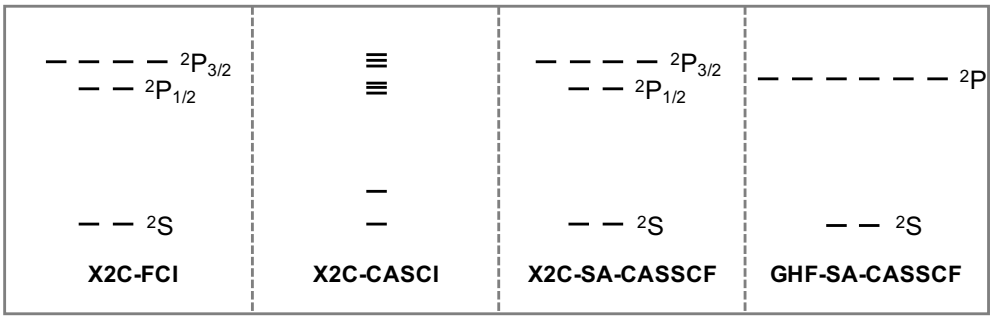

Figure 4.1: Schematic diagram of the eight lowest energy states obtained for the Na atom using different electronic structure theories. Acronyms are defined in main text.

The two-component non-relativistic state-averaged CASSCF (GHF-SA-CASSCF) solution correctly recovers the doubly degenerate ^{2}S states and the 6-fold degeneracy of the ^{2}P state. When relativistic effects are included, scalar relativities contract core levels, leading to a lower system energy compared to that in the non-relativistic case. In addition, spin-orbit coupling splits ^{2}P to doubly degenerate $^2P_{1/2}$ and quadruply degenerate $^2P_{3/2}$ levels. However, the X2C-CASCI(1,8) calculation without orbital optimization is unable to produce the correct degeneracies because the orbitals are optimized for one state. The correct degeneracy is recovered only when the orbitals are optimized equally for all relevant states in X2C-SA-CASSCF or in the limit of full-CI (FCI).

As we approach the limit of full CI, the appropriate symmetry is recovered through mixing in more determinants. The qualitatively correct solution is obtained once all of the states with the same symmetry as the true ground state are included. Since full-CI is not feasible, the correct degeneracy can be recovered by optimizing the orbitals for the set of states of interest, in a state average CASSCF framework, such that all spin manifolds feel the same mean-field potential. Although, symmetry is not enforced from the beginning but is recovered later via variational SA-CASSCF. This is in contrast to other methods that explicitly enforce Kramers pairing in the MCSCF/CASSCF procedure, or use a closed-shell reference.

Although not the focus, the value of the sodium '*d*-line' splitting between the $^2P_{1/2}$ and

$^2P_{3/2}$ states, caused by spin-orbit coupling, can be calculated from Tab. 4.1. For X2C-SA-CASSCF, the splitting is 1.8meV, compared to the experimental value of 2.1meV[149].

4.3.2 Fine Structure Splitting in p-Block Elements

In this section, we benchmark the ground and excited state fine structure splitting of lower p-block elements (rows 4-6), from Gallium (31) to Astatine (85), where the relativistic effects, especially the spin-orbit coupling, start to become pronounced. For all elements in this section we use the Sapporo-DKH3-DZP basis set [225], which is optimized for use in relativistic calculations. As before, the four-component part of the X2C calculation is over uncontracted primitives, while the contracted basis is used for the remainder of the CASSCF procedure. In the relativistic X2C-CASSCF calculations we use an active space of the valence s and p orbitals of the atoms and state averaging. All states arising in the fine structure are included in the state averaging, this varies between groups and is detailed in Tab. 4.5. The calculated values are compared with the experimental atomic spectra obtained from the NIST database[149]. For reference, literature values obtained via two other computational methods are also shown; the perturbative CASPT2-SOC[259] method and the four-component Dirac-Coulomb-Breit CASSCF method[327]. These results were obtained using larger basis sets than the calculations presented here, meaning a direct comparison is not possible but they do serve as a useful guide to the accuracy of the available methods.

Table 4.2: The ground state ^{2}P energy splitting in group 13 and 17 elements. Percentage errors with respect to experiments are reported in parentheses.

	$^2P_{1/2} \rightarrow {}^2P_{3/2}$ (meV)			
Group 13	X2C-SA-CASSCF	4C-CASSCF	CASPT2-SOC	Exp
Ga	87(14.7%)	85(16.7%)	99(2.9%)	102
In	201(26.6%)	229(16.4%)	261(4.7%)	274
Tl	700(27.5%)	-	893(7.6%)	966

	$^2P_{3/2} \rightarrow {}^2P_{1/2}$ (meV)			
Group 17	X2C-SA-CASSCF	4C-CASSCF	CASPT2-SOC	Exp
Br	464 (1.5%)	457(0.0%)	422(7.6%)	457
I	909(3.5%)	951 (1.0%)	863(8.3%)	942
At	2529	-	2517	-

	$^2D_{3/2} \rightarrow {}^2D_{5/2}$ (meV)			
Group 15	X2C-SA-CASSCF	4C-CASSCF	CASPT2-SOC	Exp
As	46(15.0%)	44(10.0%)	25(37.5%)	40
Sb	175(4.8%)	187(12.0%)	114(31.7%)	167
Bi	558(11.8%)	-	465(6.8%)	499

	$^2P_{1/2} \rightarrow {}^2P_{3/2}$ (meV)			
Group 15	X2C-SA-CASSCF	4C-CASSCF	CASPT2-SOC	Exp
As	50(12.3%)	-	30(47.3%)	57
Sb	217(15.6%)	-	156(39.3%)	257
Bi	1088(23.7%)	-	1017(28.7%)	1426

Table 4.4: The excited state ^{2}D and ^{2}P energy splittings in group 15 elements. Percentage errors with respect to experiments are reported in parentheses.

	$^3P_0 \rightarrow {}^3P_1$ (meV)			
Group 14	X2C-SA-CASSCF	4C-CASSCF	CASPT2-SOC	Exp
Ge	62(10.1%)	63(8.7%)	60(13%)	69
Sn	173(17.6%)	192(8.6%)	179(14.8%)	210
Pb	700(27.9%)	-	826(14.9%)	971

	$^3P_0 \rightarrow {}^3P_2$ (meV)			
Group 14	X2C-SA-CASSCF	4C-CASSCF	CASPT2-SOC	Exp
Ge	162(7.4%)	163(6.8%)	154(12.0%)	175
Sn	384(9.6%)	414(4.5%)	378(11.1%)	425
Pb	1131(14.3%)	-	1196(9.3%)	1320

	$^3P_2 \rightarrow {}^3P_1$ (meV)			
Group 16	X2C-SA-CASSCF	4C-CASSCF	CASPT2-SOC	Exp
Se	246(0%)	242(1.6%)	229(6.9%)	246
Te	544(7.6%)	571(3%)	537(8.8%)	589
Po	1758(15.8%)	-	1818(12.9%)	2087

	$^3P_2 \rightarrow {}^3P_0$ (meV)			
Group 16	X2C-SA-CASSCF	4C-CASSCF	CASPT2-SOC	Exp
Se	317(0.6%)	312(1.0%)	302(4.2%)	315
Te	566(3%)	585(0.2%)	600(2.7%)	584
Po	973(4.1%)	-	1134(21.2%)	935

Table 4.3: The ground state ^3P energy splitting in group 14 and 16 elements. Percentage errors with respect to experiments are reported in parentheses.

Table 4.2 presents the ground state fine structure splitting of groups 13 and 17. For both groups 13 and 17, the p^1 and p^5 electron configurations give rise to a ^{2}P ground state. Table 4.3 presents the ground state fine structure splitting of groups 14 and 16. For groups 14 and 16, the p^2 and p^4 electron configurations both give rise to ^{3}P ground states without spin-orbit coupling. For group 15 elements, since they have a ^{4}S ground state configuration, we focus on the fine structure splittings of excited states ^{2}D and ^{2}P (Tab. 4.4).

According to the fine structure rule, in the case of less than half-filled shells levels with a lower J value in the same term are lower in energy, and vice versa in the case of more than half-filled shells. The energetic ordering of spin-orbit split levels is $^3P_{1/2} < {}^3P_{3/2}$ for group 13 elements, $^3P_{3/2} < {}^3P_{1/2}$ for group 17 elements, $^3P_0 < {}^3P_1 < {}^3P_2$ for group 14 elements, and $^3P_2 < {}^3P_1 < {}^3P_0$ for group 16 elements. Although, experimental measurements suggest that Te and Po in group 16 violate the empirical fine structure rule.

For most cases, X2C-SA-CASSCF predicts the correct energetic ordering of the spin-orbit split levels, out-performs CASPT2-SOC, and produces results comparable to the 4C-CASSCF values. There are a few noticeable exceptions. For group 13 elements, both variational methods (X2C-SA- and 4C-CASSCF) methods exhibit a larger percentage error than the perturbative method (CASPT2-SOC). This is likely due to the limited contribution of dynamical correlation in CASSCF methods.

For the Te element in group 16, experimental reference values suggest that $^3P_0$ state lies slightly beneath the $^3P_1$ states with an energy difference of only 5 meV (1% total energy). However, none of the tested methods are able to reproduce the same energetic ordering with the CASPT2-SOC results deviating the most from experiments. Given the small experimental $^3P_0$-$^3P_1$ splitting, we suggest that the discrepancy is likely due to the incompleteness of basis set.

Overall, for the p-block elements tested, X2C-SA-CASSCF, being an approximate two-component method, is able to produce fine structure splittings that are comparable to those computed using the more expensive four-component formalism. The relative error of X2C-SA-CASSCF compared to experiment increases further down the periodic table. In addition

#Group	Electron Configuration	Low Lying States to Average	Total Averaged States
13	s^2p^1	$^2P_{1/2}$, $^2P_{3/2}$	6
14	s^2p^2	$^3P_0$, $^3P_1$, $^3P_2$	9
15	s^2p^3	$^4S_{3/2}$, $^2D_{5/2}$, $^2D_{3/2}$, $^2P_{1/2}$, $^2P_{3/2}$	20
16	s^2p^4	$^3P_2$, $^3P_1$, $^3P_0$	9
17	s^2p^5	$^2P_{1/2}$, $^2P_{3/2}$	6
3	s^2d^1	$^2D_{5/2}$, $^2D_{3/2}$	10
11	s^1d^{10}	$^2S_{1/2}$, $^2D_{5/2}$, $^2D_{3/2}$	12

Table 4.5: The states included in the state-averaging, for different groups

to the incompleteness of basis set, a possible cause for this is the importance of 2-electron spin-orbit coupling. In the present work, only the 1-electron spin-orbit coupling is included, which is then scaled using the Boettger factor in order to account for screening of nuclear charge and other multiple electron effects. This factor does not contain any dependence on the principle quantum number, such that $2p$ and $6p$ electrons have the same screening, leading to larger error further down the group.

4.3.3 Fine Structure Splitting in d-Block Elements

We also apply the X2C-SA-CASSCF method to study the fine structure splitting of selected d-block elements. As with the p-block benchmarks, a Sapporo-DKH3-DZP basis and a valence active space is used. Table 4.6 shows the ground state ^{2}D splitting of the group 3 transition metals and excited state ^{2}D splitting for the group 11 transition metals. For group 3 the ^{2}D ground state splits into 10 states, hence we state average over all 10 states. For group 11 since the ground state is ^{2}S, we report the splitting of the ^{2}D excited state using averaging over all 12 states that result from the splitting of the ground state ^{2}S and excited state ^{2}D. The details of the specific states included are given in Tab. 4.5.

For both groups, the X2C-SA-CASSCF gives the correct energetic ordering of states and

	$^2D_{3/2} \rightarrow {}^2D_{5/2}$ (meV)			$^2D_{5/2} \rightarrow {}^2D_{3/2}$ (meV)	
Group 3	X2C-SA-CASSCF	Exp	Group 11	X2C-SA-CASSCF	Exp
Sc	23(9.5%)	21	Cu	279(10.3%)	253
Y	49(25.7%)	66	Ag	576(4.0%)	554
La	94(27.7%)	130	Au	1443(5.1%)	1521

Table 4.6: The ^{2}D fine structure splitting of group 3 and group 11 elements. Percentage errors with respect to experiments are reported in parentheses.

the agreement with experiment is reasonably good. For group 3, as with the p-block atoms, the error in splittings increases down the group.

4.4 Conclusion

In this work, we have introduced a two-component CASSCF method that includes both scalar relativistic and spin-orbit coupling effects variationally. This is achieved via use of a one-electron X2C transformation of the modified Dirac equation. This approach is variational in nature, allowing the orbitals to be affected by the spin-orbit coupling; a requirement for accurate description of atomic spin-orbit splittings. The formulation developed in this work is for the general Kramers-unrestricted case, and could be extended to include magnetic field effects in the future, where time-reversal symmetry is no longer preserved. In contrast to the pseudo-potential relativistic approach, although not explored here, including core orbitals in the active space may allow studies of excitations involving core electrons, such as those in X-ray spectra.

The qualitative behavior of the method is highlighted by a simple example of spin-orbit splitting – the sodium 'd-line'. This example uses an X2C-GHF reference, but the (case-specific) degeneracy of the α and β spin manifolds and correct spin-orbit splitting structure is restored by optimizing the orbitals using state averaging.

We also test the X2C-SA-CASSCF method for the calculation of the ground and excited

state spin-orbit splitting of lower p- and d-block elements. For all atoms, the experimental ordering of states is successfully reproduced, with the exception of Te. The splitting values have an error of between 0-25%, performing better for rows 4 and 5. These values are comparable to existing literature values for four-component CASSCF implementations, but at a reduced cost since the AO to MO integral transformation can be performed over two-component rather than four-component spinors.

The X2C-SA-CASSCF method provides a practical tool to describe the electronic structure of transition metals, and other systems where both static correlation and relativistic effects must be accounted for.

Chapter 5

TOWARD ACCURATE MODELING OF NANOMATERIALS WITH COMPLEX ENVIRONMENT AND EXTERNAL FIELD

In Chapter 3, we have used a concise mathematical model to show that the solvent surrounding the colloidal QDs can pronouncedly alter their Fermi-level and electronic wave function of the excess electrons. However, such simple model cannot provide further insights on the more intriguing properties, such as absorption spectrum. In this chapter, we will model such solvation effect in a deeper atomistic level, via employing a so-called QM/MM method, which explicitly incorporate the solvent molecules. Moreover, we have applied real-time framework to include the effect of time-dependent external electric field as well. Though the examples we shown in this chapter is not a real nanomaterial system, the theory and implementation is generalized to any interesting systems, such as metal clusters and quantum dots under atomic basis. This chapter is adapted with permission from: Hongbin Liu, Andrew J Jenkins, Andrew Wildman, Michael J Frisch, Filippo Lipparini, Benedetta Mennucci, Xiaosong Li, *J. Chem. Theory Comput.* **2019**, *15*, 1633-1641. Copyright ©2019 American Chemical Society. [188]

5.1 Introduction

Real-time time-dependent electronic structure theory seeks to solve the time-dependent Schrödinger equation (TDSE) for quantum systems in order to predict and simulate the response to external perturbations [290, 165, 270, 10, 177, 46, 65, 45, 220, 221, 222, 99]. Real-time methods have been applied to many types of spectroscopy[161, 66, 58, 197] as well as studies of charge migration and charge-transfer dynamics. [46, 90, 63, 261, 240, 292, 123]. A commonly used real-time approach is the real-time time-dependent density functional the-

ory (RT-TDDFT),[43, 59, 171, 178, 64, 100, 98, 132, 196, 197, 78] making use of TDDFT, one of the most prevalent methods for the study of excited state properties and absorption spectra of molecular systems. However, available DFT functionals used in RT-TDDFT are adiabatic, *i.e.* the exchange-correlation potentials do not change in time, and are designed for the ground state, leading to many known problems.[262, 91, 246, 242]

Recently, wave function based real-time electronic structure theory in the framework of time-dependent configuration interaction (TD-CI) has been used for the calculation of absorption spectra and non-linear optical properties in vacuum.[166, 236, 80, 278, 291] Since the full TD-CI method is not computationally feasible except for very small molecular systems, the CI expansion is often truncated in terms of either the excitation operator (*e.g.*, singles and doubles) or the space used to construct the CI basis (*e.g.*, the complete active space approach). Both types of truncated TD-CI methods have shown promise in simulating multi-electron dynamics driven by external perturbations. [166, 236, 291]

An external perturbation of great chemical interest is the interaction between a molecule and its environment, such as a solvent or protein. It is well known that this perturbation can lead to changes in fundamentally dynamical properties of a molecule, as seen by solvatochromic shifts in spectra of chromophores [248, 284, 205, 127, 42] or solvent induced modifications to electron transfer rates.[46] Although the importance of such a perturbation is widely recognized, care must still be taken when choosing a model to simulate the solute-solvent interaction. An effective and increasingly popular approach consists in adopting a so-called polarizable embedding scheme, which includes atomistic descriptions of the environment while also allowing for mutual polarization between the molecule and its environment. Many different models belong to the family of polarizable embedding, including, but not limited to the "Effective Fragment Potential Method"[57, 130] and the polarizable molecular mechanics models, which can be based on induced dipoles[55, 38, 37, 203, 195] (MMPol), fluctuating charges[255, 256, 184, 185], or Drude oscillators[27]. Numerous recent efforts have been devoted to improving the accuracy of spectral simulations in an environment through the lens of polarizable embedding. Hedegård *et al.* implemented a multi-configuration self-

consistent field (MCSCF) within their own polarizable embedding framework and used it to get the solvatochromic shift of the first absorption in acetone and uracil.[109] Li *et al.* combined the induced dipole formalism of MMPol with the complete active space self-consistent field (CASSCF)[260, 124] method to accurately capture the solvation effect of water on the excited states of cytosine.[170] Donati *et al.* coupled real-time TDDFT to MMPol to simulate the absorption spectrum and the time-dependent dipole in both solvated systems as well as covalently bound protein.[69] Motivated by this final approach, this paper aims to merge the merits of both explicitly time-dependent complete active space (CAS) methods and MMPol to simulate the complex, environment-dependent and multi-electron excited state properties.

We present a time-dependent complete active space configuration interaction (TD-CASCI) method coupled with an MMPol environment. This method is then used to calculate the absorption spectrum of coumarin 153 (C153) in methanol, which has a pronounced and well studied solvatochromic shift, in order to highlight the need for both facets of the model. In addition, we explore the choice of reference orbitals for the TD-CASCI calculation and the implications of the choices on the behavior of the environment. In particular, the behaviors of TD-CASCI simulations using HF, ground state state-specific CASSCF (SS-CASSCF) and state-averaged CASSCF (SA-CASSCF) [304] orbitals in an MMPol environment are compared to determine their suitability for capturing environmental effects on correlated excited states.

5.2 Theory

The time-evolving wave function of a many-electron system is governed by the time-dependent Schrödinger equation:

$$i\frac{\partial\Psi(t)}{\partial t} = \hat{H}(t)\Psi(t) \tag{5.1}$$

In the time-dependent configuration interaction (TDCI) framework, the wave function $\Psi(t)$ is expanded as a linear combination of time-independent Slater determinants $\{\Phi_i\}$:

$$\Psi(t) = \sum_k C_k(t)\Phi_k \tag{5.2}$$

where $\{C_i(t)\}$ are the time-dependent CI coefficients. Within a given basis, the TDCI approach gives the exact time-dependent variational solution of a many-electron system. However, it is not a computationally practical method except for small systems. For large molecules, the TDCI wave function expansion can be restricted in a so-called active space, resulting in a CAS formalism,

$$\Psi^{\mathrm{CAS}}(t) = \sum_{K \in \mathrm{CAS}} C_K(t)\Phi_K \tag{5.3}$$

As the size of the active space increases, the CAS wave function approaches the asymptotic limit of the full CI solution. In the following discussion, we remove the CAS denotation for simplicity, and use the following notation throughout the rest of the paper:

- $K, L, ...$ are Slater determinants in the *active* space.
- $t, u, v, w, ...$ are orbitals in the *active* space.
- $i, j, k, l, ...$ are orbitals in the *inactive* space.
- $a, b, c, d, ...$ are orbitals in the *virtual* space.
- $p, q, r, s, ...$ are any orbitals.
- $\nu, \nu', ...$ are atomic orbitals.

5.2.1 Time-dependent Complete Active Space Approach

With the CAS wave function ansatz in Eq. (5.3), Eq. (5.1) can be written in a matrix form as:

$$i\dot{\mathbf{C}}(t) = \hat{\mathbf{H}}(t)\mathbf{C}(t) \tag{5.4}$$

The Hamiltonian in the determinant basis is

$$H_{KL}(t) = \langle K| \sum_{tu} (h_{tu} + \sum_{i} (2(tu|ii) - (ti|iu)) + V_{tu}^{\mathrm{Ext}}(t)) \hat{E}_{tu} |L\rangle + \langle K| \frac{1}{2} \sum_{tuvw} (tu|vw)(\hat{E}_{tu}\hat{E}_{vw} - \delta_{uv}\hat{E}_{tw}) |L\rangle \tag{5.5}$$

where the h_{pq} and $(pq|rs)$ are the one-electron and two-electron integrals, respectively. $\hat{E}_{pq}$ is an excitation operator

$$\hat{E}_{pq} = \hat{a}_{p\alpha}^{\dagger}\hat{a}_{q\alpha} + \hat{a}_{p\beta}^{\dagger}\hat{a}_{q\beta}. \tag{5.6}$$

The first term in Eq. (5.5) is the effective one-electron Hamiltonian which includes contributions from doubly occupied inactive orbitals and external perturbations. In the presence of an external electric field, $\boldsymbol{\xi}(t)$, the effect of the external perturbation takes on an electric-dipole approximation,

$$V_{tu}^{\mathrm{Ext}}(t) = \mathbf{d}_{tu} \cdot \boldsymbol{\xi}(t) \tag{5.7}$$

$$\mathbf{d}_{pq} = \langle p| \mathbf{r} |q\rangle \tag{5.8}$$

This potential is included in the effective one-electron Hamiltonian in Eq. (5.5)

5.2.2 Time-propagation of Direct TD-CASCI

Propagation of Eq. (5.4) can be carried out in the CI state basis where the time-evolution operator is a unitary matrix.[163, 166, 291] However, propagating the TD-CASCI wave function in the CI state basis requires a full diagonalization of the Hamiltonian and computation of the transition dipole matrix element between all CI states. This is not a computationally practical approach except for small CAS problems.

In this work, we use the second-order symplectic leapfrog method [236, 103, 23] to integrate the TD-CASCI equation in matrix form (Eq. (5.4)) with a *direct* algorithm to form the matrix-vector product.

The first step in the leapfrog propagation of Eq. (5.4) is a first order extrapolation of $\mathbf{C}$ at $t = 0$, $\mathbf{C}(0)$, to $\mathbf{C}$ at $t = \frac{\Delta t}{2}$, $\mathbf{C}(\frac{\Delta t}{2})$:

$$\mathbf{C}(\frac{\Delta t}{2}) = \mathbf{C}(0) + \frac{\Delta t}{2}\dot{\mathbf{C}}(0) \tag{5.9}$$

where $\dot{\mathbf{C}}(t)$ is written as the simple rearrangement of Eq. (5.4):

$$\dot{\mathbf{C}}(t) = -i\hat{\mathbf{H}}(t)\mathbf{C}(t) \tag{5.10}$$

The subsequent steps propagate $\mathbf{C}$ by evaluation of $\dot{\mathbf{C}}$ at the midpoint of the step:

$$\mathbf{C}(t) = \mathbf{C}(t - \Delta t) + \Delta t\ \dot{\mathbf{C}}(t - \frac{\Delta t}{2}) \tag{5.11}$$

The symplectic nature of the scheme ensures the norm is conserved over long-time propagation.[236]

The most time-consuming step of the leapfrog propagation is the evaluation of the matrix-vector product in Eq. (5.10). In the *direct* TD-CASCI approach, the matrix-vector product

$$\sigma_L = \sum_L H_{KL} C_L \tag{5.12}$$

is computed *on-the-fly* using Olsen's minimum operation count algorithm[226]. Combining a *direct*-CI approach with the leapfrog algorithm results in a method with reduced memory requirements, allowing the use of larger CI expansions and the study of larger systems.

5.2.3 Coupling to the Time-dependent Polarizable Force Field

To describe the many-electron dynamics embedded in a polarizable force field, one needs to integrate the mutual polarization between the TD-CASCI and MMPol subsystems during the dynamics. MMPol introduces an additional time-dependent perturbation to the effective one-electron Hamiltonian,

$$V_{tu}^{\mathrm{MMPol}} = -\langle t| \sum_i \frac{q_i}{|\mathbf{r} - \mathcal{R}_i|} + \sum_p \frac{\boldsymbol{\mu}_p(t) \cdot (\mathcal{R}_p - \mathbf{r})}{|\mathbf{r} - \mathcal{R}_p|^3} |u\rangle \tag{5.13}$$

where $\{q_i\}$ are MM charges. Indices i and p label the charge and polarizable sites in the MM region, respectively. $\mathbf{r}$ are electronic degrees of freedom in the QM region and $\mathcal{R}$ are the nuclear degrees of freedom in the MM region.

The two terms in the bracket in Eq. (5.13) give rise to the electrostatic interaction between the QM electrons and the MM charges $\{q_i\}$ and induced dipole $\{\boldsymbol{\mu}_p\}$. The time-dependence of the MM dipoles $\{\boldsymbol{\mu}_p\}$ arises from the time-dependent electric field produced by the MM charges and QM electrons through the following linear equation,

$$\boldsymbol{\mu}_p(t) = \boldsymbol{\alpha}_p \cdot \left(\mathbf{E}_p(t) + \sum_{p' \neq p} S^{(3)}_{pp'} \frac{\boldsymbol{\mu}_{p'}(t)}{|\mathcal{R}_{pp'}|^3} - \sum_{p' \neq p} S^{(5)}_{pp'} \frac{3\mathcal{R}_{pp'}(\mathcal{R}_{pp'} \cdot \boldsymbol{\mu}_{p'}(t))}{|\mathcal{R}_{pp'}|^5} \right) \tag{5.14}$$

$$\mathbf{E}_p(t) = \sum_{i \neq p} q_i \frac{\mathcal{R}_p - \mathcal{R}_i}{|\mathcal{R}_p - \mathcal{R}_i|^3} + \sum_i Z_i \frac{\mathcal{R}_p - \mathbf{R}_i}{|\mathcal{R}_p - \mathbf{R}_i|^3} + \int \rho(\mathbf{r}, t) \frac{\mathcal{R}_p - \mathbf{r}}{|\mathcal{R}_p - \mathbf{r}|^3} d\mathbf{r} \tag{5.15}$$

where $\boldsymbol{\alpha}_p$ and $\mathbf{E}_p(t)$ are the static polarizability tensor and the time-dependent polarization field at the MM site p. $\mathbf{R}$ are nuclear degrees of freedom in the QM region. $S^{(3)_{pp'}}$ and $S^{(5)_{pp'}}$ are screening factors depending on the MM topology, which are introduced to avoid over-polarization effects.[287, 293, 299] In the MMPol scheme used in this work, atomic partial charges[36] and isotropic static atomic polarizabilities[38, 129] in the MM region are employed.

The time-dependent polarization field at the MM site p includes the electric field produced by the time-dependent electronic density of charge $\rho(\mathbf{r}, t)$. In the current implementation, this term is evaluated as

$$\int \rho(\mathbf{r}, t) \frac{\mathcal{R}_p - \mathbf{r}}{|\mathcal{R}_p - \mathbf{r}|^3} d\mathbf{r} = \sum_{\nu\nu'} P_{\nu\nu'}(t) \langle \nu | \frac{\mathcal{R}_p - \mathbf{r}}{|\mathcal{R}_p - \mathbf{r}|^3} | \nu' \rangle \tag{5.16}$$

where $\mathbf{P}$ is the density matrix in the atomic orbital basis.

In this work, only the static polarizabilities of the MM sites are considered, and the MM induced dipoles respond instantaneously to the electric field produced by the time-dependent electronic density of charge $\rho(\mathbf{r}, t)$ at each polarizable site p. This is a reasonable and useful approximation for cases where the electric field generated by the QM region is oscillating much slower than the response in the MM region.[307]

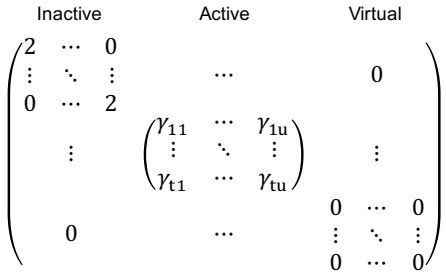

Figure 5.1: Density matrix $\boldsymbol{\gamma}$ in molecular orbital basis.

In the TD-CASCI formalism, the total one-particle density matrix takes on a form illustrated in Fig. 5.1 where all the inactive orbitals are doubly occupied and all virtual orbitals are empty. Only the one-particle density matrix in the active molecular orbital space depends on times. Such a dependence stems from the time-evolution of TD-CASCI,

$$\begin{aligned}
&\gamma_{ii}(t) = 2, \quad \gamma_{ij}(t) = 0, \quad i \neq j \\
&\gamma_{tu}(t) = \langle 0| \hat{E}_{tu} |0\rangle = \sum_{KL} C_K^*(t) C_J(t) \langle K| \hat{E}_{tu} |L\rangle \\
&\gamma_{ab}(t) = 0
\end{aligned} \tag{5.17}$$

However, all electrons, including those in the inactive orbitals, produce polarization fields acting on the MM sites. Therefore, at each time step, the total one-particle density matrix in the molecular orbital space $\boldsymbol{\gamma}(t)$ is transformed to the atomic orbital space $\mathbf{P}(t)$ for the evaluation of the polarization field introduced by the QM region (Eq. (5.16)).

5.2.4 Computation of Absorption Spectrum and Signal Processing

In the *direct* TD-CASCI formalism, the time-dependent dipole moment can be computed as

$$\mu_{x,y,z}(t) = \mathrm{Tr}[\mathbf{d}_{x,y,z}\boldsymbol{\gamma}(t)] \tag{5.18}$$

where $\mathbf{d}$ and $\gamma(t)$ are defined in Eq. (5.8) and Eq. (5.17). Note that only the time-evolving part of the one-particle density matrix can give rise to dipole oscillations and absorption signals.

The initial electric field perturbation corresponds to a step function lineshape lasting for only the initial time-step of width Δt, e.g.

$$\xi(t) = \begin{cases} \xi_{\max}, & 0 \leq t < \Delta t, \\ 0, & \text{else} \end{cases} \tag{5.19}$$

In this case, the discrete Fourier transform of the "delta pulse" $\xi(t)$ will simply be $\xi_{\max}$.

Following this external perturbation the molecular dipole will evolve in time. The absorption spectrum can then be determined by a Fourier transform of the time evolving dipole moment (Eq. (5.18)). Padé approximants, used in this paper, have been shown to produce comparable spectra with far shorter simulation time.[31, 132] The transformed dipole moments can then be used to construct the isotropic dipole strength function

$$S(\omega) \propto \sum_{q=x,y,z} \text{Tr}\left[\omega \cdot \text{Im}\frac{\mu_q(\omega)}{\xi_q}\right] \tag{5.20}$$

to form the absorption spectrum.

5.3 Results and Discussion

5.3.1 Simulation Protocols

The TD-CASCI/MMPol method introduced in this work is implemented in the development version of the Gaussian software package.[89] The case study is the absorption spectrum of the coumarin 153 dye[204, 167, 148, 115, 156, 253, 44, 120, 217, 157], a member of a class of molecules widely employed as sensitizers in solar cells.[227] The time step used in the benchmark calculations is 0.024 attosecond to ensure an accurate interpretation of the results. TD-CASCI/MMPol dynamics are integrated for 15 fs. The external electric field employed to perturb the system had an intensity of 0.001 a.u., low enough to allow a linear approximation of the system response to the perturbation. Computed spectra are compared to experimental measurements and linear response TDDFT results. The PBE0 hybrid functional[1] with the 6-31G(d) basis set [67, 86] is used in the TDDFT calculations. The same basis set is used for the TD-CASCI calculations.

5.3.2 Choosing the CASCI Space and Reference Orbitals

Characteristics of electron wave functions in TD-CASCI calculations strongly depend on the size of the active space and the choice of orbitals used to construct the configurations that expand the CAS wave function (Eq. (5.3)). Three different sets of molecular orbitals are used to construct the active space and their effects on the TD-CASCI spectra are investigated in this work. The three sets of molecular orbitals are fully optimized at the Hartree-Fock (HF) reference, ground state SS-CASSCF, and SA-CASSCF levels, respectively. In the following discussion, we will use TD-CASCI//HF, TD-CASCI//SS-CASSCF, and TD-CASCI//SA-CASSCF notations to describe the choice of molecular orbitals that underly the TD-CASCI simulations.

In order to determine the ideal size of the active space for TD-CASCI simulations, a large active space, CAS(22,16) (22 electrons and 16 orbitals), was initially investigated. We will use the optimized ground state HF reference orbitals in vacuum as a case study to illustrate the strategy to choose the active space. Ground state HF orbitals optimized in vacuum ranging from HOMO−10 to LUMO+4 are included in the CASCI(22,16) calculation. Suggested by a linear response TDHF calculation, these orbitals are mostly responsible for the lowest 15 electronic excitations. Fig. 5.2A shows orbital occupation numbers (Eq. (5.17)) obtained from the CASCI(22,16) calculation. Many orbitals are nearly doubly-occupied (occupation number > 1.95) or empty (occupation number < 0.05) in the lowest 16 CI states including the ground state. Only seven orbitals with significant π characters, HOMO−3 to LUMO+2 (see Fig. 5.2B), are considered active in terms of electron occupation number. This analysis suggests that an active space of 8 electrons and 7 orbitals is sufficient for describing low-energy electronic excitations of coumarin 153 in vacuum. Similar exercises are used to select active spaces for TD-CASCI simulations using molecular orbitals optimized at different levels in vacuum and in MMPol (see Supporting Information, Figure S1 and S2), and result in the same size of active space for all simulations carried out in this work. Therefore, all following TD-CASCI calculations are performed in the CAS(8,7) framework with different

optimized molecular orbital sets shown in Figure S2 in the Supporting Information. The initial condition at $t < 0$ before the field is turned on for each test case is chosen to be the ground state of the CASCI(8,7) solution.

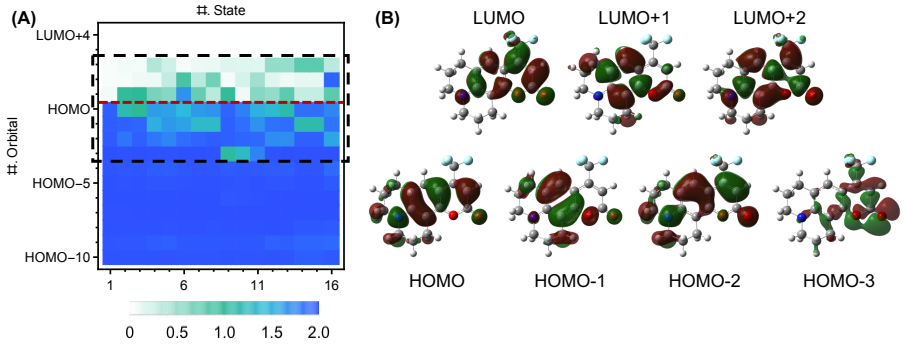

Figure 5.2: **(A)** Orbital occupation numbers, computed using Eq. (5.17), from HOMO−10 to LUMO+4 across the first sixteen states in coumarin 153. **(B)** Seven most *active* orbitals from the analysis in **(A)**.

Figure 5.3 shows absorption spectra of coumarin 153 in vacuum computed using three different TD-CASCI protocols, compared to those obtained with linear response TDDFT and TDHF. All TD-CASCI spectra are blue-shifted compared to those from linear response TDDFT and TDHF calculations. The spectral blue-shift in TD-CASCI is a result of a lack of dynamical correlation when a small active space is used. It should be noted that the TD-CASCI spectrum generated using SS-CASSCF ground state orbitals is more blue-shifted than those using HF and SA-CASSCF orbitals. This occurs because the SS-CASSCF orbitals are optimized solely for the ground state, meaning that the ground state is stabilized compared to the excited states. As a result, the energy gap between the ground and excited states increases, causing a larger blue shift.

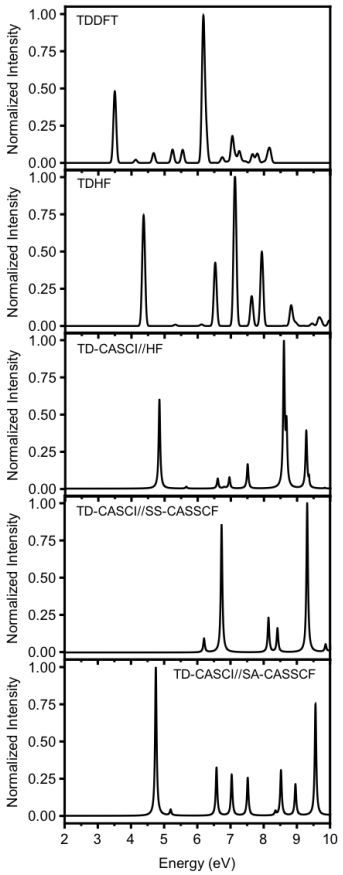

Figure 5.3: Absorption spectra of coumarin 153 in vacuum computed with linear response TDDFT, TDHF, and TD-CASCI using HF, SS-CASSCF, and SA-CASSCF optimized orbitals. Experimentally, the first absorption peak appears at 3.35 eV in vacuum.[217]

Figure 5.4 analyzes two characteristic absorption peaks in TDHF, TDDFT and TD-CASCI//HF spectra, including the first and the most intense peaks. Their contributing MO transitions and Slater determinants are shown with expansion coefficients. Compared to linear response TDDFT and TDHF calculations, most peaks in TD-CASCI//HF spectra consist of similar molecular orbital transitions that correspond to singly excited determinants. One major advantage of TD-CASCI over TDDFT or TDHF is that excited states containing characters beyond that of a single excitation can be resolved. Figure 5.4 shows that the

two characteristic absorption peaks in TD-CASCI//HF spectrum contains double excitation contributions. In particular, the first absorption peak of coumarin 153 in vacuum has a rather significant contribution from a doubly excited Slater determinant that corresponds to two-electron transition from HOMO to LUMO, a character that cannot be captured by linear response TDHF or TDDFT.

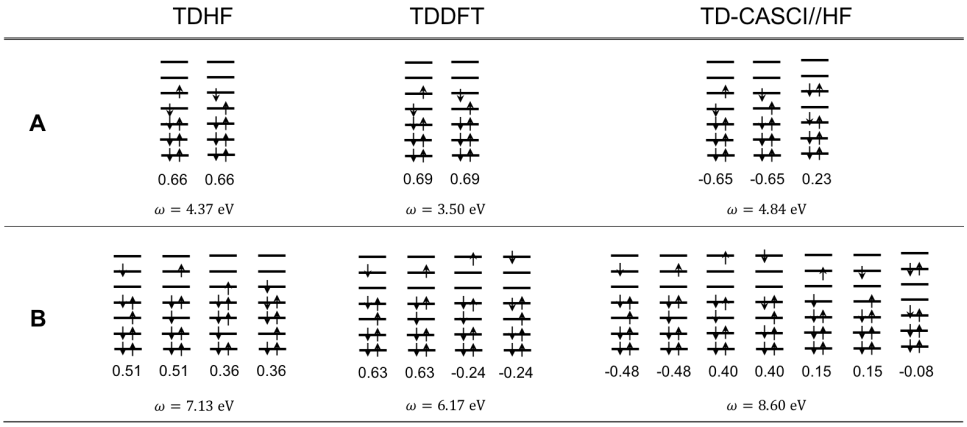

Figure 5.4: MO transition and Slater determinant contributions to the first, (**A**), and most intense, (**B**), absorption peaks for coumarin 153 in vacuum.

5.3.3 Solvatochromic Spectral Shift

The focus of this work is to illustrate the time-dependent interplay between solute electronic excited states and a polarizable environment, and how their interactions manifest in a solvatochromic shift. Therefore, although the absolute absorption peak positions are blue-shifted, we expect that the relative solvatochromic shifts can still be accurately captured by TD-CASCI since they arise due to the perturbation from the environment instead of internal electron correlation.

Experimentally, the lowest absorption peak of coumarin 153 in methanol exhibits a 0.35∼0.44 eV solvatochromic red-shift compared to that in vacuum.[217, 297, 153] The TD-CASCI/MMPol electronic dynamics of the coumarin 153 dye in methanol solvent are simu-

lated to resolve the absorption spectrum and solvatochromic shift. Coumarin 153 was placed in a box of 175 methanol molecules.[121, 119] The solvation box was previously equilibrated using the Amber parm99SB force field.[53, 298, 114]

To simulate electronic dynamics driven by external electric field in solvent, the system is initially prepared in equilibrium with the environment. In other words, molecular orbitals are variationally optimized in the presence of solvent before the external perturbation is turned on. The three self-consistent approaches, including HF, SS-CASSCF, and SA-CASSCF, to obtain molecular orbitals for the active space also represent three different equilibrium conditions to include the solvent effect at $t < 0$. Although at $t > 0$, the time-dependent interaction between the TD-CASCI quantum system and the MMPol subsystem is modeled in the same framework as described in Sec. 5.2.3 for all test cases, the electronic dynamics and spectroscopic signals strongly depend on the initial equilibrium conditions.

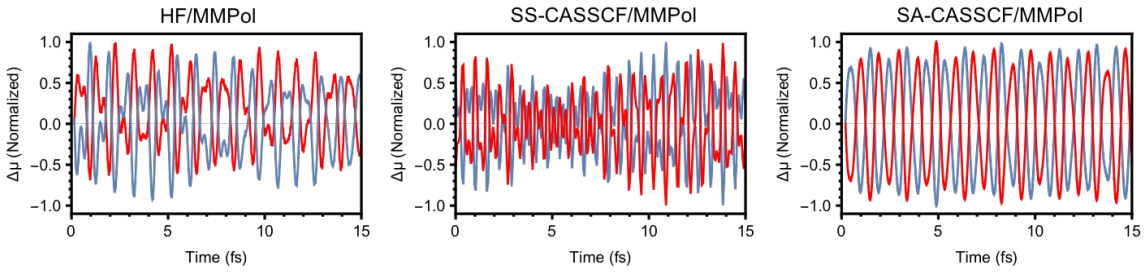

Figure 5.5: Normalized time-dependent net dipole moments of coumarin 153 in methanol after a delta-pulse perturbation, simulated with TD-CASCI/MMPol using different sets of orbitals. The net dipole moments of the QM region are plotted in blue, the net dipole moments of the MM region are plotted in red and have been magnified for 10 times. *left to right*: orbitals optimized at the HF/MMPol, SS-CASSCF/MMPol, and SA-CASSCF/MMPol levels.

Figure 5.5 shows the normalized time-dependent net dipole moments of coumarin 153 in methanol simulated with TD-CASCI/MMPol using solvated orbitals optimized at the HF/MMPol, SS-CASSCF/MMPol, and SA-CASSCF/MMPol levels. Time-dependent net

dipole moments of the MMPol region are also plotted. Since the MM dipoles are propagated instantaneously with the perturbed QM electronic density, an anti-oscillatory behavior of the time-dependent MM dipole is expected. The absorption spectra obtained from the three dipole time series are compared in Fig. 5.6 to the results in vacuum and those obtained with linear response TDDFT/MMPol and TDHF/MMPol calculations in methanol.

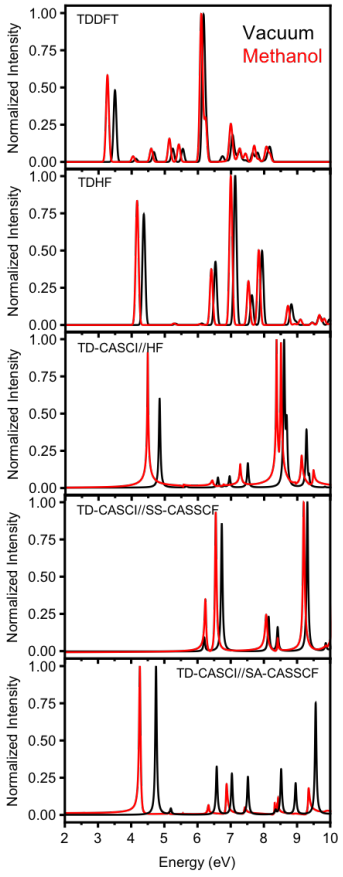

Figure 5.6: Absorption spectra of coumarin in methanol computed with TD-CASCI/MMPol using HF/MMPol, SS-CASSCF/MMPol, and SA-CASSCF/MMPol optimized orbitals (red) compared to their corresponding vacuum spectra (black).

Linear response TDHF and TDDFT exhibit a solvatochromic red-shift of 0.20 eV and

0.24 eV, respectively. In contrast, TD-CASCI simulations using the HF or SA-CASSCF optimized orbitals show a solvatochromic red-shift of of 0.37 eV and 0.44 eV, respectively, for the first absorption peak, in excellent agreement with experimental measurements. From the analysis in Fig. 5.4, this is attributed to the inclusion of higher order excitation contributions which are beyond the capability of linear response TDHF or TDDFT formalisms. However, the simulations using SS-CASSCF orbitals shows the smallest solvatochromic shift. This again is due to the fact that solvated orbitals are solely optimized for the ground state. In the cases of TD-CASCI using solvated HF and SA-CASSCF orbitals, both ground and excited states are treated on an equal footing with the consideration of static correlation and environmental effects. This is an intrinsic nature of the TD-CASCI//HF approach. For TD-CASCI//SA-CASSCF, all relevant states should be considered in the state-average optimization of the solvated orbitals. In the case studied here, the lowest eight states are included in the averaging.

5.4 Conclusion

In this article, we have introduced a coupling scheme that embeds the TD-CASCI method in a polarizable force field, MMPol. The time-evolution of TD-CASCI approach employs a direct matrix-vector contraction *on-the-fly* which allows studies of large scale systems using the TD-CI approach.

The solvatochromic shift of coumarin 153 dye in methanol was studied using the TD-CASCI/MMPol approach developed in this work, compared to experimental measurements and results from linear response TDHF and TDDFT calculations. Although absolute excitation energies from TD-CASCI/MMPol simulations are higher than those calculated using TDHF and TDDFT due to the lack of dynamic correlation, TD-CASCI simulations using HF and SA-CASSCF solvated orbitals out-perform linear response TDHF and TDDFT for the computed solvatochromic shift. The TD-CASCI approach is particularly advantageous because its multi-configurational nature allows the description of the excited states with double-excitation character.

The effect of using different reference orbitals for the TD-CASCI simulation has also been investigated. The use of SS-CASSCF/MMPol solvated orbitals is discouraged because they give rise to a strong bias toward electronic characteristics of the ground state. In order to properly describe the excited state solvatochromic shift, wave functions of all relevant states should be treated on an equal footing. This is the case in the TD-CASCI simulations using HF and SA-CASSCF solvated orbitals which produce a solvatochromic red-shift in excellent agreement with experiments.

The TD-CASCI/MMPol method detailed here is a powerful tool for studying electronic dynamics embedded in a polarizable environment. This method is particularly advantageous when excited states of the quantum subsystem are multi-configurational in nature.

BIBLIOGRAPHY

[1] Carlo Adamo and Vincenzo Barone. Toward reliable density functional methods without adjustable parameters: The PBE0 model. *J. Chem. Phys.*, 110:6158–6170, 1999.

[2] Michael L. Agiorgousis, Yi-Yang Sun, Hao Zeng, and Shengbai Zhang. Strong Covalency-Induced Recombination Centers in Perovskite Solar Cell Material CH3NH3PbI3. *J. Am. Chem. Soc.*, 136:14570–14575, 2014.

[3] Jeffery A. Aguiar, Sarah Wozny, Terry G. Holesinger, Toshihiro Aoki, Maulik K. Patel, Mengjin Yang, Joseph J. Berry, Mowafak Al-Jassim, Weilie Zhou, and Kai Zhu. In Situ Investigation of the Formation and Metastability of Formamidinium Lead Tri-Iodide Perovskite Solar Cells. *Energ. Environ. Sci.*, 9:2372–2382, 2016.

[4] Ghada H Ahmed, Jehad K El-Demellawi, Jun Yin, Jun Pan, Dhinesh Babu Velusamy, Mohamed Nejib Hedhili, Erkki Alarousu, Osman M Bakr, Husam N Alshareef, and Omar F Mohammed. Giant Photoluminescence Enhancement in CsPbCl3 Perovskite Nanocrystals by Simultaneous Dual-Surface Passivation. *ACS Energy Lett.*, 3:2301–2307, 2018.

[5] Adel Almoukhalalati, Stefan Knecht, Hans Jørgen Aa. Jensen, Kenneth G. Dyall, and Trond Saue. Electron Correlation within the Relativistic No-pair Approximation. *J. Chem. Phys.*, 145:074104, 2016.

[6] Anna Amat, Edoardo Mosconi, Enrico Ronca, Claudio Quarti, Paolo Umari, Mohammad K. Nazeeruddin, Michael Grtzel, and Filippo De Angelis. Cation-Induced Band-gap Tuning in Organohalide Perovskites: Interplay of Spin-Orbit Coupling and Octahedra Tilting. *Nano Lett.*, 14:3608–3616, 2014.

[7] Jochen Autschbach. Perspective: Relativistic Effects. *J. Chem. Phys.*, 136:150902, 2012.

[8] Ekateriana Badaeva, Yong Feng, Daniel R. Gamelin, and Xiaosong Li. Investigation of Pure and Co^{2+}-Doped ZnO Quantum Dot Electronic Structures Using the Density Functional Theory: Choosing the Right Functional. *New J. Phys.*, 10:055013, 2008.

[9] Ekateriana Badaeva, Christine M. Isborn, Yong Feng, Stefan T. Ochsenbein, Daniel R. Gamelin, and Xiaosog Li. Theoretical Characterization of Electronic Transitions in Co^{2+}- and Mn^{2+}-Doped ZnO Nanocrystals. *J. Phys. Chem. C*, 113:8710–8717, 2009.

[10] Roi Baer and Recca Gould. A Method for ab initio Nonlinear Electron-density Evolution. *J. Chem. Phys.*, 114:3385–3392, 2001.

[11] Monojit Bag, Lawrence A Renna, Supravat Adhikari, Ramesh Y .and Karak, Feng Liu, Paul M. Lahti, Thomas P. Russell, Mark T. Tuominen, and D. Venkataraman. Kinetics of Ion Transport in Perovskite Active Layers and its Implications for Active Layer Stability. *J. Am. Chem. Soc.*, 137:13130–13137, 2015.

[12] Jefferson E. Bates and Toru Shiozaki. Fully Relativistic Complete Active Space Self-Consistent Field for Large Molecules: Quasi-second-order Minimax Optimization. *J. Chem. Phys.*, 142:044112, 2015.

[13] Stefano Battaglia, Sebastian Keller, and Stefan Knecht. Efficient Relativistic Density-Matrix Renormalization Group Implementation in a Matrix-Product Formulation. *J. Chem. Theory Comput.*, 14:2353–2369, 2018.

[14] Charles W. Bauschlicher, Stephen R. Langhoff, and Peter R. Taylor. Accurate Quantum Chemical Calculations. *Adv. Chem. Phys.*, 77:103–161, 1990.

[15] Rémi Beaulac, Yong Feng, Joseph W. May, Ekaterina Badaeva, Daniel R. Gamelin, and Xiaosong Li. Orbital Pathways for Mn^{2+}-Carrier *sp–d* Exchange in Diluted Magnetic Semiconductor Quantum Dots. *Phys. Rev. B*, 84:195324, 2011.

[16] Michael A Becker, Roman Vaxenburg, Georgian Nedelcu, Peter C. Sercel, Andrew Shabaev, Michael J Mehl, John G. Michopoulos, Samuel G. Lambrakos, Noam Bernstein, John L. Lyons, Thilo Stöferle, Rainer F. Mahrt, Maksym V. Kovalenko, David J. Norris, Gabriele Rainò, and Alexander L. Efros. Bright Triplet Excitons in Caesium Lead Halide Perovskites. *Nature*, 553:189–193, 2018.

[17] T. Berger, M. Sterrer, O. Diwald, E. Knözinger, D. Panayotov, T. L. Thompson, and J. T. Yates, Jr. Light-Induced Charge Separation in Anatase TiO 2 Particles. *J. Phys. Chem. B*, 109:6061–6068, 2005.

[18] Chenghao Bi, Shixun Wang, Qiang Li, Stephen V. Kershaw, Jianjun Tian, and Andrey L. Rogach. Thermally Stable Copper(II)-Doped Cesium Lead Halide Perovskite Quantum Dots with Strong Blue Emission. *J. Phys. Chem. Lett.*, 10:943–952, 2019.

[19] Dongqin Bi, Wolfgang Tress, M. Ibrahim Dar, Peng Gao, Jingshan Luo, Clémentine Renevier, Kurt Schenk, Antonio Abate, Fabrizio Giordano, and Juan-Pablo Correa Baena. Efficient luminescent Solar Cells based on Tailored Mixed-Cation Perovskites. *Sci. Adv.*, 2:e1501170, 2016.

[20] Andreas Binek, Fabian C Hanusch, Pablo Docampo, and Thomas Bein. Stabilization of the Trigonal High-Temperature Phase of Formamidinium Lead Iodide. *J. Phys. Chem. Lett.*, 6:1249–1253, 2015.

[21] Juan Bisquert. Theory of the Impedance of Electron Diffusion and Recombination in a Thin Layer. *J. Phys. Chem. B*, 106:325–333, 2002.

[22] Juan Bisquert, Iván Mora-Sero, and Francisco Fabregat-Santiago. Diffusion–recombination impedance model for solar cells with disorder and nonlinear recombination. *ChemElectroChem*, 1:289–296, 2014.

[23] S. Blanes, F. Casas, and A. Murua. Symplectic Splitting Operator Methods for the Time-dependent Schrödinger Equation. *J. Chem. Phys.*, 124:234105, 2006.

[24] Peter E. Blöchl, Clemens J. Först, and Johannes Schimpl. Projector Augmented Wave Method: Ab Initio Molecular Dynamics with Full Wave Functions. *Bull. Mater. Sci.*, 26:33–41, 2003.

[25] J. C. Boettger. Approximate Two-Electron Spin-Orbit Coupling Term For Density-Functional-Theory DFT Calculations Using The Douglas-Kroll-Hess Transformation. *Phys. Rev. B*, 62:7809–7815, 2000.

[26] Pablo P. Boix, Shweta Agarwala, Teck Ming Koh, Nripan Mathews, and Subodh G. Mhaisalkar. Perovskite Solar Cells: Beyond Methylammonium Lead Iodide. *J. Phys. Chem. Lett.*, 6:898–907, 2015.

[27] Eliot Boulanger and Walter Thiel. Solvent Boundary Potentials for Hybrid QM/MM Computations Using Classical Drude Oscillators: A Fully Polarizable Model. *J. Chem. Theory Comput.*, 8:4527–4538, 2012.

[28] Liam R. Bradshaw, Joseph W. May, Jillian L. Dempsey, Xiaosong Li, and Daniel R. Gamelin. Ferromagnetic Excited-State Mn^{2+} Dimers in $Zn_{1-x}Mn_xSe$ Quantum Dots Observed by Time-Resolved Magnetophotoluminescence. *Phys. Rev. B*, 89:115312, 2014.

[29] Patrick R. Brown, Donghun Kim, Richard R. Lunt, Ni Zhao, Moungi G. Bawendi, Jeffrey C. Grossman, and Vladimir Bulovic. Energy Level Modification in Lead Sulfide Quantum Dot Thin Films through Ligand Exchange. *ACS Nano*, 8:5863–5872, 2014.

[30] Carl K. Brozek, Kimberly H. Hartstein, and Daniel R. Gamelin. Potentiometric Titrations for Measuring the Capacitance of Colloidal Photodoped ZnO Nanocrystals. *J. Am. Chem. Soc.*, 138:10605–10610, 2016.

[31] Adam Bruner, Daniel LaMaster, and Kenneth Lopata. Accelerated Broadband Spectra Using Transition Dipole Decomposition and Padé Approximants. *J. Chem. Theory Comput.*, 12:3741–3750, 2016.

[32] Louis E. Brus. A Simple Model for the Ionization Potential, Electron Affinity, and Aqueous Redox Potentials of Small Semiconductor Crystallites. *J. Chem. Phys.*, 79:5566–5571, 1983.

[33] Louis E. Brus. Electron–electron and Electron-hole Interactions in Small Semiconductor Crystallites: The Size dependence of the Lowest Excited Electronic State. *J. Chem. Phys.*, 80:4403–4409, 1984.

[34] Julian Burschka, Norman Pellet, Soo-Jin Moon, Robin Humphry-Baker, Peng Gao, Mohammad K. Nazeeruddin, and Michael Grätzel. Sequential Deposition as a Route to High-Performance Perovskite-Sensitized Solar Cells. *Nature*, 499:316, 2013.

[35] Duyen H Cao, Constantinos C. Stoumpos, Omar K. Farha, Joseph T Hupp, and Mercouri G. Kanatzidis. 2D Homologous Perovskites as Light-Absorbing Materials for Solar Cell Applications. *J. Am. Chem. Soc.*, 137:7843–7850, 2015.

[36] Stefano Caprasecca, Carles Curutchet, Sandro Jurinovich, and Benedetta Mennucci. PolChat: A Polarisation-Consistent Charge Fitting Tool, Molecolab Tools, 2017.

[37] Stefano Caprasecca, Sandro Jurinovich, Louis Lagardère, Benjamin Stamm, and Filippo Lipparini. Achieving Linear Scaling in Computational Cost for a Fully Polarizable MM/Continuum Embedding. *J. Chem. Theory Comput.*, 11:694–704, 2015.

[38] Stefano Caprasecca, Sandro Jurinovich, Lucas Viani, Carles Curutchet, and Benedetta Mennucci. Geometry Optimization in Polarizable QM/MM Models: The Induced Dipole Formulation. *J. Chem. Theory Comput.*, 10:1588–1598, 2014.

[39] Graham H. Carey, Ahmed L. Abdelhady, Zhijun Ning, Susanna M. Thon, Osman M. Bakr, and Edward H. Sargent. Colloidal Quantum Dot Solar Cells. *Chem. Rev.*, 115:12732–12763, 2015.

[40] Gerard M. Carroll, Alina M. Schimpf, Emily Y. Tsui, and Daniel R. Gamelin. Redox Potentials of Colloidal n-Type ZnO Nanocrystals: Effects of Confinement, Electron

Density, and Fermi-Level Pinning by Aldehyde Hydrogenation. *J. Am. Chem. Soc.*, 137:11163–11169, 2015.

[41] Gerard M. Carroll, Emily Y. Tsui, Carl K. Brozek, and Daniel R. Gamelin. Spectroelectrochemical Measurement of Surface Electrostatic Contributions to Colloidal CdSe Nanocrystal Redox Potentials. *Chem. Mater.*, 28:7912–7918, 2016.

[42] Edward W. Castner Jr, Mark Maroncelli, and Graham R. Fleming. Subpicosecond Resolution Studies of Solvation Dynamics in Polar Aprotic and Alcohol Solvents. *J. Chem. Phys.*, 86:1090–1097, 1987.

[43] Alberto Castro, Heiko Appel, Micael Oliveira, Carlo A. Rozzi, Xavier Andrade, Florian Lorenzen, M. A. L. Marques, E. K. U. Gross, and Angel Rubio. Octopus: A Tool for the Application of Time-dependent Density Functional Theory. *Phys. Status Solidi B*, 243:2465–2488, 2006.

[44] Robert J. Cave and Jr. Edward. W. Castner. Time-Dependent Density Functional Theory Investigation of the Ground and Excited States of Coumarins 102, 152, 153, and 343. *J. Phys. Chem. A*, 106:12117–12123, 2002.

[45] Craig T. Chapman, Wenkel Liang, and Xiaosong Li. Open-System Electronic Dynamics and Thermalized Electronic Structure. *J. Chem. Phys.*, 134:024118, 2011.

[46] Craig T. Chapman, Wenkel Liang, and Xiaosong Li. Solvent Effects on Intramolecular Charge Transfer Dynamics in a Fullerene Derivative. *J. Phys. Chem. A*, 117:2687–2691, 2013.

[47] Menglu Chen and Philippe Guyot-Sionnest. Reversible Electrochemistry of Mercury Chalcogenide Colloidal Quantum Dot Films. *ACS Nano*, 11:4165–4173, 2017.

[48] Ziyong Cheng and Jun Lin. Layered Organic–Inorganic Hybrid Perovskites: Structure, Optical Properties, Film Preparation, Patterning and Templating Engineering. *CrystEngComm*, 12:2646–2662, 2010.

[49] Erica Q. Chong, David B. Lingerfelt, Alessio Petrone, and Xiaosong Li. Classical or Quantum? A Computational Study of Small Ion Diffusion in II-VI Semiconductor Quantum Dots. *J. Phys. Chem. C*, 120:19434–19441, 2016.

[50] Chu-Chen Chueh, Chang-Zhi Li, and Alex K.-Y. Jen. Recent Progress and Perspective in Solution-Processed Interfacial Materials for Efficient and Stable Polymer and Organometal Perovskite Solar Cells. *Energ. Environ. Sci.*, 8:1160–1189, 2015.

[51] Alberto Comin and Liberato Manna. New Materials for Tunable Plasmonic Colloidal Nanocrystals. *Chem. Soc. Rev.*, 43:3957–3975, 2014.

[52] B. E. Conway, J. OM Bockris, and I. A. Ammar. The Dielectric Constant of the Solution in the Diffuse and Helmholtz Double Layers at a Charged Interface in Aqueous Solution. *Trans. Faraday Soc.*, 47:756–766, 1951.

[53] Wendy D. Cornell, Piotr Cieplak, Christopher I. Bayly, Ian R. Gould, Kenneth M. Merz, David M. Ferguson, David C. Spellmeyer, Thomas Fox, James W. Caldwell, and Peter A. Kollman. A Second Generation Force Field for the Simulation of Proteins, Nucleic Acids, and Organic Molecules. *J. Am. Chem. Soc.*, 117:5179–5197, 1995.

[54] Matthew J Crane, Daniel Kroupa, Joo Yeon D Roh, Rayne T Anderson, Matthew D Smith, and Daniel R Gamelin. Single-Source Vapor Deposition of Quantum-Cutting Yb3+: CsPb (Cl1-xBrx) 3 and Other Complex Metal-Halide Perovskites. *ACS Appl. Energy Mater.*, 2019.

[55] Carles Curutchet, Aurora Muñoz-Losa, Susanna Monti, Jacob Kongsted, Gregory D Scholes, and Benedetta Mennucci. Electronic Energy Transfer in Condensed Phase Studied by a Polarizable QM/MM Model. *J. Chem. Theory Comput.*, 5:1838–1848, 2009.

[56] Ernest R. Davidson. The Iterative Calculation of a Few of the Lowest Eigenvalues

and Corresponding Eigenvectors of Large Real-symmetric Matrices. *J. Comput. Phys.*, 17:87–94, 1975.

[57] Paul N. Day, Jan H. Jensen, Mark S. Gordon, Simon P. Webb, Walter J. Stevens, Morris Krauss, David Garmer, Harold Basch, and Drora Cohen. An Effective Fragment Method for Modeling Solvent Effects in Quantum Mechanical Calculations. *J. Chem. Phys.*, 105:1968–1986, 1998.

[58] Umberto De Giovannini, Gustavo Brunetto, Alberto Castro, Jessica Walkenhorst, and Angel Rubio. Simulating Pump–Probe Photoelectron and Absorption Spectroscopy on the Attosecond Timescale with Time-Dependent Density Functional Theory. *ChemPhysChem*, 14:1363–1376, 2013.

[59] A. Eugene DePrince III, Matthew Pelton, Jeffrey R. Guest, and Stephen K. Gray. Emergence of Excited-State Plasmon Modes in Linear Hydrogen Chains from Time-Dependent Quantum Mechanical Methods. *Phys. Rev. Lett.*, 107:196806, 2011.

[60] Christian Dette, Miguel A. Pérez-Osorio, Christopher S. Kley, Paul Punke, Christopher E. Patrick, Peter Jacobson, Feliciano Giustino, Soon Jung Jung, and Klaus Kern. TiO2 Anatase with a Bandgap in the Visible Region. *Nano Lett.*, 14:6533–6538, 2014.

[61] James D. Dill and John A. Pople. Self-Consistent Molecular Orbital Methods. XV. Extended Gaussian-type Basis Sets for Lithium, Beryllium, and Boron. *J. Chem. Phys.*, 62:2921–2923, 1975.

[62] Nada M. Dimitrijevic, Zoran V. Saponjic, Bryan M. Rabatic, Oleg G. Poluektov, and Tijana Rajh. Effect of Size and Shape of Nanocrystalline TiO2 on Photogenerated Charges. An EPR Study. *J. Phys. Chem. C*, 111:14597–14601, 2007.

[63] Feizhi Ding, Craig T. Chapman, Wenkel Liang, and Xiaosong Li. Mechanisms of Bridge-Mediated Electron Transfer: A TDDFT Electronic Dynamics Study. *J. Chem. Phys.*, 137:22A512, 2012.

[64] Feizhi Ding, Joshua J. Goings, Michael J. Frisch, and Xiaosong Li. Ab Initio Non-Relativistic Spin Dynamics. *J. Chem. Phys.*, 141:214111, 2014.

[65] Feizhi Ding, David B. Lingerfelt, Benedetta Mennucci, and Xiaosong Li. Time-Dependent Non-Equilibrium Dielectric Response in QM/Continuum Approaches. *J. Chem. Phys.*, 142:034120, 2015.

[66] Feizhi Ding, Benjamin E. Van Kuiken, Bruce E. Eichinger, and Xiaosong Li. An Efficient Method for Calculating Dynamical Hyperpolarizabilities Using Real-Time Time-Dependent Density Functional Theory. *J. Chem. Phys.*, 138:064104, 2013.

[67] R. Ditchfield, W. J. Hehre, and J. A Pople. Self-Consistent Molecular-Orbital Methods. IX. An Extended Gaussian-Type Basis for Molecular-Orbital Studies of Organic Molecules. *J. Chem. Phys.*, 54:724–728, 1971.

[68] Pablo Docampo and Thomas Bein. A Long-Term View on Perovskite Optoelectronics. *Acc. Chem. Res.*, 49:339–346, 2016.

[69] Greta Donati, Andrew Wildman, Stefano Caprasecca, David B. Lingerfelt, Filippo Lipparini, Benedetta Mennucci, and Xiaosong Li. Coupling Real-Time Time-Dependent Density Functional Theory with Polarizable Force Field. *J. Phys. Chem. Lett.*, 8:5283–5289, 2017.

[70] Marvin Douglas and Norman M. Kroll. Quantum Electrodynamical Corrections to the Fine Structure of Helium. *Ann. Phys.*, 82:89–155, 1974.

[71] Amalie Dualeh, Thomas Moehl, Nicolas Tétreault, Joël Teuscher, Peng Gao, Mohammad Khaja Nazeeruddin, and Michael Grtzel. Impedance Spectroscopic Analysis of Lead Iodide Perovskite-Sensitized Solid-State Solar Cells. *ACS Nano*, 8:362–373, 2013.

[72] Thom H. Dunning Jr. Gaussian Basis Sets for Use in Correlated Molecular Calculations. I. The Atoms Boron Through Neon and Hydrogen. *J. Chem. Phys.*, 90:1007–1023, 1989.

[73] Thom H. Dunning Jr. and P. Jeffery Hay. *Methods of Electronic Structure Theory.* Ed. H. F. Schaefer III, Vol 3, Springer, 1977.

[74] Kenneth G. Dyall and Knut Fægri, Jr. *Introduction to Relativistic Quantum Chemistry.* Oxford University Press, 2007.

[75] Franco Egidi, Joshua J. Goings, Michael J. Frisch, and Xiaosong Li. Direct Atomic-Orbital-Based Relativistic Two-Component Linear Response Method for Calculating Excited-State Fine Structures. *J. Chem. Theory Comput.*, 12:3711–3718, 2016.

[76] Franco Egidi, Shichao Sun, Joshua J. Goings, Giovanni Scalmani, Michael J. Frisch, and Xiaosong Li. Two-Component Non-Collinear Time-Dependent Spin Density Functional Theory for Excited State Calculations. *J. Chem. Theory Comput.*, 13:2591–2603, 2017.

[77] Giles E. Eperon, Samuel D. Stranks, Christopher Menelaou, Michael B. Johnston, Laura M. Herz, and Henry J. Snaith. Formamidinium Lead Trihalide: A Broadly Tunable Perovskite for Efficient Planar Heterojunction Solar Cells. *Energ. Environ. Sci.*, 7:982–988, 2014.

[78] Henk Eshuis, Gabriel G. Balint-Kurti, and Frederick R. Manby. Dynamics of Molecules in Strong Oscillating Electric Fields using Time-Dependent Hartree-Fock Theory. *J. Chem. Phys.*, 128:114113, 2008.

[79] Francisco Fabregat-Santiago, Germà Garcia-Belmonte, Ivan Mora-Sero, and Juan Bisquert. Characterization of Nanostructured Hybrid and Organic Solar Cells by Impedance Spectroscopy. *Phys. Chem. Chem. Phys.*, 13:9083–9118, 2011.

[80] B. Scott Fales and Benjamin G. Levine. Nanoscale Multireference Quantum Chemistry: Full Configuration Interaction on Graphical Processing Units. *J. Chem. Theory Comput.*, 11:4708–4716, 2015.

[81] Dmitri G. Fedorov, Shiro Koseki, Michael W. Schmidt, and Mark S. Gordon. Spin-orbit Coupling in Molecules: Chemistry Beyond the Adiabatic Approximation. *Int. Rev. Phys. Chem.*, 22:551–592, 2003.

[82] Michael Filatov, Wenli Zou, and Dieter Cremer. Spin-Orbit Coupling Calculations with the Two-Component Normalized Elimination of the Small Component Method. *J. Chem. Phys.*, 139:014106, 2013.

[83] Timo Fleig. Relativistic Wave-function Based Electron Correlation Methods. *Chem. Phys.*, 395:2–15, 2012.

[84] Timo Fleig, Hans Jørgen Aa Jensen, Jeppe Olsen, and Lucas Visscher. The Generalized Active Space Concept for the Relativistic Treatment of Electron Correlation. III. Large-scale Configuration Interaction and Multiconfiguration Self-Consistent-Field Four-component Methods with Application to UO_2. *J. Chem. Phys.*, 124:2963–2971, 2006.

[85] Timo Fleig, Christel M. Marian, and Jeppe Olsen. Spinor Optimization for a Relativistic Spin-Dependent CASSCF Program. *Theor. Chem. Acc.*, 97:125–135, 1997.

[86] Michelle M. Francl, William J. Pietro, Warren J. Hehre, J. Stephen Binkley, Mark S. Gordon, Douglas J. DeFrees, and John A. Pople. Self-Consistent Molecular Orbital Methods. XXIII. A Polarization Type Basis Set for Second Row Elements. *J. Chem. Phys.*, 77:3654–3665, 1982.

[87] M. J. Frisch, G. W. Trucks, H. B. Schlegel, G. E. Scuseria, M. A. Robb, J. R. Cheeseman, G. Scalmani, V. Barone, B. Mennucci, G. A. Petersson, H. Nakatsuji, M. Caricato, X. Li, H. P. Hratchian, A. F. Izmaylov, J. Bloino, G. Zheng, J. L. Sonnenberg, W. Liang, M. Hada, M. Ehara, K. Toyota, R. Fukuda, J. Hasegawa, M. Ishida, T. Nakajima, Y. Honda, O. Kitao, H. Nakai, T. Vreven, Jr. J. A. Montgomery, J. E. Peralta, F. Ogliaro, M. Bearpark, J. J. Heyd, E. Brothers, K. N. Kudin, V. N. Staroverov,

T. Keith, R. Kobayashi, J. Normand, K. Raghavachari, A. Rendell, J. C. Burant, S. S. Iyengar, J. Tomasi, M. Cossi, N. Rega, J. M. Millam, M. Klene, J. E. Knox, J. B. Cross, V. Bakken, C. Adamo, J. Jaramillo, R. Gomperts, R. E. Stratmann, O. Yazyev, A. J. Austin, R. Cammi, C. Pomelli, J. W. Ochterski, R. L. Martin, K. Morokuma, V. G. Zakrzewski, G. A. Voth, P. Salvador, J. J. Dannenberg, S. Dapprich, P. V. Parandekar, N. J. Mayhall, A. D. Daniels, Ö. Farkas, J. B. Foresman, J. V. Ortiz, J. Cioslowski, and D. J. Fox. Gaussian Development Version Revision H.21.

[88] M. J. Frisch, G. W. Trucks, H. B. Schlegel, G. E. Scuseria, M. A. Robb, J. R. Cheeseman, G. Scalmani, V. Barone, G. A. Petersson, H. Nakatsuji, X. Li, M. Caricato, A. V. Marenich, J. Bloino, B. G. Janesko, R. Gomperts, B. Mennucci, H. P. Hratchian, J. V. Ortiz, A. F. Izmaylov, J. L. Sonnenberg, D. Williams-Young, F. Ding, F. Lipparini, F. Egidi, J. Goings, B. Peng, A. Petrone, T. Henderson, D. Ranasinghe, V. G. Zakrzewski, J. Gao, N. Rega, G. Zheng, W. Liang, M. Hada, M. Ehara, K. Toyota, R. Fukuda, J. Hasegawa, M. Ishida, T. Nakajima, Y. Honda, O. Kitao, H. Nakai, T. Vreven, K. Throssell, J. A. Montgomery, Jr., J. E. Peralta, F. Ogliaro, M. J. Bearpark, J. J. Heyd, E. N. Brothers, K. N. Kudin, V. N. Staroverov, T. A. Keith, R. Kobayashi, J. Normand, K. Raghavachari, A. P. Rendell, J. C. Burant, S. S. Iyengar, J. Tomasi, M. Cossi, J. M. Millam, M. Klene, C. Adamo, R. Cammi, J. W. Ochterski, R. L. Martin, K. Morokuma, O. Farkas, J. B. Foresman, and D. J. Fox. Gaussian Development Version Revision I.11+.

[89] M. J. Frisch, G. W. Trucks, H. B. Schlegel, G. E. Scuseria, M. A. Robb, J. R. Cheeseman, G. Scalmani, V. Barone, G. A. Petersson, H. Nakatsuji, X. Li, M. Caricato, A. V. Marenich, J. Bloino, B. G. Janesko, R. Gomperts, B. Mennucci, H. P. Hratchian, J. V. Ortiz, A. F. Izmaylov, J. L. Sonnenberg, D. Williams-Young, F. Ding, F. Lipparini, F. Egidi, J. Goings, B. Peng, A. Petrone, T. Henderson, D. Ranasinghe, V. G. Zakrzewski, J. Gao, N. Rega, G. Zheng, W. Liang, M. Hada, M. Ehara, K. Toyota, R. Fukuda, J. Hasegawa, M. Ishida, T. Nakajima, Y. Honda, O. Kitao, H. Nakai,

T. Vreven, K. Throssell, J. A. Montgomery, Jr., J. E. Peralta, F. Ogliaro, M. J. Bearpark, J. J. Heyd, E. N. Brothers, K. N. Kudin, V. N. Staroverov, T. A. Keith, R. Kobayashi, J. Normand, K. Raghavachari, A. P. Rendell, J. C. Burant, S. S. Iyengar, J. Tomasi, M. Cossi, J. M. Millam, M. Klene, C. Adamo, R. Cammi, J. W. Ochterski, R. L. Martin, K. Morokuma, O. Farkas, J. B. Foresman, and D. J. Fox. Gaussian Development Version Revision I.10+.

[90] J. I. Fuks, P. Elliott, A. Rubio, and N. T. Maitra. Dynamics of Charge-Transfer Processes with Time-Dependent Density Functional Theory. *J. Phys. Chem. Lett.*, 4:735–739, 2013.

[91] J. I. Fuks, N. Helbig, I. V. Tokatly, and A. Rubio. Nonlinear Phenomena in Time-Dependent Density-Functional Theory: What Rabi Oscillations Can Teach Us. *Phys. Rev. B*, 84:075107, 2011.

[92] Laura Gagliardi and Björn O. Roos. The Electronic Spectrum of $Re_2Cl_8^{2-}$: A Theoretical Study. *Inorg. Chem.*, 42:1599–1603, 2003.

[93] Laura Gagliardi, Björn O. Roos, Per-Åke Malmqvist, and John M. Dyke. On the Electronic Structure of the UO_2 Molecule. *J. Phys. Chem. A*, 105:10602–10606, 2001.

[94] Dmitry Ganyushin and Frank Neese. A Fully Variational Spin-orbit Coupled Complete Active Space Self-Consistent Field Approach: Application to Electron Paramagnetic Resonance g-tensors. *J. Chem. Phys.*, 138:104113, 2013.

[95] Peng Gao, Michael Grätzel, and Mohammad K. Nazeeruddin. Organohalide Lead Perovskites for Photovoltaic Applications. *Energ. Environ. Sci.*, 7:2448–2463, 2014.

[96] Guillermo Garcia, Raffaella Buonsanti, Evan L. Runnerstrom, Rueben J. Mendelsberg, Anna Llordes, Andre Anders, Thomas J. Richardson, and Delia J. Milliron. Dynamically Modulating the Surface Plasmon Resonance of Doped Semiconductor Nanocrystals. *Nano Lett.*, 11:4415–4420, 2011.

[97] Dylan C. Gary, Sarah E. Flowers, Werner Kaminsky, Alessio Petrone, Xiaosong Li, and Brandi M. Cossairt. Single-Crystal and Electronic Structure of a 1.3 nm Indium Phosphide Nanocluster. *J. Am. Chem. Soc.*, 138:1510–1513, 2016.

[98] Joshua J. Goings, Joseph M. Kasper, Franco Egidi, Shichao Sun, and Xiaosong Li. Real Time Propagation of the Exact Two Component Time-Dependent Density Functional Theory. *J. Chem. Phys.*, 145:104107, 2016.

[99] Joshua J. Goings, Patrick J. Lestrange, and Xiaosong Li. Real-Time Time-Dependent Electronic Structure Theory. *WIREs Comput. Mol. Sci.*, 8:null, 2018.

[100] Joshua J. Goings and Xiaosong Li. An Atomic Orbital Based Real-Time Time-Dependent Density Functional Theory for Computing Electronic Circular Dichroism Band Spectra. *J. Chem. Phys.*, 144:234102, 2016.

[101] Joshua J. Goings, Alina M. Schimpf, Joseph W. May, Robert W. Johns, Daniel R. Gamelin, and Xiaosong Li. Theoretical Characterization of Conduction-Band Electrons in Photodoped and Aluminum-Doped Zinc Oxide (AZO) Quantum Dots. *J. Phys. Chem. C*, 118:26584–26590, 2014.

[102] Victoria Gonzalez-Pedro, Emilio J. Juarez-Perez, Waode-Sukmawati Arsyad, Eva M. Barea, Francisco Fabregat-Santiago, Ivan Mora-Sero, and Juan Bisquert. General Working Principles of CH3NH3PbX3 Perovskite Solar Cells. *Nano Lett.*, 14:888–893, 2014.

[103] Stephen K. Gray, Donald W. Noid, and Bobbt G. Sumpter. Symplectic Integrators for Large Scale Molecular Dynamics Simulations: A Comparison of Several Explicit Methods. *J. Chem. Phys.*, 101:4062–4072, 1994.

[104] Martin A. Green, Anita Ho-Baillie, and Henry J. Snaith. The Emergence of Perovskite Solar Cells. *Nat. Photonics*, 8:506, 2014.

[105] Antonio Guerrero, Germ Garcia-Belmonte, Ivan Mora-Sero, Juan Bisquert, Yong Soo Kang, T Jesper Jacobsson, Juan-Pablo Correa-Baena, and Anders Hagfeldt. Properties of Contact and Bulk Impedances in Hybrid Lead Halide Perovskite Solar Cells Including Inductive Loop Elements. *J. Phys. Chem. C*, 120:8023–8032, 2016.

[106] Qifeng Han, Sang-Hoon Bae, Pengyu Sun, Yao-Tsung Hsieh, Yang Yang, You Seung Rim, Hongxiang Zhao, Qi Chen, Wangzhou Shi, Gang Li, et al. Single Crystal Formamidinium Lead Iodide (FAPbI3): Insight into the Structural, Optical, and Eectrical Properties. *Adv. Mater.*, 28:2253–2258, 2016.

[107] Kimberly H. Hartstein, Alina M. Schimpf, Michael Salvador, and Daniel R. Gamelin. Cyclotron Splittings in the Plasmon Resonances of Electronically Doped Semiconductor Nanocrystals Probed by Magnetic Circular Dichroism Spectroscopy. *J. Phys. Chem. Lett.*, 8:1831–1836, 2017. PMID: 28379708.

[108] P. Jeffery Hay and Willard R. Wadt. Ab initio Effective Core Potentials for Molecular Calculations. Potentials for the Transition Metal Atoms Sc to Hg. *J. Chem. Phys.*, 82:270–283, 1985.

[109] Erik Donovan Hedegård, Nanna H List, Hans Jørgen Aagaard Jensen, and Jacob Kongsted. The Multi-Configuration Self-Consistent Field Method Within a Polarizable Embedded Framework. *J. Chem. Phys.*, 139:044101, 2013.

[110] Larry M Henling and Gary L McPherson. EPR Spectra of Magnetically Coupled Pairs of Gd3+ Ions in Crystals of CsMgCl3, CsMgBr3, and CsCdBr3. *Phys. Rev. B*, 16:4756, 1977.

[111] Bernd A. Hess. Relativistic Electronic-Structure Calculations Employing a Two-Component No-Pair Formalism with External-Field Projection Operators. *Phys. Rev. A*, 33:3742–3748, 1986.

[112] Bernd A. Heß, Christel M. Marian, Ulf Wahlgren, and Odd Gropen. A Mean-Field Spin-Orbit Method Applicable to Correlated Wavefunctions. *J. Chem. Phys.*, 251:365–371, 1996.

[113] Pierre Hohenberg and Walter Kohn. Inhomogeneous Electron Gas. *Phys. Rev.*, 136:B864, 1964.

[114] Viktor Hornak, Robert Abel, Asim Okur, Bentley Strockbine, Adrian Roitberg, and Carlos Simmerling. Comparison of Multiple Amber Force Fields and Development of Improved Protein Backbone Parameters. *Proteins: Struct., Funct., Genet.*, 65:712–725, 2006.

[115] M. L. Horng, J. A. Gardecki, A. Papazyan, and M. Maroncelli. Subpicosecond Measurements of Polar Solvation Dynamics: Coumarin 153 Revisited. *J. Phys. Chem.*, 99:17311–17337, 1995.

[116] Arjan J. Houtepen and Daniël Vanmaekelbergh. Orbital Occupation in Electron-charged CdSe Quantum-dot Solids. *J. Phys. Chem. B*, 109:19634–19642, 2005.

[117] Yinghong Hu, Johannes Schlipf, Michael Wussler, Michiel L Petrus, Wolfram Jaegermann, Thomas Bein, Peter Mller-Buschbaum, and Pablo Docampo. Hybrid Perovskite/Perovskite Heterojunction Solar Cells. *ACS Nano*, 10:5999–6007, 2016.

[118] Miroslaŵ Ilias and Trond Saue. An Infinite-Order Relativistic Hamiltonian by a Simple One-Step Transformation. *J. Chem. Phys.*, 126:064102, 2007.

[119] Roberto Improta, Vincenzo Barone, and Fabrizio Santoro. Ab Initio Calculations of Absorption Spectra of Large Molecules in Solution: Coumarin 153. *Angew. Chem.*, 119:409–412, 2007.

[120] Roberto Improta, Vincenzo Barone, Giovanni Scalmani, and Michael J. Frisch. A State-Specific Polarizable Continuum Model Time Dependent Density Functional Theory Method for Excited State Calculations in Solution. *J. Chem. Phys.*, 125:054103, 2006.

[121] Denis Jacquemin, Aurelien Planchat, Carlo Adamo, and Benedetta Mennucci. TD-DFT Assessment of Functionals for Optical 0-0 Transitions in Solvated Dyes. *J. Chem. Theory Comput.*, 8:2359–2372, 2012.

[122] Andrew J. Jenkins, Hongbin Liu, Joseph M. Kasper, Michael J. Frisch, and Xiaosong Li. Variational Relativistic Two-Component Complete-Active-Space Self-Consistent Field Method. *J. Chem. Theory Comput.*, 15:2974–2982, 2019.

[123] Andrew J. Jenkins, Morgane Vacher, Michael J. Bearpark, and Michael A. Robb. Nuclear Spatial Delocalization Silences Electron Density Oscillations in 2-Phenyl-Ethyl-Amine (PEA) and 2-Phenylethyl-N,N-Dimethylamine (PENNA) Cations. *J. Chem. Phys.*, 144:104110, 2016.

[124] Hans Jørgen Aa Jensen and Hans Ågren. A Direct, Restricted-step, Second-order MC SCF Program for Large Scale ab initio Calculations. *Chem. Phys.*, 104:229–250, 1986.

[125] Hans Jørgen Aa. Jensen, Kenneth G. Dyall, Trond Saue, and Knut Fægri. Relativistic Four-component Multiconfigurational Self-Consistent-Field Theory for Molecules: Formalism. *J. Chem. Phys.*, 104:4083–4097, 1996.

[126] Kwang Seob Jeong, Zhiyou Deng, Sean Keuleyan, Heng Liu, and Philippe Guyot-Sionnest. Air-Stable n-Doped Colloidal HgS Quantum Dots. *J. Phys. Chem. Lett.*, 5:1139–1143, 2014.

[127] Ralph Jimenez, Graham R. Fleming, P. V. Kumar, and Mark Maroncelli. Femtosecond Solvation Dynamics of Water. *Nature*, 369:471–473, 1994.

[128] Hyun Suk Jung and Nam-Gyu Park. Perovskite Solar Cells: From Materials to Devices. *Small*, 11:10–25, 2015.

[129] Sandro Jurinovich, Carles Curutchet, and Benedetta Mennucci. The Fenna–Matthews–Olson Protein Revisited: A Fully Polarizable (TD)DFT/MM Description. *ChemPhysChem*, 15:3194–3204, 2014.

[130] Visvaldas Kairys and Jan H. Jensen. QM/MM Boundaries Across Covalent Bonds: A Frozen Localized Molecular Orbital-Based Approach for the Effective Fragment Potential Method. *J. Phys. Chem. A*, 104:6656–6665, 2000.

[131] Philip Kalisman, Yifat Nakibli, and Lilac Amirav. Perfect Photon-to-Hydrogen Conversion Efficiency. *Nano Lett.*, 16:1776–1781, 2016.

[132] Joseph M. Kasper, Patrick J. Lestrange, Torin F. Stetina, and Xiaosong Li. Modeling $L_{2,3}$-Edge X-ray Absorption Spectroscopy with Real-Time Exact Two-Component Relativistic Time-Dependent Density Functional Theory. *J. Chem. Theory Comput.*, 14:1998–2006, 2018.

[133] Hui-Seon Kim, Sang Hyuk Im, and Nam-Gyu Park. Organolead Halide Perovskite: New Horizons in Solar Cell Research. *J. Phys. Chem. C*, 118:5615–5625, 2014.

[134] Hui-Seon Kim, Ivan Mora-Sero, Victoria Gonzalez-Pedro, Francisco Fabregat-Santiago, Emilio J Juarez-Perez, Nam-Gyu Park, and Juan Bisquert. Mechanism of Carrier Accumulation in Perovskite Thin-Absorber Solar Cells. *Nat. Commun.*, 4:2242, 2013.

[135] Inkoo Kim and Yoon Sup Lee. Two-component Kramers Restricted Complete Active Space Self-Consistent Field Method with Relativistic Effective Core Potential Revisited: Theory, Implementation, and Applications to Spin-Orbit Splitting of Lower p-Block Atoms. *J. Chem. Phys.*, 139:134115, 2013.

[136] Jong H Kim, Po-Wei Liang, Spencer T. Williams, Namchul Cho, Chu-Chen Chueh, Micah S. Glaz, David S. Ginger, and Alex K.-Y. Jen. High-Performance and Environmentally Stable Planar Heterojunction Perovskite Solar Cells Based on a Solution-Processed Copper-Doped Nickel Oxide Hole-Transporting Layer. *Adv. Mater.*, 27:695–701, 2015.

[137] Yong Seok Kim and Yoon Sup Lee. The Kramers' Restricted Complete Active Space Self-Consistent-Field Method for Two-Component Molecular Spinors and Relativis-

tic Effective Core Potentials Including Spin–Orbit Interactions. *J. Chem. Phys.*, 119:12169–12178, 2003.

[138] P. D. C. King, T. D Veal, F. Fuchs, C. Y. Wang, D. J. Payne, A. Bourlange, H. Zhang, G. R. Bell, V. Cimalla, O. Ambacher, R. G. Egdell, F. Bechstedt, and C. F. McConville. Band gap, Electronic Structure, and Surface Electron Accumulation of Cubic and Rhombohedral In2O3. *Phys. Rev. B*, 79:205211, 2009.

[139] Andreas Klein. Electronic properties of In2O3 surfaces. *Appl. Phys. Lett.*, 77:2009–2011, 2000.

[140] Klein, Andreas. Energy Band Alignment in Chalcogenide Thin Film Solar Cells from Photoelectron Spectroscopy. *J. Phys.–Condens. Mat.*, 27:134201, 2015.

[141] Stefan Knecht, Ös Legeza, and Markus Reiher. Communication: Four-component Density Matrix Renormalization Group. *J. Chem. Phys.*, 140:041101, 2014.

[142] Peter J. Knowles and Nicolas C. Handy. A New Determinant-based Full Configuration Interaction Method. *Chem. Phys. Lett.*, 111:315–321, 1984.

[143] M Kobayashi, K Omata, S Sugimoto, Y Tamagawa, T Kuroiwa, H Asada, H Takeuchi, and S Kondo. Scintillation characteristics of CsPbCl3 single crystals. *Nucl. Instrum. Methods Phys. Res.*, 592:369–373, 2008.

[144] Teck Ming Koh, Vignesh Shanmugam, Johannes Schlipf, Lukas Oesinghaus, Peter Müller-Buschbaum, N Ramakrishnan, Varghese Swamy, Nripan Mathews, Pablo P. Boix, and Subodh G. Mhaisalkar. Nanostructuring Mixed-Dimensional Perovskites: A Route toward Tunable, Efficient Photovoltaics. *Adv. Mater.*, 28:3653–3661, 2016.

[145] Weon-kyu Koh, Alexey Y. Koposov, John T. Stewart, Bhola N. Pal, Istvan Robel, Jeffrey M. Pietryga, and Victor I. Klimov. Heavily Doped n-type PbSe and PbS Nanocrystals using Ground-state Charge Transfer from Cobaltocene. *Sci. Rep.*, 3:2004, 2013.

[146] Walter Kohn and Lu Jeu Sham. Self-Consistent Equations Including Exchange and Correlation Effects. *Phys. Rev.*, 140:A1133, 1965.

[147] Lukas Konecny, Marius Kadek, Stanislav Komorovsky, Olga L. Malkina, Kenneth Ruud, and Michal Repisky. Acceleration of Relativistic Electron Dynamics by Means of X2C Transformation: Application to the Calculation of Nonlinear Optical Properties. *J. Chem. Theory Comput.*, 12:5823–5833, 2016.

[148] S. A. Kovalenko, J. Ruthmann, and N. P. Ernsting. Ultrafast Stokes Shift and Excited-State Transient Absorption of Coumarin 153 in Solution. *Chem. Phys. Lett.*, 271:40–50, 1997.

[149] A. Kramida, Y. Ralchenko, J. Reader, and NIST ASD Team. NIST Atomic Spectra Database (version 5.6.1), 2018. National Institute of Standards and Technology, Gaithersburg, MD.

[150] Georg Kresse and Jürgen Furthmüller. Efficiency of Ab-Initio Total Energy Calculations for Metals and Semiconductors Using a Plane-wave Basis Set. *Comput. Mater. Sci.*, 6:15–50, 1996.

[151] Georg Kresse and Jürgen Furthmüller. Efficient Iterative Schemes for Ab Initio Total-Energy Calculations Using a Plane-wave Basis Set. *Phys. Rev. B*, 54:11169, 1996.

[152] Ilka Kriegel, Francesco Scotognella, and Liberato Manna. Plasmonic Doped Semiconductor Nanocrystals: Properties, Fabrication, Applications and Perspectives. *Phys. Rep.*, 674:1–52, 2017.

[153] Robert Królicki, Włodzimierz Jarzęba, Mehran Mostafavi, and Isabelle Lampre. Preferential Solvation of Coumarin 153 - The Role of Hydrogen Bonding. *J. Phys. Chem. A*, 106:1708–1713, 2002.

[154] Norman M. Kroll and Marvin Douglas. Quantum Electrondynamics Corrections to the Fine Structure of Helium*. *Ann. Phys.*, 82:89–155, 1974.

[155] Daniel M Kroupa, Joo Yeon Roh, Tyler J Milstein, Sidney E Creutz, and Daniel R Gamelin. Quantum-Cutting Ytterbium-Doped CsPb (Cl1–x Br x) 3 Perovskite Thin Films with Photoluminescence Quantum Yields over 190%. *ACS Energy Lett.*, 3:2390–2395, 2018.

[156] P. V. Kumar and M. Maroncelli. Polar Solvation Dynamics of Polyatomic Solutes: Simulation Studies in Acetonitrile and Methanol. *J. Chem. Phys.*, 103:3038–3059, 1995.

[157] Yuki Kurashige, Takahito Nakajima, Saki Kurashige, Kimihiro Hirao, and Yoshinori Nishikitani. Theoretical Investigation of the Excited States of Coumarin Dyes for Dye-Sensitized Solar Cells. *J. Phys. Chem. A*, 111:5544–5548, 2007.

[158] Werner Kutzlenigg and Wenjian Liu. Quasirelativistic Theory Equivalent to Fully Relativistic Theory. *J. Chem. Phys.*, 123:241102, 2005.

[159] Jin-Wook Lee, Deok-Hwan Kim, Hui-Seon Kim, Seung-Woo Seo, Sung Min Cho, and Nam-Gyu Park. Formamidinium and Cesium Hybridization for Photo-and Moisture-Stable Perovskite Solar Cell. *Adv. Energy Mater.*, 5:1501310, 2015.

[160] Jin-Wook Lee, Dong-Jin Seol, An-Na Cho, and Nam-Gyu Park. High-Efficiency Perovskite Solar Cells Based on the Black Polymorph of HC (NH2) 2PbI3. *Adv. Mater.*, 26:4991–4998, 2014.

[161] K. M. Lee, K. Yabana, and G. F. Bertsch. Magnetic Circular Dichroism in Real-Time Time-Dependent Density Functional Theory. *J. Chem. Phys.*, 134:144106, 2011.

[162] Michael M. Lee, Joël Teuscher, Tsutomu Miyasaka, Takurou N. Murakami, and Henry J. Snaith. Efficient Hybrid Solar Cells Based on Meso-Superstructured Organometal Halide Perovskites. *Science*, 338:643–647, 2012.

[163] Claude Leforestier, Charly Bisseling, R. H .and Cerjan, M. D. Feit, Rich Friesner, A. Guldberg, A. Hammerich, G. Jolicard, W. Karrlein, H.-D. Meyer, N. Lipkin, O. Roncero, and R. Kosloff. A Comparison of Different Propagation Schemes for the Time Dependent Schrödinger Equation. *J. Chem. Phys.*, 94:59–80, 1991.

[164] Tomas Leijtens, Giles E. Eperon, Nakita K. Noel, Severin N. Habisreutinger, Annamaria Petrozza, and Henry J. Snaith. Stability of Metal Halide Perovskite Solar Cells. *Adv. Energy Mater.*, 5:1500963, 2015.

[165] Manfred Lein, Thomas Kreibich, E. K. U. Gross, and Volker Engel. Strong-Field Ionization Dynamics of a Model H2 Molecule. *Phys. Rev. A*, 65:033403, 2002.

[166] Patrick J. Lestrange, Mark R. Hoffmann, and Xiaosong Li. Time-Dependent Configuration Interaction using the Graphical Unitary Group Approach: Nonlinear Electric Properties. *Adv. Quantum Chem.*, 76:295–313, 2017.

[167] J. E. Lewis and Mark Maroncelli. On the (Uninteresting) Dependence of the Absorption and Emission Transition Moments of Coumarin 153 on Solvent. *Chem. Phys. Lett.*, 282:197–203, 1998.

[168] Chang-Zhi Li, Chu-Chen Chueh, Hin-Lap Yip, Kevin M O'Malley, Wen-Chang Chen, and Alex K.-Y. Jen. Effective Interfacial Layer to Enhance Efficiency of Polymer Solar Cells via Solution-Processed Fullerene-Surfactants. *J. Mater. Chem.*, 22:8574–8578, 2012.

[169] Nan Li, Zonglong Zhu, Chu-Chen Chueh, Hongbin Liu, Bo Peng, Alessio Petrone, Xiaosong Li, Liduo Wang, and Alex K-Y Jen. Mixed cation FAxPEA1–xPbI3 with Enhanced Phase and Ambient Stability toward High-performance Perovskite Solar Cells. *Adv. Energy Mater.*, 7:1601307, 2017.

[170] Quansong Li, Benedetta Mennucci, Michael A Robb, Lluís Blancafort, and Carles Curutchet. Polarizable QM/MM Multiconfiguration Self-Consistent Field Approach with

State-Specific Corrections: Environment Effects on Cytosine Absorption Spectrum. *J. Chem. Theory Comput.*, 11:1674–1682, 2015.

[171] Xiaosong Li, John C. Tully, H. Bernhard Schlegel, and Michael J. Frisch. Ab Initio Ehrenfest Dynamics. *J. Chem. Phys.*, 123:084106, 2005.

[172] Xiyu Li, Sai Duan, Haichun Liu, Guanying Chen, Yi Luo, and Hans Ågren. Mechanism for the Extremely Efficient Sensitization of Yb3+Luminescence in CsPbCl3 Nanocrystals. *J. Phys. Chem. Lett.*, 10:487–492, 2019.

[173] Zhen Li, Mengjin Yang, Ji-Sang Park, Su-Huai Wei, Joseph J Berry, and Kai Zhu. Stabilizing Perovskite Structures by Tuning Tolerance Factor: Formation of Formamidinium and Cesium Lead Iodide Solid-State Alloys. *Chem. Mater.*, 28:284–292, 2015.

[174] Zhendong Li, Bingbing Suo, Yong Zhang, Yunlong Xiao, and Wenjian Liu. Combining spin-adapted open-shell TD-DFT with spinorbit coupling. *Mol. Phys.*, 111:3741–3755, 2013.

[175] Zhendong Li, Yunlong Xiao, and Wenjian Liu. On the Spin Separation of Algebraic Two-Component Relativistic Hamiltonians. *J. Chem. Phys.*, 137:154114, 2012.

[176] Kangning Liang, David B. Mitzi, and Michael T. Prikas. Synthesis and Characterization of Organic-Inorganic Perovskite Thin Films Prepared Using a Versatile Two-Step Dipping Technique. *Chem. Mater.*, 10:403–411, 1998.

[177] Wenkel Liang, Craig T. Chapman, Feizhi Ding, and Xiaosong Li. Modeling Ultrafast Solvated Electronic Dynamics Using Time-Dependent Density Functional Theory and Polarizable Continuum Model. *J. Phys. Chem. A*, 116:1884–1890, 2012.

[178] Wenkel Liang, Craig T. Chapman, and Xiaosong Li. Efficient First-Principles Electronic Dynamics. *J. Chem. Phys.*, 134:184102, 2011.

[179] John C. Light and Tucker Carrington Jr. Discrete-variable Representations and Their Utilization. *Adv. Chem. Phys.*, 114:263–310, 2000.

[180] Chun Che Lin, Kun Yuan Xu, Da Wang, and Andries Meijerink. Luminescent Manganese-doped CsPbCl 3 Perovskite Quantum Dots. *Sci. Rep.*, 7:45906, 2017.

[181] Hai Lin and Donald G. Truhlar. QM/MM: What Have We Learned, Where Are We, and Where Do We Go From Here? *Theor. Chem. Acc.*, 117:185–199, 2006.

[182] Qianqian Lin, Ardalan Armin, Paul L. Burn, and Paul Meredith. Organohalide Perovskites for Solar Energy Conversion. *Acc. Chem. Res.*, 49:545–553, 2016.

[183] David B. Lingerfelt, Erica Q. Chong, Hongbin Liu, and Xiaosong Li. Gauss-Hermite DVR Code, 2017.

[184] Filippo Lipparini and Vincenzo Barone. Polarizable Force Fields and Polarizable Continuum Model: A Fluctuating Charges/PCM Approach. 1. Theory and Implementation. *J. Chem. Theory Comput.*, 7:3711–3724, 2011.

[185] Filippo Lipparini, Chiara Cappelli, and Vincenzo Barone. Linear Response Theory and Electronic Transition Energies for a Fully Polarizable QM/Classical Hamiltonian. *J. Chem. Theory Comput.*, 8:4153–4165, 2012.

[186] Filippo Lipparini and Jürgen Gauss. Cost-Effective Treatment of Scalar Relativistic Effects for Multireference Systems: A CASSCF Implementation Based on the Spin-free Dirac–Coulomb Hamiltonian. *J. Chem. Theory Comput.*, 12:4284–4295, 2016.

[187] Hongbin Liu, Carl K. Brozek, Shichao Sun, David B. Lingerfelt, Daniel R. Gamelin, and Xiaosong Li. A Hybrid Quantum-Classical Model of Electrostatics in Multiply Charged Quantum Dots. *J. Phys. Chem. C*, 121:26086–26095, 2017.

[188] Hongbin Liu, Andrew J. Jenkins, Andrew Wildman, Michael J. Frisch, Filippo Lipparini, Benedetta Mennucci, and Xiaosong Li. Time-Dependent Complete Active Space Embedded in a Polarizable Force Field. *J. Chem. Theory Comput.*, 15:1633–1641, 2019.

[189] Wenjian Liu. Ideas of Relativistic Quantum Chemistry. *Mol. Phys.*, 108:1679–1706, 2010.

[190] Wenjian Liu. Advances in Relativistic Molecular Quantum Mechanics. *Phys. Rep.*, 537:59–89, 2014.

[191] Wenjian Liu. *Handbook of Relativistic Quantum Chemistry.* Springer-Verlag Berlin Heidelberg, 2017.

[192] Wenjian Liu and Daoling Peng. Infinite-Order Quasirelativistic Density Functional Method Based on the Exact Matrix Quasirelativistic Theory. *J. Chem. Phys.*, 125:044102, 2006.

[193] Wenjian Liu and Daoling Peng. Exact Two-component Hamiltonians Revisited. *J. Chem. Phys.*, 131:031104, 2009.

[194] Zhihui Liu and Rémi Beaulac. On the Nature of the Infrared Transition of Colloidal Indium Nitride Nanocrystals: Non-Parabolicity Effects on the Plasmonic Behavior of Doped Semiconductor Nanomaterials. *Chem. Mater.*, 29:7507–7514, 2017.

[195] Daniele Loco, Étienne Polack, Stefano Caprasecca, Louis Lagardère, Filippo Lipparini, Jean-Philip Piquemal, and Benedetta Mennucci. A QM/MM Approach Using the AMOEBA Polarizable Embedding: From Ground State Energies to Electronic Excitations. *J. Chem. Theory Comput.*, 12:3654–3661, 2016.

[196] Kenneth Lopata and Niranjan Govind. Modeling Fast Electron Dynamics with Real-Time Time-Dependent Density Functional Theory: Application to Small Molecules and Chromophores. *J. Chem. Theory Comput.*, 7:1344–1355, 2011.

[197] Kenneth Lopata, Benjamin E. Van Kuiken, Munira Khalil, and Niri Govind. Linear-Response and Real-Time Time-Dependent Density Functional Theory Studies of Core-Level Near-Edge X-Ray Absorption. *J. Chem. Theory Comput.*, 8:3284–3292, 2012.

[198] Per Åke Malmqvist. Calculation of Transition Density Matrices by Nonunitary Orbital Transformations. *Int. J. Quant. Chem.*, 30:479–494, 1986.

[199] Per Åke Malmqvist and Björn O. Roos. The CASSCF State Interaction Method. *Chem. Phys. Lett.*, 155:189–194, 1989.

[200] Per Åke Malmqvist, Björn O. Roos, and Bernd Schimmelpfennig. The Restricted Active Space (RAS) State Interaction Approach with Spin-orbit Coupling. *Chem. Phys. Lett.*, 357:230–240, 2002.

[201] Joseph S. Manser and Prashant V. Kamat. Band Filling with Free Charge Carriers in Organometal Halide Perovskites. *Nat. Photonics*, 8:737, 2014.

[202] Joseph S. Manser, Makhsud I. Saidaminov, Jeffrey A. Christians, Osman M. Bakr, and Prashant V. Kamat. Making and Breaking of Lead Halide Perovskites. *Acc. Chem. Res.*, 49:330–338, 2016.

[203] Yuezhi Mao, Omar Demerdash, Martin Head-Gordon, and Teresa Head-Gordon. Assessing Ion–Water Interactions in the AMOEBA Force Field Using Energy Decomposition Analysis of Electronic Structure Calculations. *J. Chem. Theory Comput.*, 12:5422–5437, 2016.

[204] Mark Maroncelli and Graham R. Fleming. Picosecond Solvation Dynamics of Coumarin 153: The Importance of Molecular Aspects of Solvation. *J. Chem. Phys.*, 86:6221–6239, 1987.

[205] Mark Maroncelli, Edward W. Castner Jr, Biman Bagchi, and Graham R. Fleming. Dipolar Solvation Dynamics. *Faraday Discuss.*, 85:199–210, 1988.

[206] Joseph W. May, Jiao Ma, Ekaterina Badaeva, and Xiaosong Li. Effect of Excited-State Structural Relaxation on Midgap Excitations in Co^{2+}-Doped ZnO Quantum Dots. *J. Phys. Chem. C*, 118:13152–13156, 2014.

[207] Joseph W. May, Ryan J. McMorris, and Xiaosong Li. Ferromagnetism in *p*-Type Manganese-Doped Zinc Oxide Quantum Dots. *J. Phys. Chem. Lett.*, 3:1374–1380, 2012.

[208] Gary L McPherson and Larry M Henling. EPR Spectrum of Coupled Pairs of Gd3+ Ions in Single Crystals of CsCdBr3. *Phys. Rev. B*, 16:1889, 1977.

[209] Tyler J Milstein, Daniel M Kroupa, and Daniel R Gamelin. Picosecond Quantum Cutting Generates Photoluminescence Quantum Yields Over 100% in Ytterbium-Doped CsPbCl3 Nanocrystals. *Nano Lett.*, 18:3792–3799, 2018.

[210] David B Mitzi. Progress in Inorganic Chemistry. *by KD Karlin, Jonh Wiley & Sons, Inc*, 1999.

[211] David B Mitzi. Templating and Structural Engineering in Organic-Inorganic Perovskites. *Dalton Trans.*, pages 1–12, 2001.

[212] David B. Mitzi, C. A. Feild, W. T. A. Harrison, and A. M. Guloy. Conducting Tin Halides with a Layered Organic-Based Perovskite Structure. *Nature*, 369:467, 1994.

[213] Navendu Mondal, Apurba De, and Anunay Samanta. Achieving Near-Unity Photoluminescence Efficiency for Blue-Violet-Emitting Perovskite Nanocrystals. *ACS Energy Lett.*, 4:32–39, 2018.

[214] Chang-Youn Moon and Su-Huai Wei. Band gap of Hg Chalcogenides: Symmetry-reduction-induced Band-gap Opening of Materials with Inverted Band Structures. *Phys. Rev. B*, 74:045205, 2006.

[215] Ivan Mora-Sero, Luca Bertoluzzi, Victoria Gonzalez-Pedro, Sixto Gimenez, Francisco Fabregat-Santiago, Kyle W. Kemp, Edward H. Sargent, and Juan Bisquert. Selective Contacts Drive Charge Extraction in Quantum Dot Solids via Asymmetry in Carrier Transfer Kinetics. *Nat. Commun.*, 4:2272, 2013.

[216] Gerrit Moritz, Alexander Wolf, and Markus Reiher. Relativistic DMRG Calculations on the Curve Crossing of Cesium Hydride. *J. Chem. Phys.*, 123:184105, 2005.

[217] Annette Mühlpfordt, Roland Schanz, Nikolaus P. Ernsting, Vadim Farztdinov, and Stefan Grimme. Coumarin 153 in the Gas Phase: Optical Spectra and Quantum Chemical Calculations. *Phys. Chem. Chem. Phys.*, 1:3209–3218, 1999.

[218] Frank Neese. Zero-Field Splitting. In Martin Kaupp, Michael Bühl, and Vladimir G. Malkin, editors, *Calculation of NMR and EPR Parameters: Theory and Applications*, chapter 31, pages 541–564. Wiley-VCH Verlag GmbH & Co. KGaA, 2004.

[219] Heidi D. Nelson, Xiaosong Li, and Daniel R. Gamelin. Computational Studies of the Electronic Structures of Copper-Doped CdSe Nanocrystals: Oxidation States, Jahn–Teller Distortions, Vibronic Bandshapes, and Singlet–Triplet Splittings. *J. Phys. Chem. C*, 120:5714–5723, 2016.

[220] Triet S. Nguyen, Ravindra Nanguneri, and John Parkhill. How Electronic Dynamics with Pauli Exclusion Produces Fermi-Dirac Statistics. *J. Chem. Phys.*, 142:134113, 2015.

[221] Triet S. Nguyen and John Parkhill. Nonadiabatic Dynamics for Electrons at Second-Order: Real-Time TDDFT and OSCF2. *J. Chem. Theory Comput.*, 11:2918–2924, 2015.

[222] Triet S. Nguyen and John Parkhill. Nonradiative Relaxation in Real-Time Electronic Dynamics OSCF2: Organolead Triiodide Perovskite. *J. Phys. Chem. A*, 120:6880–6887, 2016.

[223] Wanyi Nie, Hsinhan Tsai, Reza Asadpour, Jean-Christophe Blancon, Amanda J Neukirch, Gautam Gupta, Jared J Crochet, Manish Chhowalla, Sergei Tretiak, and Muhammad A. Alam. High-Efficiency Solution-Processed Perovskite Solar Cells with Millimeter-Scale Grains. *Science*, 347:522–525, 2015.

[224] Lea Nienhaus, Joshua J Goings, Duc Nguyen, Sarah Wieghold, Joseph Lyding, Xiaosong Li, and Martin Gruebele. Imaging Excited Orbitals of Quantum Dots: Experiment and Electronic Structure Theory. *J. Am. Chem. Soc.*, 137:14743–14750, 2015.

[225] Takeshiand Noro, Masahiroand Sekiya, and Toshikatsu Koga. Sapporo-(DKH3)-nZP (n= D, T, Q) Sets for the Sixth Period s-, d-, and p-Block Atoms. *Theor. Chem. Acc.*, 132:1363, 2013.

[226] Jeppe Olsen, Bjorn O Roos, and Poul Jørgensen. Determinant Based Configuration Interaction Algorithms for Complete and Restricted Configuration Interaction Spaces. *J. Chem. Phys.*, 89:2185–2192, 1988.

[227] B. O'Regan and M. Grätzel. A Low-Cost, High-Efficiency Solar Cell Based on Dye-Sensitized Colloidal TiO_2 Films. *Nature*, 353:737–740, 1991.

[228] Gencai Pan, Xue Bai, Dongwen Yang, Xu Chen, Pengtao Jing, Songnan Qu, Lijun Zhang, Donglei Zhou, Jinyang Zhu, Wen Xu, et al. Doping Lanthanide into Perovskite Nanocrystals: Highly Improved and Expanded Optical Properties. *Nano Lett.*, 17:8005–8011, 2017.

[229] Nam-Gyu Park. Organometal Perovskite Light Absorbers toward a 20% Efficiency Low-Cost Solid-State Mesoscopic Solar Cell. *J. Phys. Chem. Lett.*, 4:2423–2429, 2013.

[230] Robert G Parr. Density Functional Theory of Atoms and Molecules. In *Horizons of Quantum Chemistry*, pages 5–15. Springer, 1980.

[231] Himadri Pathak, Sudip Sasmal, Malaya K. Nayak, Nayana Vaval, and Sourav Pal. Relativistic Equation-of-motion Coupled-Cluster Method for the Electron Attachment Problem. *Comput. Theor. Chem.*, 1076:94 – 100, 2016.

[232] Norman Pellet, Peng Gao, Giuliano Gregori, Tae-Youl Yang, Mohammad K. Nazeeruddin, Joachim Maier, and Michael Grätzel. Mixed-Organic-Cation Perovskite Photovoltaics for Enhanced Solar-Light Harvesting. *Angew. Chem. Int. Ed.*, 53:3151–3157, 2014.

[233] Bo Peng, Joseph W. May, Daniel R. Gamelin, and Xiaosong Li. Effects of Crystallographic and Shape Anisotropies on Dopant-Carrier Exchange Interactions in Magnetic Semiconductor Quantum Dots. *J. Phys. Chem. C*, 118:7630–7636, 2014.

[234] Daoling Peng, Wenjian Liu, Yunlong Xiao, and Lan Cheng. Making Four- and Two-Component Relativistic Density Functional Methods Fully Equivalent Based on the Idea of From Atoms to Molecule. *J. Chem. Phys.*, 127:104106, 2007.

[235] Daoling Peng, Nils Middendorf, Florian Weigend, and Markus Reiher. An Efficient Implementation of Two-Component Relativistic Exact-Decoupling Methods for Large Molecules. *J. Chem. Phys.*, 138:184105, 2013.

[236] Wei-Tao Peng, B. Scott Fales, and Benjamin G. Levine. Simulating Electron Dynamics of Complex Molecules with Time-Dependent Complete Active Space Configuration Interaction. *J. Chem. Theory Comput.*, 14:4129–4138, 2018.

[237] David J. Peper, Jennifer L .and Vinyard, Gary W. Brudvig, and James M. Mayer. Slow Equilibration between Spectroscopically Distinct Trap States in Reduced TiO2 Nanoparticles. *J. Am. Chem. Soc.*, 139:2868–2871, 2017.

[238] John P. Perdew, Kieron Burke, and Matthias Ernzerhof. Generalized Gradient Approximation Made Simple. *Phys. Rev. Lett.*, 77:3865, 1996.

[239] John P. Perdew, Kieron Burke, and Matthias Ernzerhof. Generalized Gradient Approximation Made Simple [Phys. Rev. Lett. 77, 3865 (1996)]. *Phys. Rev. Lett.*, 78:1396–1396, 1997.

[240] Alessio Petrone, David B. Lingerfelt, Nadia Rega, and Xiaosong Li. From Charge-Transfer to a Charge-Separated State: A Perspective from the Real-Time TDDFT Excitonic Dynamics. *Phys. Chem. Chem. Phys.*, 16:24457–24465, 2014.

[241] Loredana Protesescu, Sergii Yakunin, Maryna I. Bodnarchuk, Franziska Krieg, Riccarda Caputo, Christopher H. Hendon, Ruo Xi Yang, Aron Walsh, and Maksym V. Kovalenko. Nanocrystals of Cesium Lead Halide Perovskites (CsPbX 3, X = Cl, Br, and I): Novel Optoelectronic Materials Showing Bright Emission with Wide Color Gamut. *Nano Lett.*, 15:3692–3696, 2015.

[242] Makenzie R. Provorse, Bradley F. Habenicht, and Christine M. Isborn. Peak-Shifting in Real-Time Time-Dependent Density Functional Theory. *J. Chem. Theory Comput.*, 11:4791–4802, 2015.

[243] Pekka Pyykkö. Relativistic Effects in Structural Chemistry. *Chem. Rev.*, 88:563–594, 1988.

[244] Pekka Pyykkö. Relativistic Effects in Chemistry: More Common Than You Thought. *Annu. Rev. Phys. Chem.*, 63:45–64, 2012.

[245] Li Na Quan, Mingjian Yuan, Riccardo Comin, Oleksandr Voznyy, Eric M. Beauregard, Sjoerd Hoogland, Andrei Buin, Ahmad R. Kirmani, Kui Zhao, and Aram Amassian. Ligand-Stabilized Reduced-Dimensionality Perovskites. *J. Am. Chem. Soc.*, 138:2649–2655, 2016.

[246] Shampa Raghunathan and Mathias Nest. Critical Examination of Explicitly Time-Dependent Density Functional Theory for Coherent Control of Dipole Switching. *J. Chem. Theory Comput.*, 7:2492–2497, 2011.

[247] Adharsh Rajagopal, Spencer T. Williams, Chu-Chen Chueh, and Alex K.-Y. Jen. Abnormal Current-Voltage Hysteresis Induced by Reverse Bias in Organic-Inorganic Hybrid Perovskite Photovoltaics. *J. Phys. Chem. Lett.*, 7:995–1003, 2016.

[248] Christian Reichardt. Solvatochromic Dyes as Solvent Polarity Indicators. *Chem. Rev.*, 94:2319–2358, 1994.

[249] Markus Reiher and Alexander Wolf. Exact Decoupling of the Dirac Hamiltonian. I. General Theory. *J. Chem. Phys.*, 121:2037, 2004.

[250] Markus Reiher and Alexander Wolf. Exact Decoupling of the DIrac Hamiltonian. II. The Generalized Douglas-Kroll-Hess Transformation Up to Arbitrary Order. *J. Chem. Phys.*, 121:10945, 2004.

[251] Markus Reiher and Alexander Wolf. *Relativistic Quantum Chemistry*. Wiley-VCH, second edition, 2015.

[252] M. Repisky, S. Komorovsky, V. G. Malkin, O. L. Malkina, M. Kaupp, K. Ruud, R. Bast, U. Ekstrom, M. Kadek, S. Knecht, L. Konecňý, E. Malkin, and Ondík Malkin. Relativistic Spectroscopy DFT Program ReSpect, 2018. http://www.respectprogram.org.

[253] L. Reynolds, J. A. Gardecki, S. J. V. Frankland, M. L. Horng, and M. Maroncelli. Dipole Solvation in Nondipolar Solvents: Experimental Studies of Reorganization Energies and Solvation Dynamics. *J. Phys. Chem.*, 100:10337–10354, 1996.

[254] Ryan D. Reynolds, Takeshi Yanai, and Toru Shiozaki. Large-scale Relativistic Complete Active Space Self-Consistent Field with Robust Convergence. *J. Chem. Phys.*, 149:014106, 2018.

[255] Steven W. Rick and B. J. Berne. Dynamical Fluctuating Charge Force Fields: The Aqueous Solvation of Amides. *J. Am. Chem. Soc.*, 118:672–679, 1996.

[256] Steven W. Rick, Steven J. Stuart, and B. J. Berne. Dynamical Fluctuating Charge Force Fields: Application to Liquid Water. *J. Chem. Phys.*, 101:6141–6156, 1998.

[257] Jeffery D. Rinehart, Alina M. Schimpf, Amanda L. Weaver, Alicia W. Cohn, and Daniel R. Gamelin. Photochemical Electronic Doping of Colloidal CdSe Nanocrystals. *J. Am. Chem. Soc.*, 135:18782–18785, 2013.

[258] Aarnoud L. Roest, John J. Kelly, and Daniël Vanmaekelbergh. Coulomb Blockade of Electron Transport in a ZnO Quantum-dot Solid. *Appl. Phys. Lett.*, 83:5530, 2003.

[259] Bjorn O. Roos and Per-Åke Malmqvist. Relativistic Quantum Chemistry: The Multiconfigurational Approach. *Phys. Chem. Chem. Phys.*, 6:2919–2927, 2004.

[260] Bjorn O. Roos, Peter R. Taylor, and Per E. M. Siegbahn. A Complete Active Space SCF Method (CASSCF) Using a Density Matrix Formulated Super-CI Approach. *Chem. Phys.*, 48:157–173, 1980.

[261] Carlo Andrea Rozzi, Sarah Maria Falke, Nicola Spallanzani, Angel Rubio, Elisa Molinari, Daniele Brida, Margherita Maiuri, Giulio Cerullo, Heiko Schramm, Jens Christoffers, and Christoph Lienau. Quantum Coherence Controls the Charge Separation in a Prototypical Artificial Light-Harvesting System. *Nat. Commun.*, 4:1602, 2013.

[262] M Ruggenthaler and D Bauer. Rabi Oscillations and Few-Level Approximations in Time-Dependent Density Functional Theory. *Phys. Rev. Lett.*, 102:233001, 2009.

[263] Michael Saliba, Taisuke Matsui, Ji-Youn Seo, Konrad Domanski, Juan-Pablo Correa-Baena, Mohammad Khaja Nazeeruddin, Shaik M. Zakeeruddin, Wolfgang Tress, Antonio Abate, Anders Hagfeldt, et al. Cesium-Containing Triple Cation Perovskite Solar Cells: Improved Stability, Reproducibility and High Efficiency. *Energ. Environ. Sci.*, 9:1989–1997, 2016.

[264] Bayrammurad Saparov and David B Mitzi. Organic-Inorganic Perovskites: Structural Versatility for Functional Materials Design. *Chem. Rev.*, 116:4558–4596, 2016.

[265] Trond Saue. Relativistic Hamiltonians for Chemistry: A Primer. *ChemPhysChem*, 12:3077–3094, 2011.

[266] Alina M. Schimpf, Carolyn E. Gunthardt, Jeffrey D. Rinehart, James M. Mayer, and Daniel R. Gamelin. Controlling Carrier Densities in Photochemically Reduced Colloidal ZnO Nanocrystals: Size Dependence and Role of the Hole Quencher. *J. Am. Chem. Soc.*, 135:16569–16577, 2013.

[267] Alina M. Schimpf, Kathryn E. Knowles, Gerard M. Carroll, and Daniel R. Gamelin. Electronic Doping and Redox-Potential Tuning in Colloidal Semiconductor Nanocrystals. *Acc. Chem. Res.*, 48:1929–1937, 2015.

[268] Alina M. Schimpf, Sebastien D. Lounis, Evan L. Runnerstrom, Delia J. Milliron, and Daniel R. Gamelin. Redox Chemistries and Plasmon Energies of Photodoped In_2O_3 and Sn-Doped In_2O_3 (ITO) Nanocrystals. *J. Am. Chem. Soc.*, 137:518–524, 2015.

[269] Alina M. Schimpf, Niket Thakkar, Carolyn E. Gunthardt, David J. Masiello, and Daniel R. Gamelin. Charge-Tunable Quantum Plasmons in Colloidal Semiconductor Nanocrystals. *ACS Nano*, 8:1065–1072, 2014.

[270] H. Bernhard Schlegel, Stanley M. Smith, and Xiaosong Li. Electronic Optical Response of Molecules in Intense Fields: Comparison of TD-HF, TD-CIS, and TD-CIS(D) Approaches. *J. Chem. Phys.*, 126:244110, 2007.

[271] Jangwon Seo, Jun Hong Noh, and Sang Il Seok. Rational strategies for efficient perovskite solar cells. *Acc. Chem. Res.*, 49:562–572, 2016.

[272] Wahyu Setyawan and Stefano Curtarolo. High-Throughput Electronic Band Structure Calculations: Challenges and Tools. *Comput. Mater. Sci.*, 49:299–312, 2010.

[273] Yuchuan Shao, Zhengguo Xiao, Cheng Bi, Yongbo Yuan, and Jinsong Huang. Origin and Elimination of Photocurrent Hysteresis by Fullerene Passivation in CH3NH3PbI3 Planar Heterojunction Solar Cells. *Nat. Commun.*, 5:5784, 2014.

[274] A. C. Sharma. Size-dependent Energy Band gap and Dielectric Constant within the Generalized Penn model Applied to a Semiconductor Nanocrystallite. *J. Appl. Phys.*, 100:084301, 2006.

[275] Moonsub Shim and Philippe Guyot-Sionnest. n-type Colloidal Semiconductor Nanocrystals. *Nature*, 407:981–983, 2000.

[276] Toru Shiozaki and Wataru Mizukami. Relativistic Internally Contracted Multireference Electron Correlation Methods. *J. Chem. Theory Comput.*, 11:4733–4739, 2015.

[277] William Shockley. On the Surface States Associated with a Periodic Potential. *Phys. Rev.*, 56:317–323, 1939.

[278] Yinan Shu, Edward G. Hohenstein, and Benjamin G. Levine. Configuration Interaction Singles Natural Orbitals: An Orbital Basis for an Efficient and size Intensive Multireference Description of Electronic Excited States. *J. Chem. Phys.*, 142:024102, 2015.

[279] Ian C. Smith, Eric T. Hoke, Diego Solis-Ibarra, Michael D. McGehee, and Hemamala I. Karunadasa. A Layered Hybrid Perovskite Solar-Cell Absorber with Enhanced Moisture Stability. *Angew. Chem. Int. Ed.*, 53:11232–11235, 2014.

[280] Henry J. Snaith. Perovskites: The Emergence of a New Era for Low-Cost, High-Efficiency Solar Cells. *J. Phys. Chem. Lett.*, 4:3623–3630, 2013.

[281] Vedentam Srikant and David R. Clarke. On the Optical Band Gap of Zinc Oxide. *J. Appl. Phys.*, 83:5447–5451, 1998.

[282] Ajay Ram Srimath Kandada and Annamaria Petrozza. Photophysics of Hybrid Lead Halide Perovskites: The Role of Microstructure. *Acc. Chem. Res.*, 49:536–544, 2016.

[283] Samuel D. Stranks and Henry J. Snaith. Metal-Halide Perovskites for Photovoltaic and Light-Emitting Devices. *Nat. Nanotechnol.*, 10:391, 2015.

[284] Richard M. Stratt and Mark Maroncelli. Nonreactive Dynamics in Solution: The Emerging Molecular View of Solvation Dynamics and Vibrational Relaxation. *J. Phys. Chem.*, 100:12981–12996, 1996.

[285] Tze Chien Sum and Nripan Mathews. Advancements in Perovskite Solar Cells: Photophysics behind the Photovoltaics. *Energ. Environ. Sci.*, 7:2518–2534, 2014.

[286] Patrick K. Tamukong, Mark R. Hoffmann, Zhendong Li, and Wenjian Liu. Relativistic GVVPT2 Multireference Perturbation Theory Description of the Electronic States of Y_2 and Tc_2. *J. Phys. Chem. A*, 118:1489–1501, 2014.

[287] B. T. Thole. Molecular Polarizabilities Calculated with a Modified Dipole Interaction. *Chem. Phys.*, 59:341–350, 1981.

[288] Jørn Thyssen, Timo Fleig, and Hans Jørgen Aa Jensen. A Direct Relativistic Four-component Multiconfiguration Self-Consistent-Field Method for Molecules. *J. Chem. Phys.*, 129:034109, 2008.

[289] Zheyan Tu, Fan Wang, and Xiangyuan Li. Equation-of-motion Coupled-Cluster Method for Ionized States with Spin-orbit Coupling. *J. Chem. Phys.*, 136:174102, 2012.

[290] C. A. Ullrich, P. G. Reinhard, and E. Suraud. Electron Dynamics in Strongly Excited Sodium Clusters: A Density-Functional Study with Self-Interaction Correction. *J. Phys. B*, 31:1871–1885, 1998.

[291] Inga S. Ulusoy, Zachary Stewart, and Angela K. Wilson. The Role of the CI Expansion Length in Time-Dependent Studies. *J. Chem. Phys.*, 148:014107, 2018.

[292] Morgane Vacher, Lee Steinberg, Andrew J. Jenkins, Michael J. Bearpark, and Michael A. Robb. Electron Dynamics Following Photoionization: Decoherence due to the Nuclear-Wave-Packet Width. *Phys. Rev. A*, 92:040502, 2015.

[293] Piet Th. van Duijnen and Marcel Swart. Molecular and Atomic Polarizabilities: Thole's Model Revisited. *J. Phys. Chem. A*, 102:2399–2407, 1998.

[294] Bess Vlaisavljevich and Toru Shiozaki. Nuclear Energy Gradients for Internally Contracted Complex Active Space Second-Order Perturbation Theory: Multistate Extensions. *J. Chem. Theory Comput.*, 12:3781–3787, 2016.

[295] Willard R. Wadt and P. Jeffery Hay. Ab initio Effective Core Potentials for Molecular Calculations. Potentials for Main Group Elements Na to Bi. *J. Chem. Phys.*, 82:284–298, 1985.

[296] Feng Wang, Hui Yu, Haihua Xu, and Ni Zhao. HPbI3: A New Precursor Compound for Highly Efficient Solution-Processed Perovskite Solar Cells. *Adv. Func. Mater.*, 25:1120–1126, 2015.

[297] Jia-Pei Wang, Jun-Sheng Chen, and Guang-Jiu Zhao. Steady-State and Time-Resolved Spectroscopic Investigations on the Existence of Stable Methanol/AOT/n-Heptane Reverse Micelles. *J. Colloid Interface Sci.*, 423:1–6, 2014.

[298] Junmei Wang, Piotr Cieplak, and Peter A. Kollman. How Well Does a Restrained Electrostatic Potential (RESP) Model Perform in Calculating Conformational Energies of Organic and Biological Molecules? *J. Comput. Chem.*, 21:1049–1074, 2000.

[299] Junmei Wang, Piotr Cieplak, Jie Li, Tingjun Hou, Ray Luo, and Yong Duan. Development of Polarizable Models for Molecular Mechanical Calculations I: Parameterization of Atomic Polarizability. *J. Phys. Chem. B*, 115:3091–3099, 2011.

[300] Lin-Wang Wang and Alex Zunger. Pseudopotential Calculations of Nanoscale CdSe Quantum Dots. *Phys. Rev. B*, 53:9579–9582, 1996.

[301] Kei Watanabe, Masanori Koshimizu, Takayuki Yanagida, Yutaka Fujimoto, and Keisuke Asai. Luminescence and Scintillation Properties of La-and La, Ag-doped CsPbCl3 Single Crystals. *Jpn. J. Appl. Phys.*, 55:02BC20, 2016.

[302] Brian L. Wehrenberg and Philippe Guyot-Sionnest. Electron and Hole Injection in PbSe Quantum Dot Films. *J. Am. Chem. Soc.*, 125:7806–7807, 2003.

[303] Su-Huai Wei and Alex Zunger. Calculated Natural Band Offsets of all II–VI and III–V Semiconductors: Chemical Trends and the Role of Cation d Orbitals. *Appl. Phys. Lett.*, 72:2011–2013, 1998.

[304] Hans Joachim Werner and Wilfried Meyer. A Quadratically Convergent MCSCF Method for the Simultaneous Optimization of Several States. *J. Chem. Phys.*, 74:5794–5801, 1981.

[305] Hans-Joachim Werner and Wilfried Meyer. A Quadratically Convergent MCSCF Method for the Simultaneous Optimization of Several States a Quadratically Convergent MCSCF Method for the Simultaneous Optimization of Several States. *J. Chem. Phys.*, 74:5794, 1981.

[306] Damon A. Wheeler, Yichuan Ling, Robert J. Dillon, Robert C. Fitzmorris, Christopher G. Dudzik, Liat Zavodivker, Tijana Rajh, Nada M. Dimitrijevic, Glenn Millhauser, Christopher Bardeen, Yat Li, and Jin Z. Zhang. Probing the Nature of Bandgap States in Hydrogen-Treated TiO2 Nanowires. *J. Phys. Chem. C*, 117:26821–26830, 2013.

[307] Andrew Wildman, Greta Donati, Filippo Lipparini, Benedetta Mennucci, and Xiaosong Li. Nonequilibrium Environment Dynamics in a Frequency-Dependent Polarizable Embedding Model. *J. Chem. Theory Comput.*, 15:43–51, 2019.

[308] Spencer T. Williams, Chu-Chen Chueh, and Alex K.-Y. Jen. Navigating Organo-Lead Halide Perovskite Phase Space via Nucleation Kinetics toward a Deeper Understanding of Perovskite Phase Transformations and Structure–Property Relationships. *Small*, 11:3088–3096, 2015.

[309] Spencer T. Williams, Adharsh Rajagopal, Chu-Chen Chueh, and Alex K.-Y. Jen. Current Challenges and Prospective Research for Upscaling Hybrid Perovskite Photovoltaics. *J. Phys. Chem. Lett.*, 7:811–819, 2016.

[310] David Williams-Young, Franco Egidi, and Xiaosong Li. Relativistic Two-Component Particle-Particle Tamm-Dancoff Approximation. *J. Chem. Theory Comput.*, 12:5379–5384, 2016.

[311] Alexander Wolf and Markus Reiher. Exact Decoupling of the Dirac Hamiltonian. III. Molecular Properties. *J. Chem. Phys.*, 121:064102, 2004.

[312] Bo Wu, Huy Tiep Nguyen, Zhiliang Ku, Guifang Han, David Giovanni, Nripan Mathews, Hong Jin Fan, and Tze Chien Sum. Discerning the Surface and Bulk Recombination Kinetics of Organic-Inorganic Halide Perovskite Single Crystals. *Adv. Energy Mater.*, 6:1600551, 2016.

[313] Wenhua Xu, Jianyi Ma, Daoling Pen, Wenli Zou, Wenjian Liu, and Volker Staemmler. Excited States of ReO_4^-: A Comprehensive Time-Dependent Relativistic Density Functional Theory Study. *Chem. Phys.*, 356:219–228, 2009.

[314] Wenhua Xu, Yong Zhang, and Wenjian Liu. Time-dependent relativistic density functional study of Yb and YbO. *Sci. China Ser. B Chem.*, 52:1945–1953, 2009.

[315] Sibel Ebru Yalcin, Joelle A. Labastide, Danielle L. Sowle, and Michael D. Barnes. Spectral Properties of Multiply Charged Semiconductor Quantum Dots. *Nano Lett.*, 11:4425–4430, 2011.

[316] Dong-Dong Yang, Fan Wang, and Jingwei Guo. Equation of Motion Coupled Cluster Method for Electron Attached States with Spin-orbit Coupling. *Chem. Phys. Lett.*, 531:236 – 241, 2012.

[317] Woon Seok Yang, Jun Hong Noh, Nam Joong Jeon, Young Chan Kim, Seungchan Ryu, Jangwon Seo, and Sang Il Seok. High-Performance Photovoltaic Perovskite Layers Fabricated through Intramolecular Exchange. *Science*, 348:1234–1237, 2015.

[318] Chenyi Yi, Jingshan Luo, Simone Meloni, Ariadni Boziki, Negar Ashari-Astani, Carole Grätzel, Shaik M. Zakeeruddin, Ursula Röthlisberger, and Michael Grätzel. Entropic Stabilization of Mixed A-Cation ABX 3 Metal Halide Perovskites for High Performance Perovskite Solar Cells. *Energ. Environ. Sci.*, 9:656–662, 2016.

[319] Jun Yin, Ghada H Ahmed, Osman M Bakr, Jean-Luc Brdas, and Omar F Mohammed. Unlocking the Effect of Trivalent Metal Doping in All-Inorganic CsPbBr3 Perovskite. *ACS Energy Lett.*, 4:789–795, 2019.

[320] Wan-Jian Yin, Tingting Shi, and Yanfa Yan. Unique Properties of Halide Perovskites as Possible Origins of the Superior Solar Cell Performance. *Adv. Mater.*, 26:4653–4658, 2014.

[321] Wan-Jian Yin, Tingting Shi, and Yanfa Yan. Unusual Defect Physics in CH3NH3PbI3 Perovskite Solar Cell Absorber. *Appl. Phys. Lett.*, 104:063903, 2014.

[322] Wan-Jian Yin, Ji-Hui Yang, Joongoo Kang, Yanfa Yan, and Su-Huai Wei. Halide Perovskite Materials for Solar Cells: A Theoretical Review. *J. Mater. Chem. A*, 3:8926–8942, 2015.

[323] Zi-Jun Yong, Shao-Qiang Guo, Ju-Ping Ma, Jun-Ying Zhang, Zhi-Yong Li, Ya-Meng Chen, Bin-Bin Zhang, Yang Zhou, Jie Shu, Jia-Li Gu, et al. Doping-enhanced Short-range Order of Perovskite Nanocrystals for Near-unity Violet Luminescence Quantum Yield. *J. Am. Chem. Soc.*, 140:9942–9951, 2018.

[324] Hui Yu, Feng Wang, Fangyan Xie, Wenwu Li, Jian Chen, and Ni Zhao. The Role of Chlorine in the Formation Process of ?CH3NH3PbI3-xClx? Perovskite. *Adv. Func. Mater.*, 24:7102–7108, 2014.

[325] Yongbo Yuan and Jinsong Huang. Ion Migration in Organometal Trihalide Perovskite and its Impact on Photovoltaic Efficiency and Stability. *Acc. Chem. Res.*, 49:286–293, 2016.

[326] Abd Rashid bin Mohd Yusoff and Mohammad Khaja Nazeeruddin. Organohalide Lead Perovskites for Photovoltaic Applications. *J. Phys. Chem. Lett.*, 7:851–866, 2016.

[327] Boyi Zhang, Jonathon E. Vandezande, Ryan D. Reynolds, and Henry F. Schaefer. Spin-Orbit Coupling via Four-Component Multireference Methods: Benchmarking on p-Block Elements and Tentative Recommendations. *J. Chem. Theory Comput.*, 14:1235–1246, 2018.

[328] Igor Ying Zhang, Xinguo Ren, Patrick Rinke, Volker Blum, and Matthias Scheffler. Numeric Atom-Centered-Orbital Basis Sets with Valence-Correlation Consistency from H to Ar. *New J. Phys.*, 15:123033, 2013.

[329] Yong Zhang, Wenhua Xu, Qiming Sun, Wenli Zou, and Wenjian Liu. Excited States of OsO_4: A Comprehensive Time-Dependent Relativistic Density Functional Theory Study. *J. Comput. Chem.*, 31:532–551, 2010.

[330] Donglei Zhou, Dali Liu, Gencai Pan, Xu Chen, Dongyu Li, Wen Xu, Xue Bai, and Hongwei Song. Cerium and Ytterbium Codoped Halide Perovskite Quantum Dots: A Novel and Efficient Downconverter for Improving the Performance of Silicon Solar Cells. *Adv. Mater.*, 29:1704149, 2017.